

# Towards an Understanding of the Correlations in Jet Substructure

Report of BOOST2013, hosted by the University of Arizona, 12<sup>th</sup>-16<sup>th</sup> of August 2013.

D. Adams<sup>1</sup>, A. Arce<sup>2</sup>, L. Asquith<sup>3</sup>, M. Backovic<sup>4</sup>, T. Barillari<sup>5</sup>, P. Berta<sup>6</sup>, D. Bertolini<sup>7</sup>,  
A. Buckley<sup>8</sup>, J. Butterworth<sup>9</sup>, R. C. Camacho Toro<sup>10</sup>, J. Caudron<sup>11</sup>, Y.-T. Chien<sup>12</sup>, J. Cogan<sup>13</sup>,  
B. Cooper<sup>9</sup>, D. Curtin<sup>14</sup>, C. Debenedetti<sup>15</sup>, J. Dolen<sup>16</sup>, M. Eklund<sup>17</sup>, S. El Hedri<sup>18</sup>,  
S. D. Ellis<sup>19</sup>, T. Embry<sup>17</sup>, D. Ferencek<sup>20</sup>, J. Ferrando<sup>21</sup>, S. Fleischmann<sup>22</sup>, M. Freytsis<sup>23</sup>,  
M. Giuliani<sup>24</sup>, Z. Han<sup>25</sup>, D. Hare<sup>26</sup>, P. Harris<sup>27</sup>, A. Hinzmann<sup>28</sup>, R. Hoing<sup>29</sup>, A. Hornig<sup>12</sup>,  
M. Jankowiak<sup>30</sup>, K. Johns<sup>17</sup>, G. Kasieczka<sup>31</sup>, R. Kogler<sup>29</sup>, W. Lampl<sup>17</sup>, A. J. Larkoski<sup>32</sup>,  
C. Lee<sup>12</sup>, R. Leone<sup>17</sup>, P. Loch<sup>17</sup>, D. Lopez Mateos<sup>23</sup>, H. K. Lou<sup>33</sup>, M. Low<sup>34</sup>,  
P. Maksimovic<sup>35</sup>, I. Marchesini<sup>29</sup>, S. Marzani<sup>32</sup>, L. Masetti<sup>18</sup>, R. McCarthy<sup>36</sup>, S. Menke<sup>5</sup>,  
D. W. Miller<sup>34</sup>, K. Mishra<sup>26</sup>, B. Nachman<sup>13</sup>, P. Nef<sup>13</sup>, F. T. O'Grady<sup>17</sup>, A. Ovcharova<sup>37</sup>,  
A. Picazio<sup>10</sup>, C. Pollard<sup>21</sup>, B. Potter-Landua<sup>27</sup>, C. Potter<sup>27</sup>, S. Rappoccio<sup>16</sup>, J. Rojo<sup>38</sup>,  
J. Rutherford<sup>17</sup>, G. P. Salam<sup>27,39</sup>, J. Schabinger<sup>40</sup>, A. Schwartzman<sup>13</sup>, M. D. Schwartz<sup>23</sup>,  
B. Shuve<sup>41</sup>, P. Sinervo<sup>42</sup>, D. Soper<sup>25</sup>, D. E. Sosa Corral<sup>24</sup>, M. Spannowsky<sup>43</sup>, E. Strauss<sup>13</sup>,  
M. Swiatlowski<sup>13</sup>, J. Thaler<sup>32</sup>, C. Thomas<sup>27</sup>, E. Thompson<sup>44</sup>, N. V. Tran<sup>26</sup>, J. Tseng<sup>38</sup>,  
E. Usai<sup>29</sup>, L. Valery<sup>45</sup>, J. Veatch<sup>17</sup>, M. Vos<sup>46</sup>, W. Waalewijn<sup>47</sup>, J. Wacker<sup>13</sup>, and C. Young<sup>27</sup>

<sup>1</sup>Brookhaven National Laboratory, Upton, NY 11973, USA

<sup>2</sup>Duke University, Durham, NC 27708, USA

<sup>3</sup>Argonne National Laboratory, Lemont, IL 60439, USA

<sup>4</sup>CP3, Universite catholique du Louvain, B-1348 Louvain-la-Neuve, Belgium

<sup>5</sup>Max-Planck-Institute fuer Physik, 80805 Muenchen, Germany

<sup>6</sup>Charles University in Prague, 116 36 Praha 1, Czech Republic

<sup>7</sup>University of California, Berkeley, CA 94720, USA

<sup>8</sup>University of Edinburgh, EH9 3JZ, UK

<sup>9</sup>University College London, WC1E 6BT, UK

<sup>10</sup>University of Geneva, CH-1211 Geneva 4, Switzerland

<sup>11</sup>RWTH Aachen University, 52062 Aachen, Germany

<sup>12</sup>Los Alamos National Laboratory, Los Alamos, NM 87545, USA

<sup>13</sup>SLAC National Accelerator Laboratory, Menlo Park, CA 94025, USA

<sup>14</sup>University of Maryland, College Park, MD 20742, USA

<sup>15</sup>University of California, Santa Cruz, CA 95064, USA

<sup>16</sup>University at Buffalo, Buffalo, NY 14260, USA

<sup>17</sup>University of Arizona, Tucson, AZ 85719, USA

<sup>18</sup>Universitaet Mainz, DE 55099, Germany

<sup>19</sup>University of Washington, Seattle, WA 98195, USA

<sup>20</sup>Rutgers University, Piscataway, NJ 08854, USA

<sup>21</sup>University of Glasgow, Glasgow, G12 8QQ, UK

<sup>22</sup>Bergische Universitaet Wuppertal, Wuppertal, D-42097, Germany

<sup>23</sup>Harvard University, Cambridge, MA 02138, USA

<sup>24</sup>Universitaet Heidelberg, DE-69117, Germany

<sup>25</sup>University of Oregon, Eugene, OR 97403, USA

<sup>26</sup>Fermi National Accelerator Laboratory, Batavia, IL 60510, USA

<sup>27</sup>CERN, CH-1211 Geneva 23, Switzerland

<sup>28</sup>Universitaet Zuerich, 8006 Zuerich, Switzerland

<sup>29</sup>Universitaet Hamburg, DE-22761, Germany

<sup>30</sup>New York University, New York, NY 10003, USA

<sup>31</sup>ETH Zuerich, 8092 Zuerich, Switzerland

<sup>32</sup>Massachusetts Institute of Technology, Cambridge, MA 02139, USA

<sup>33</sup>Princeton University, Princeton, NJ 08544, USA

<sup>34</sup>University of Chicago, IL 60637, USA

<sup>35</sup>Johns Hopkins University, Baltimore, MD 21218, USA

<sup>36</sup>YITP, Stony Brook University, Stony Brook, NY 11794-3840, USA

<sup>37</sup>Berkeley National Laboratory, University of California, Berkeley, CA 94720, USA

<sup>38</sup>University of Oxford, Oxford, OX1 3NP, UK

<sup>39</sup>LPTHE, UPMC Univ. Paris 6 and CNRS UMR 7589, Paris, France

<sup>40</sup>Universidad Autonoma de Madrid, 28049 Madrid, Spain

<sup>41</sup>Perimeter Institute for Theoretical Physics, Waterloo, Ontario N2L 2Y5, Canada

<sup>42</sup>University of Toronto, Toronto, Ontario M5S 1A7, Canada

<sup>43</sup>IPPP, University of Durham, Durham, DH1 3LE, UK

<sup>44</sup>Columbia University, New York, NY 10027, USA

<sup>45</sup>LPC Clermont-Ferrand, 63177 Aubiere Cedex, France

<sup>46</sup>Instituto de Física Corpuscular, IFIC/CSIC-UVEG, E-46071 Valencia, Spain

<sup>47</sup>University of Amsterdam, 1012 WX Amsterdam, Netherlands

**Abstract** Over the past five or so years a large number of observables have been proposed in the literature, and explored at the LHC experiments, that attempt to utilise the internal structure of highly boosted jets in order to distinguish those that have been initiated by a quark, a gluon or by a heavier particle, such as a Top quark or W boson. This report of the BOOST2013 workshop presents original particle-level studies that attempt to improve our understanding of the relationship between these observables, their complementarity and overlap, and the dependence of this on the underlying jet parameters, especially the jet radius  $R$  and jet  $p_T$ . This is explored in the context of quark/gluon discrimination, boosted W-boson tagging and boosted Top quark tagging.

**Keywords** boosted objects · jet substructure · beyond-the-Standard-Model physics searches · Large Hadron Collider

## 1 Introduction

The characteristic feature of collisions at the LHC is a center-of-mass energy, 7 TeV in 2010 and 2011, of 8 TeV in 2012, and near 14 TeV with the start of the second phase of operation in 2015, that is large compared to even the heaviest of the known particles. Thus these particles (and also previously unknown ones) will often be produced at the LHC with substantial boosts. As a result, when decaying hadronically, these particles will not be observed as multiple jets in the detector, but rather as a single hadronic jet with distinctive internal substructure. This realization has led to a new era of sophistication in our understanding of both standard QCD jets and jets containing the decay of a heavy particle, with an array of new jet observables and detection techniques introduced and studies. To allow the efficient sharing of results from these jet substructure studies a series of BOOST Workshops have been held on a yearly basis: SLAC (2009, [1]), Oxford University (2010, [2]), Princeton University (2011, [3]), IFIC Valencia (2012 [4]), University of Arizona (2013 [5]), and, most recently, University College London (2014 [6]). After each of these meetings Working Groups have functioned during the following year to generate reports highlighting the most interesting new results, including studies of ever maturing details. Previous BOOST reports can be found at [7–9].

This report from BOOST 2013 thus views the study and implementation of jet substructure techniques as a fairly mature field, and focuses on the question of the correlations between the plethora of observables that have been developed and employed, and their dependence on the underlying jet parameters, especially the jet radius  $R$  and jet  $p_T$ . Samples of quark-, gluon-, W- and Top-initiated jets are reconstructed at the particle-level using FASTJET [10], and the performance, in terms of separating signal from background,

of various groomed jet masses and jet substructure observables investigated through Receiver Operating Characteristic (ROC) curves, which show the efficiency to “tag” the signal as a function of the efficiency (or rejection, being  $1/\text{efficiency}$ ) to “tag” the background. In new analyses developed for the report, we investigate the separation of a quark signal from a gluon background (q/g tagging), a W signal from a gluon background (W-tagging) and a Top signal from a mixed quark/gluon QCD background (Top-tagging). In the case of Top-tagging, we also investigate the performance of dedicated Top-tagging algorithms, the HepTopTagger [11] and the Johns Hopkins Tagger [12]. Using multivariate techniques, we study the degree to which the discriminatory information provided by the observables and taggers overlaps, by examining in particular the extent to which the signal-background separation performance increases when two or more variables/taggers are combined, via a Boosted Decision Tree (BDT), into a single discriminant.

**mention that no pile-up, and no detector simulation is used - we are not trying to benchmark the performance of any one algorithm or approach here?**

The report is organized as follows. In Section 2 we describe the generation of the Monte Carlo event samples that we use in the studies that follow. In Section 3 we detail the jet algorithms, observables and taggers investigated in each section of the report, and in Section 4 the multivariate techniques used to combine the one or more of the observables into single discriminants. In Section 5 we describe the q/g-tagging studies, in Section 6 we describe the W-tagging studies, and in Section 7 we describe the Top-tagging studies. Finally we offer some summary of the studies and general conclusions in Section 8.

*This report presents original analyses and discussions pertaining to the performance of and correlations between various jet substructure techniques applied to quark/gluon discrimination, W-boson tagging, and top tagging. The principal organizers of and contributors to the analyses presented in the report are: B. Cooper, S. D. Ellis, M. Freytsis, A. Hornig, A. Larkoski, D. Lopez Mateos, B. Shuve, and N. V. Tran.*

## 2 Monte Carlo Samples

In the below sections the Monte Carlo samples used in the q/g tagging, W tagging and Top tagging sections of this report are described. Note that in all cases the samples used contain no additional proton-proton interactions beyond the hard scatter (no pile-up), and there is no attempt to emulate the degradation in angular and  $p_T$  resolution that would result when reconstructing the jets inside a real detector.

## 2.1 Quark/gluon and $W$ tagging

Samples were generated at  $\sqrt{s} = 8$  TeV for QCD dijets, and for  $W^+W^-$  pairs produced in the decay of a (pseudo) scalar resonance and decaying hadronically. The QCD events were split into subsamples of  $gg$  and  $q\bar{q}$  events, allowing for tests of discrimination of hadronic  $W$  bosons, quarks, and gluons.

Individual  $gg$  and  $q\bar{q}$  samples were produced at leading order (LO) using MADGRAPH5 [13], while  $W^+W^-$  samples were generated using the JHU GENERATOR [14–16] to allow for separation of longitudinal and transverse polarizations. Both were generated using CTEQ6L1 PDFs [17]. The samples were produced in exclusive  $p_T$  bins of width 100 GeV, with the slicing parameter chosen to be the  $p_T$  of any final state parton or  $W$  at LO. At the parton-level the  $p_T$  bins investigated were 300-400 GeV, 500-600 GeV and 1.0-1.1 TeV. Since no matching was performed, a cut on any parton was equivalent. The samples were then all showered through PYTHIA8 (version 8.176) [18] using the default tune 4C [19]. For each of the various samples ( $W, q, g$ ) and  $p_T$  bins, 500,000 events were simulated.

## 2.2 Top tagging

Samples were generated at  $\sqrt{s} = 14$  TeV. Standard Model dijet and top pair samples were produced with SHERPA 2.0.Q60 [20–25], with matrix elements of up to two extra partons matched to the shower. The top samples included only hadronic decays and were generated in exclusive  $p_T$  bins of width 100 GeV, taking as slicing parameter the maximum of the top/anti-top  $p_T$ . The QCD samples were generated with a cut on the leading parton-level jet  $p_T$ , where parton-level jets are clustered with the anti- $k_t$  algorithm and jet radii of  $R = 0.4, 0.8, 1.2$ . The matching scale is selected to be  $Q_{\text{cut}} = 40, 60, 80$  GeV for the  $p_{T\text{min}} = 600, 1000, \text{ and } 1500$  GeV bins, respectively. For the top samples, 100k events were generated in each bin, while 200k QCD events were generated in each bin.

## 3 Jet Algorithms and Substructure Observables

In this section, we define the jet algorithms and observables used in our analysis. Over the course of our study, we considered a larger set of observables, but for the final analysis we eliminated redundant observables for presentation purposes. In Sections 3.1, 3.2, 3.3 and 3.4 we first describe the various jet algorithms, groomers, taggers and other substructure variables used in these studies.

## 3.1 Jet Clustering Algorithms

**Jet clustering:** Jets were clustered using sequential jet clustering algorithms [26] implemented in FASTJET 3.0.3. Final state particles  $i, j$  are assigned a mutual distance  $d_{ij}$  and a distance to the beam,  $d_{iB}$ . The particle pair with smallest  $d_{ij}$  are recombined and the algorithm repeated until the smallest distance is instead the distance to the beam,  $d_{iB}$ , in which case  $i$  is set aside and labelled as a jet. The distance metrics are defined as

$$d_{ij} = \min(p_{Ti}^{2\gamma}, p_{Tj}^{2\gamma}) \frac{\Delta R_{ij}^2}{R^2}, \quad (1)$$

$$d_{iB} = p_{Ti}^{2\gamma}, \quad (2)$$

where  $\Delta R_{ij}^2 = (\Delta\eta)^2 + (\Delta\phi)^2$ . In this analysis, we use the anti- $k_t$  algorithm ( $\gamma = -1$ ) [27], the Cambridge/Aachen (C/A) algorithm ( $\gamma = 0$ ) [28, 29], and the  $k_t$  algorithm ( $\gamma = 1$ ) [30, 31], each of which has varying sensitivity to soft radiation in defining the jet.

**Qjets:** We also perform non-deterministic jet clustering [32, 33]. Instead of always clustering the particle pair with smallest distance  $d_{ij}$ , the pair selected for combination is chosen probabilistically according to a measure

$$P_{ij} \propto e^{-\alpha(d_{ij}-d_{\min})/d_{\min}}, \quad (3)$$

where  $d_{\min}$  is the minimum distance for the usual jet clustering algorithm at a particular step. This leads to a different cluster sequence for the jet each time the Qjet algorithm is used, and consequently different substructure properties. The parameter  $\alpha$  is called the rigidity and is used to control how sharply peaked the probability distribution is around the usual, deterministic value. The Qjets method uses statistical analysis of the resulting distributions to extract more information from the jet than can be found in the usual cluster sequence.

## 3.2 Jet Grooming Algorithms

**Pruning:** Given a jet, re-cluster the constituents using the C/A algorithm. At each step, proceed with the merger as usual unless both

$$\frac{\min(p_{Ti}, p_{Tj})}{p_{Tij}} < z_{\text{cut}} \text{ and } \Delta R_{ij} > \frac{2m_j}{p_{Tj}} R_{\text{cut}}, \quad (4)$$

in which case the merger is vetoed and the softer branch discarded. The default parameters used for pruning [34] in this study are  $z_{\text{cut}} = 0.1$  and  $R_{\text{cut}} = 0.5$ . One advantage of pruning is that the thresholds used to veto soft, wide-angle radiation scale with the jet kinematics, and so the algorithm is expected to perform comparably over a wide range of momenta.

**Trimming:** Given a jet, re-cluster the constituents into sub-jets of radius  $R_{\text{trim}}$  with the  $k_t$  algorithm. Discard all subjects  $i$  with

$$p_{Ti} < f_{\text{cut}} p_{TJ}. \quad (5)$$

The default parameters used for trimming [35] in this study are  $R_{\text{trim}} = 0.2$  and  $f_{\text{cut}} = 0.03$ .

**Filtering:** Given a jet, re-cluster the constituents into sub-jets of radius  $R_{\text{filt}}$  with the C/A algorithm. Re-define the jet to consist of only the hardest  $N$  subjects, where  $N$  is determined by the final state topology and is typically one more than the number of hard prongs in the resonance decay (to include the leading final-state gluon emission) [36]. While we do not independently use filtering, it is an important step of the HEPTopTagger to be defined later.

**Soft drop:** Given a jet, re-cluster all of the constituents using the C/A algorithm. Iteratively undo the last stage of the C/A clustering from  $j$  into subjects  $j_1, j_2$ . If

$$\frac{\min(p_{T1}, p_{T2})}{p_{T1} + p_{T2}} < z_{\text{cut}} \left( \frac{\Delta R_{12}}{R} \right)^\beta, \quad (6)$$

discard the softer subject and repeat. Otherwise, take  $j$  to be the final soft-drop jet [37]. Soft drop has two input parameters, the angular exponent  $\beta$  and the soft-drop scale  $z_{\text{cut}}$ , with default value  $z_{\text{cut}} = 0.1$ . **ED: Soft-drop actually functions as a tagger when  $\beta = -1$**

### 3.3 Jet Tagging Algorithms

**Modified Mass Drop Tagger:** Given a jet, re-cluster all of the constituents using the C/A algorithm. Iteratively undo the last stage of the C/A clustering from  $j$  into subjects  $j_1, j_2$  with  $m_{j_1} > m_{j_2}$ . If either

$$m_{j_1} > \mu m_j \text{ or } \frac{\min(p_{T1}^2, p_{T2}^2)}{m_j^2} \Delta R_{12}^2 < y_{\text{cut}}, \quad (7)$$

then discard the branch with the smaller transverse mass  $m_T = \sqrt{m_i^2 + p_{Ti}^2}$ , and re-define  $j$  as the branch with the larger transverse mass. Otherwise, the jet is tagged. If de-clustering continues until only one branch remains, the jet is untagged [38]. In this study we use by default  $\mu = 1.0$  and  $y_{\text{cut}} = 0.1$ .

**Johns Hopkins Tagger:** Re-cluster the jet using the C/A algorithm. The jet is iteratively de-clustered, and at each step the softer prong is discarded if its  $p_T$  is less than  $\delta_p p_{T\text{jet}}$ . This continues until both prongs are harder than the  $p_T$  threshold, both prongs are softer than the  $p_T$  threshold, or if they are too close ( $|\Delta\eta_{ij}| + |\Delta\phi_{ij}| < \delta_R$ ); the jet is rejected if either of the latter conditions apply. If both are harder than the

$p_T$  threshold, the same procedure is applied to each: this results in 2, 3, or 4 subjects. If there exist 3 or 4 subjects, then the jet is accepted: the top candidate is the sum of the subjects, and  $W$  candidate is the pair of subjects closest to the  $W$  mass [12]. The output of the tagger is  $m_t$ ,  $m_W$ , and  $\theta_h$ , a helicity angle defined as the angle, measured in the rest frame of the  $W$  candidate, between the top direction and one of the  $W$  decay products. The two free input parameters of the Johns Hopkins tagger in this study are  $\delta_p$  and  $\delta_R$ , defined above.

**HEPTopTagger:** Re-cluster the jet using the C/A algorithm. The jet is iteratively de-clustered, and at each step the softer prong is discarded if  $m_1/m_{12} > \mu$  (there is not a significant mass drop). Otherwise, both prongs are kept. This continues until a prong has a mass  $m_i < m$ , at which point it is added to the list of subjects. Filter the jet using  $R_{\text{filt}} = \min(0.3, \Delta R_{ij})$ , keeping the five hardest subjects (where  $\Delta R_{ij}$  is the distance between the two hardest subjects). Select the three subjects whose invariant mass is closest to  $m_t$  [11]. The output of the tagger is  $m_t$ ,  $m_W$ , and  $\theta_h$ , a helicity angle defined as the angle, measured in the rest frame of the  $W$  candidate, between the top direction and one of the  $W$  decay products. The two free input parameters of the HEPTopTagger in this study are  $m$  and  $\mu$ , defined above.

**Top Tagging with Pruning:** For comparison with the other top taggers, we add a  $W$  reconstruction step to the trimming algorithm described above. A  $W$  candidate is found as follows: if there are two subjects, the highest-mass subject is the  $W$  candidate (because the  $W$  prongs end up clustered in the same subject); if there are three subjects, the two subjects with the smallest invariant mass comprise the  $W$  candidate. In the case of only one subject, no  $W$  is reconstructed.

**Top Tagging with Trimming:** For comparison with the other top taggers, we add a  $W$  reconstruction step to the trimming algorithm described above. A  $W$  candidate is found as follows: if there are two subjects, the highest-mass subject is the  $W$  candidate (because the  $W$  prongs end up clustered in the same subject); if there are three subjects, the two subjects with the smallest invariant mass comprise the  $W$  candidate. In the case of only one subject, no  $W$  is reconstructed.

### 3.4 Other Jet Substructure Observables

Jet substructure observables are computed using ungroomed jets.

**Qjet mass volatility:** As described above, Qjet algorithms re-cluster the same jet non-deterministically to obtain a collection of interpretations of the jet. For each jet interpretation, the pruned jet mass is computed with the default pruning parameters. The mass volatility,  $\Gamma_{\text{Qjet}}$ , is defined as [32]

$$\Gamma_{\text{Qjet}} = \frac{\sqrt{\langle m_J^2 \rangle - \langle m_J \rangle^2}}{\langle m_J \rangle}, \quad (8)$$

where averages are computed over the Qjet interpretations. We use a rigidity parameter of  $\alpha = 0.1$  (although other studies suggest a smaller value of  $\alpha$  may be optimal [32, 33]), and 25 trees per event for all of the studies presented here.

**$N$ -subjettiness:**  $N$ -subjettiness [39] quantifies how well the radiation in the jet is aligned along  $N$  directions. To compute  $N$ -subjettiness,  $\tau_N^{(\beta)}$ , one must first identify  $N$  axes within the jet. Then,

$$\tau_N = \frac{1}{d_0} \sum_i p_{Ti} \min(\Delta R_{1i}^\beta, \dots, \Delta R_{Ni}^\beta), \quad (9)$$

where distances are between particles  $i$  in the jet and the axes,

$$d_0 = \sum_i p_{Ti} R^\beta \quad (10)$$

and  $R$  is the jet clustering radius. The exponent  $\beta$  is a free parameter. There is also some choice in how the axes used to compute  $N$ -subjettiness are determined. The optimal configuration of axes is the one that minimizes  $N$ -subjettiness; recently, it was shown that the “winner-takes-all” (WTA) axes can be easily computed and have superior performance compared to other minimization techniques [40]. We use both the WTA and one-pass  $k_t$  optimization axes in our analyses.

A more powerful discriminant is often the ratio,

$$\tau_{N,N-1} \equiv \frac{\tau_N}{\tau_{N-1}}. \quad (11)$$

While this is not an infrared-collinear (IRC) safe observable, it is calculable [41] and can be made IRC safe with a loose lower cut on  $\tau_{N-1}$ .

**Energy correlation functions:** The transverse momentum version of the energy correlation functions are defined as [42]:

$$\text{ECF}(N, \beta) = \sum_{i_1 < i_2 < \dots < i_N \in j} \left( \prod_{a=1}^N p_{Ti_a} \right) \left( \prod_{b=1}^{N-1} \prod_{c=b+1}^N \Delta R_{i_b i_c} \right)^\beta, \quad (12)$$

where  $i$  is a particle inside the jet. It is preferable to work in terms of dimensionless quantities, particularly the energy correlation function double ratio:

$$C_N^{(\beta)} = \frac{\text{ECF}(N+1, \beta) \text{ECF}(N-1, \beta)}{\text{ECF}(N, \beta)^2}. \quad (13)$$

This observable measures higher-order radiation from leading order substructure.

## 4 Multivariate Analysis Techniques

Multivariate techniques are used to combine variables into an optimal discriminant. In all cases variables are combined using a boosted decision tree (BDT) as implemented in the TMVA package [43]. We use the BDT implementation including gradient boost. An example of the BDT settings are as follows:

- NTrees=1000
- BoostType=Grad
- Shrinkage=0.1
- UseBaggedGrad=F
- nCuts=10000
- MaxDepth=3
- UseYesNoLeaf=F
- nEventsMin=200

Exact parameter values are chosen to best reduce the effect of overtraining. Additionally, the simulated data were split into training and testing samples and comparisons of the BDT output were compared to reduced the effect of overtraining as well.

## 5 Quark-Gluon Discrimination

In this section, we examine the differences between quark- and gluon-initiated jets in terms of substructure variables, and to determine to what extent these variables are correlated. Along the way, we provide some theoretical understanding of these observables and their performance. The motivation for these studies comes not only from the desire to “tag” a jet as originating from a quark or gluon, but also to improve our understanding of the quark and gluon components of the QCD backgrounds relative to boosted resonances. While recent studies have suggested that quark/gluon tagging efficiencies depend highly on the Monte Carlo generator used[44, 45], we are more interested in understanding the scaling performance with  $p_T$  and  $R$ , and the correlations between observables, which are expected to be treated consistently within a single shower scheme.

### 5.1 Methodology

These studies use the  $qq$  and  $gg$  MC samples, described previously in Section 2. The showered events were clustered with FASTJET 3.03 using the anti- $k_T$  algorithm with jet radii of  $R = 0.4, 0.8, 1.2$ . In both signal (quark) and background (gluon) samples, an upper and lower cut on the leading jet  $p_T$  is applied after showering/clustering, to ensure similar  $p_T$  spectra for signal and background in each  $p_T$  bin. The bins in leading jet  $p_T$  that are considered are 300-400 GeV, 500-600 GeV, 1.0-1.1 TeV, for the 300-400 GeV, 500-600



GeV, 1.0-1.1 TeV parton  $p_T$  slices respectively. Various jet grooming approaches are applied to the jets, as described in Section 3.4. Only leading and subleading jets in each sample are used. The following observables are studied in this section:

- The number of constituents ( $N_{\text{constits}}$ ) in the jet.
- The pruned Qjet mass volatility,  $\Gamma_{\text{Qjet}}$ .
- 1-point energy correlation functions,  $C_1^\beta$  with  $\beta = 0, 1, 2$ .
- 1-subjettiness,  $\tau_1^\beta$  with  $\beta = 1, 2$ . The  $N$ -subjettiness axes are computed using one-pass  $k_t$  axis optimization.
- The ungroomed jet mass,  $m$ .

We will see below that, in terms of their jet-by-jet correlations and their ability to separate quark initiated jets from gluon initiated jets (hereafter called simply quark jets and gluon jets), these observables fall into five classes. The first three,  $N_{\text{constits}}$ ,  $\Gamma_{\text{Qjet}}$  and  $C_1^{\beta=0}$ , form classes by themselves (Classes I to III) in the sense that they each carry some independent information about a jet and, when combined, provide substantially better quark jet and gluon jet separation than either observable by itself. Of the remaining observables,  $C_1^{\beta=1}$  and  $\tau_1^{\beta=1}$  comprise a single class (Class IV) in the sense that they exhibit similar distributions when applied to a sample of jets, their jet-by-jet values are highly correlated, they exhibit very similar power to separate quark jets and gluon jets (with very similar dependence on the jet parameters  $R$  and  $p_T$ ) and this separation power is essentially unchanged when they are combined. The fifth class (Class V) is composed of  $C_1^{\beta=2}$ ,  $\tau_1^{\beta=2}$  and the (ungroomed) jet mass. Again the issue is that jet-by-jet correlations are strong (even though the individual observable distributions are somewhat different), quark versus gluon separation power is very similar (including the  $R$  and  $p_T$  dependence) and little is achieved by combining more than one of these observables. This class structure is not surprising given that within a class the observables exhibit very similar dependence on the kinematics of the underlying jet constituents. For example, the members of Class V are constructed from a sum over pairs of constituents using products of the energy of each member of the pair times the angular separation squared for the pair (for the mass case think in terms of mass squared with small angular separations). By the same argument the Class IV and Class V observables will be seen to be more similar than any other pair of classes, differing only in the power ( $\beta$ ) of the dependence on the angular separations, which will produce small but detectable differences. We will return to a more complete discussion of jet masses at the end of Section 5.

## 5.2 Single Variable Discrimination

The quark and gluon distributions of different substructure observables are shown in Figure 1, which already illustrates at least some of the points about the Classes made above. At a fundamental level the primary difference between quark jets and gluon jets is the color charge of the initiating parton, typically expressed in terms of the ratio of the corresponding Casimir factors  $C_F/C_A = 4/9$ . Since the quark has the smaller color charge, it will radiate less than a corresponding gluon and the resulting jet will contain fewer constituents. This difference is clearly indicated in Figure 1(a), suggesting that simply counting constituents will provide good separation between quark and gluon jets. In fact, among the observables considered, one can see by eye that  $N_{\text{constits}}$  should provide the highest separation power, *i.e.*, the quark and gluon distributions are most distinct, as was originally noted in [45, 46]. Figure 1 further suggests that  $C_1^{\beta=0}$  should provide the next best separation followed by  $C_1^{\beta=1}$ , as was also found by the CMS and ATLAS Collaborations[44, 47].

To more quantitatively study the power of each observable as a discriminator for quark/gluon tagging, ROC curves are built by scanning each distribution and plotting the background efficiency (to select gluon jets) vs. the signal efficiency (to select quark jets). Figure 2 shows these ROC curves for all of the substructure variables shown in Figure 1, along with the ungroomed mass, representing the best performing mass variable, for  $R=0.4, 0.8$  and  $1.2$  jets in the  $p_T = 300 - 400$  GeV bin. In addition, the ROC curve for a tagger built from a BDT combination of all the variables (see Section 4) is shown. Clearly, and as suggested earlier,  $n_{\text{constits}}$  is the best performing variable for all  $R$ s, even though  $C_1^{\beta=0}$  is close, particularly for  $R=0.8$ . Most other variables have similar performance, except  $\Gamma_{\text{Qjet}}$ , which shows significantly worse discrimination (this may be due to our choice of rigidity  $\alpha = 0.1$ , with other studies suggesting that a smaller value, such as  $\alpha = 0.01$ , produces better results[32, 33]). The combination of all variables shows somewhat better discrimination, and we will discuss in more detail below the correlations between the observables and their impact on the combined discrimination power.

We now examine how the performance of the substructure observables changes with  $p_T$  and  $R$ . To present the results in a “digestible” fashion we will focus on the gluon jet “rejection” factor,  $1/\epsilon_{\text{bkg}}$ , for a quark signal efficiency,  $\epsilon_{\text{sig}}$ , of 50%. We can use the values of  $1/\epsilon_{\text{bkg}}$  generated for the 9 kinematic points introduced above ( $R = 0.4, 0.8, 1.2$  and the 100 GeV  $p_T$  bins with lower limits  $p_T = 300$  GeV, 500 GeV, 1000 GeV) to generate surface plots. The surface plots in Figure 3 indicate both the level of gluon rejection and the variation with  $p_T$  and  $R$  for each of the studied single observable. The color shading is defined so that a change in color corresponds to a change of about 0.4 in  $1/\epsilon_{\text{bkg}}$ .

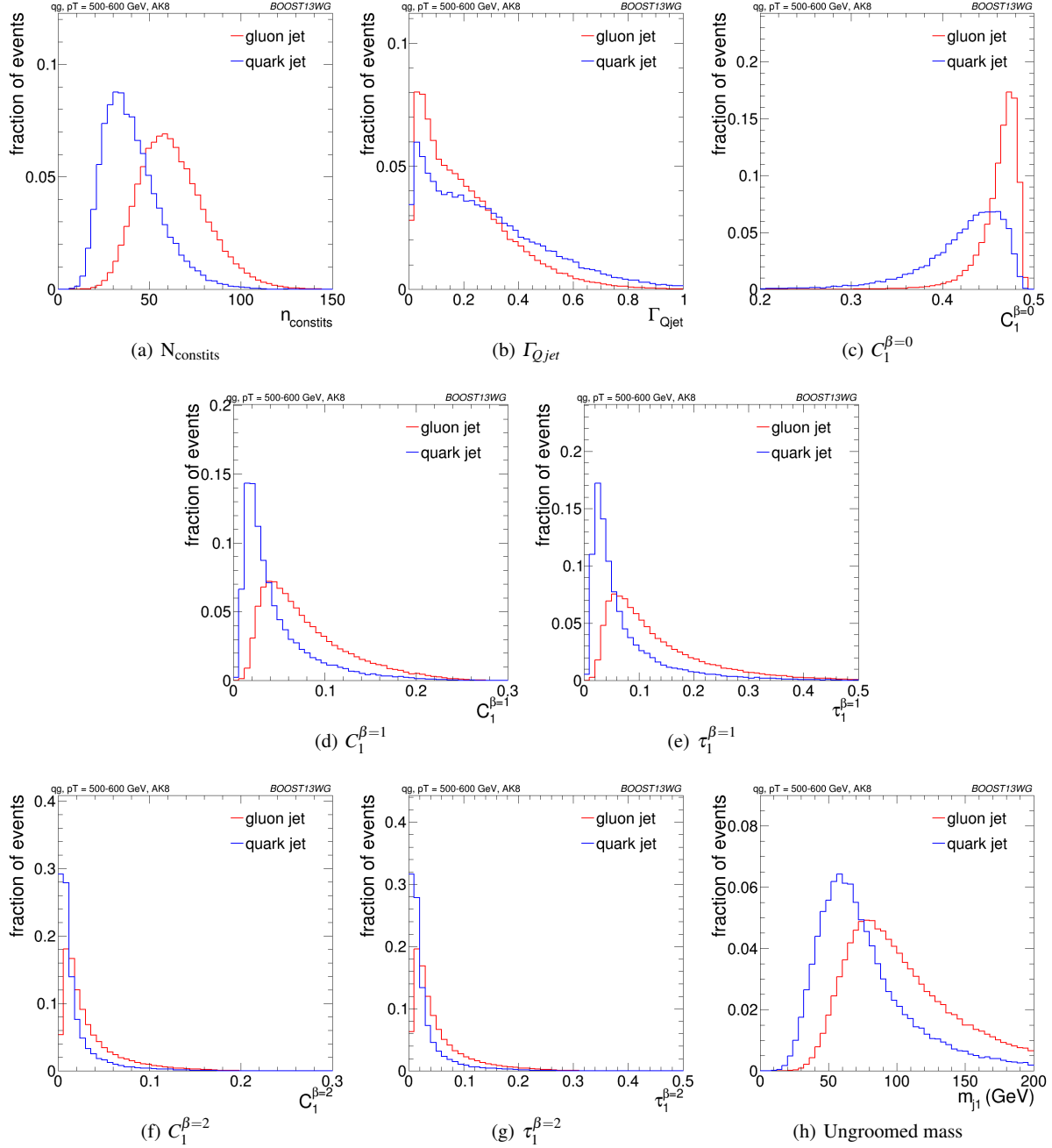


**Fig. 1** Comparisons of quark and gluon distributions of different substructure variables (organized by Class) for leading jets in the  $p_T = 500 - 600$  GeV bin using the anti- $k_T$   $R = 0.8$  algorithm.

The colors have the same correlation with the magnitude of  $1/\epsilon_{\text{bkg}}$  in all of the plots, but repeat after a change of about 4. Thus “blue” corresponds to a value of about 2.5 in Figure 3(b) and the values 6.5 and 10.5 in Figure 3(a), while “yellow” corresponds to about 5 in Figures 3(c) to (h) and about 9 in Figure 3(a).

We see, as expected, that the numerically largest rejection rates occur for the observable  $N_{\text{constits}}$  in Figure 3(a), where the rejection factor is in the range 6 to 11 and varies

rather dramatically with  $R$ . As  $R$  increases the jet collects more constituents from the underlying event, which are the same for quark and gluon jets, and the separation power decreases. At large  $R$ , there is some improvement with increasing  $p_T$  due to the enhanced radiation, which does distinguish quarks from gluons. Figure 3(b) confirms the limited efficacy of the single observable  $\Gamma_{Qjet}$  (at least for our parameter choices) with a rejection rate only in the range 2.5 to 2.8. On the other hand, this observable probes a very different

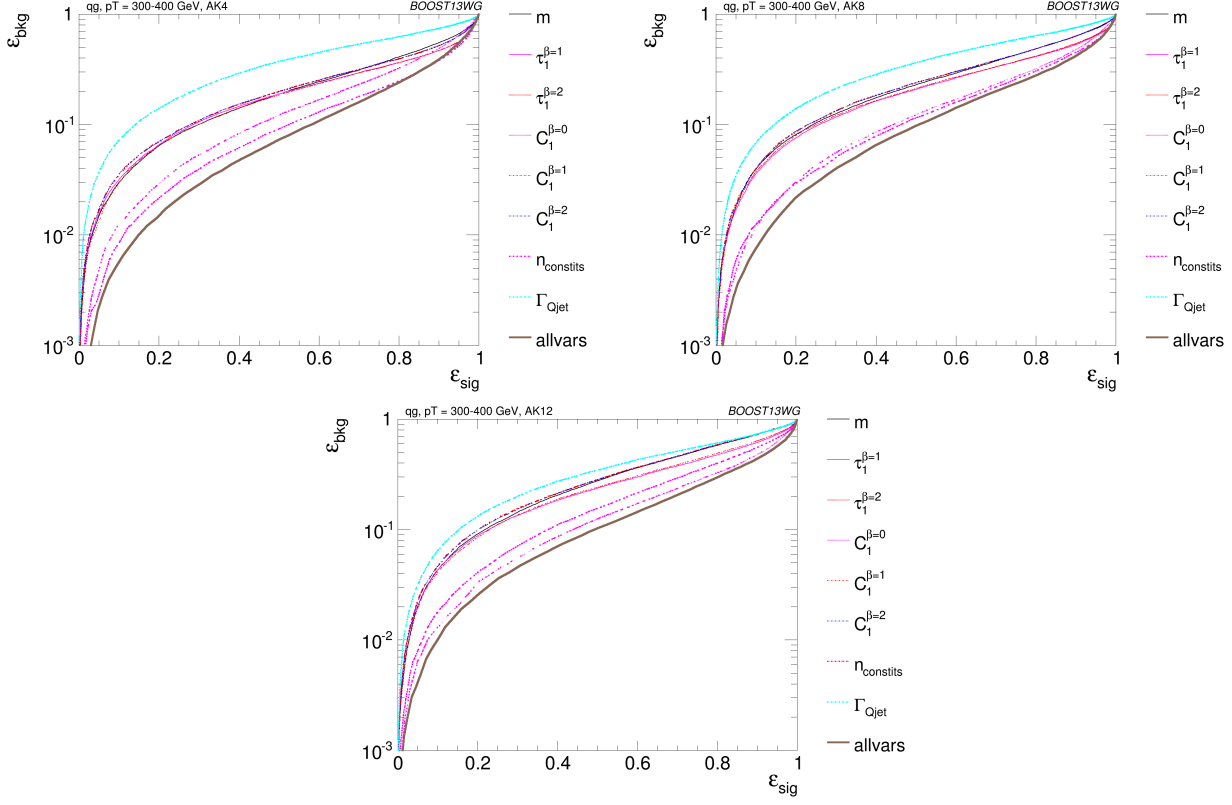


**Fig. 2** The ROC curve for all single variables considered for quark-gluon discrimination in the  $p_T$  300-400 GeV bin using the anti- $k_T$   $R=0.4, 0.8$  and 1.2 algorithm.

property of jet substructure, *i.e.*, the sensitivity to detailed changes in the grooming procedure, and this difference is suggested by the distinct  $R$  and  $p_T$  dependence illustrated in Figure 3(b). The rejection rate increases with increasing  $R$  and decreasing  $p_T$ , since the distinction between quark and gluon jets for this observable arises from the relative importance of the one “hard” gluon emission configuration. The role of this contribution is enhanced for both decreasing  $p_T$  and increasing  $R$ . Figure 3(c) indicates that the observable  $C_1^{\beta=0}$  can, by itself, provide a rejection rate in the range 7.8 to 8.6 (intermediate between the two previous observables) and again with distinct  $R$  and  $p_T$  dependence. In this case the rejection rate decreases slowly with increasing  $R$  ( $\beta = 0$  explicitly means that the angular dependence is much reduced), while the rejection rate peaks at intermediate  $p_T$  values (an effect visually enhanced by the limited number of  $p_T$  values included). Both the distinct values of the rejection rates and the differing  $R$  and  $p_T$  dependence serve to confirm that these three observables tend to probe independent features of the quark and gluon jets.

Figures 3(d) and (e) serve to confirm the very similar properties of the Class IV observables  $C_1^{\beta=1}$  and  $\tau_1^{\beta=1}$  (already suggested in Figures 1(d) and (e)) with essentially identical rejection rates (4.1 to 5.4) and identical  $R$  and  $p_T$  dependence (a slow decrease with increasing  $R$  and an even

slower increase with increasing  $p_T$ ). A similar conclusion for the Class V observables  $C_1^{\beta=2}$ ,  $\tau_1^{\beta=2}$  and  $m$  with similar rejection rates in the range 3.5 to 5.3 and very similar  $R$  and  $p_T$  dependence (a slow decrease with increasing  $R$  and an even slower increase with increasing  $p_T$ ). Arguably, drawing a distinction between the Class IV and Class V observables, is a fine point, but the color shading does suggest some distinction from the slightly smaller rejection rate in Class V. Again the strong similarities between the plots within the second and third rows in Figure 3 speaks to the common properties of the observables within the two classes.

In summary, the overall discriminating power between quark and gluon jets tends to decrease with increasing  $R$ , except for the  $\Gamma_{Qjet}$  observable, presumably primarily due to the increasing contamination from the underlying event. Since the construction of the  $\Gamma_{Qjet}$  observable explicitly involves pruning away the soft, large angle constituents, it is not surprising that it exhibits different  $R$  dependence. In general the discriminating power increases slowly and monotonically with  $p_T$  (except for the  $\Gamma_{Qjet}$  and  $C_1^{\beta=0}$  observables) presumably because there is overall more (color charge related) radiation as  $p_T$  increasing providing some increase in discrimination (except for the  $\Gamma_{Qjet}$  observable). We turn now to the question of the impact of employing more than one observable at a time.



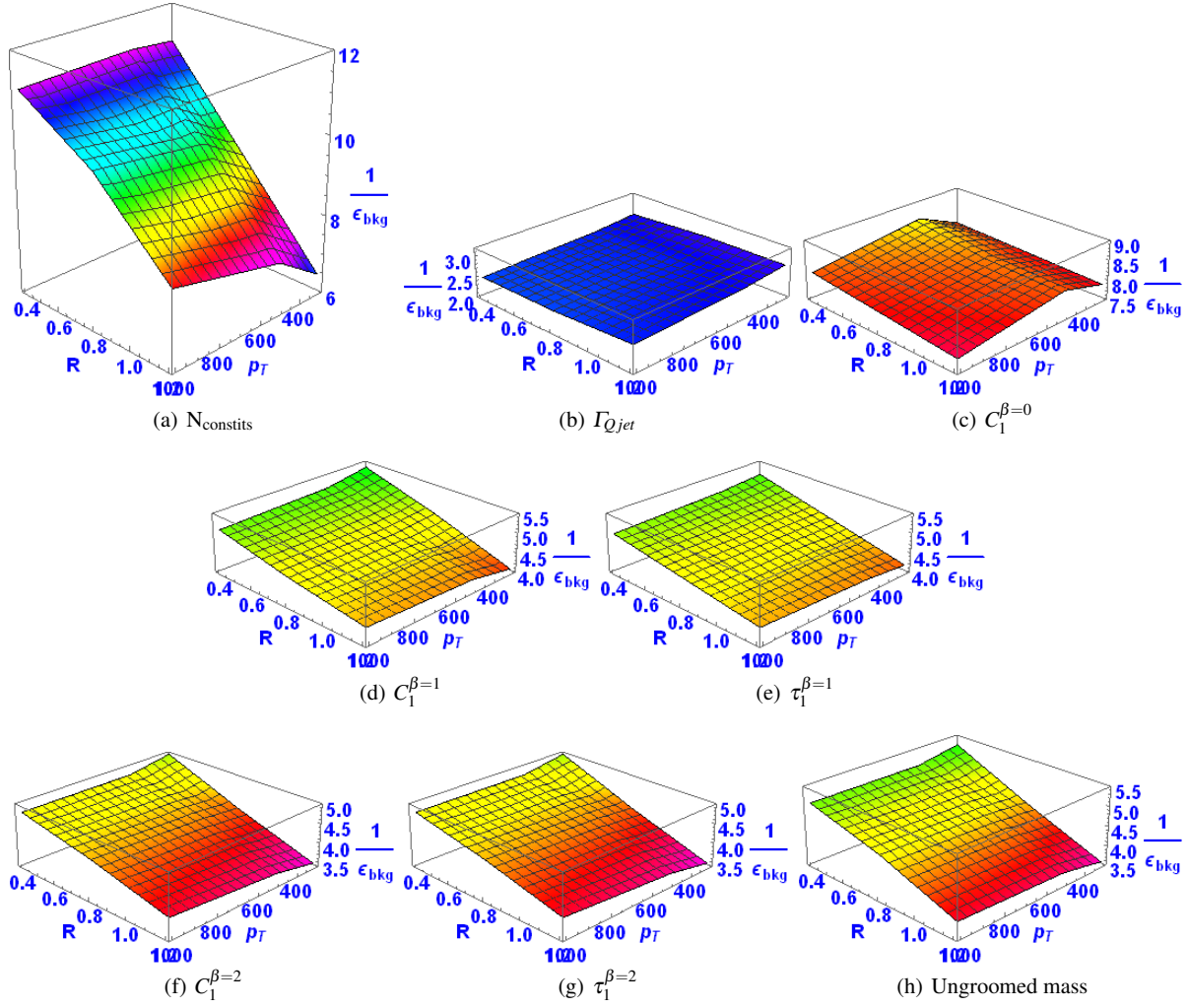


**Fig. 3** Surface plots of  $1/\epsilon_{\text{bkg}}$  for all single variables considered for quark-gluon discrimination as functions of  $R$  and  $p_T$ .

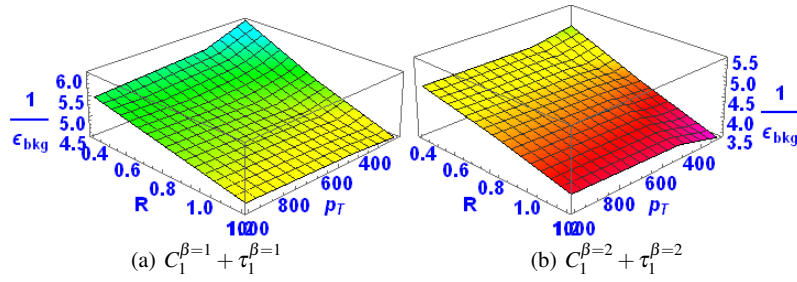


**Fig. 4** Surface plots of  $1/\epsilon_{\text{bkg}}$  for the indicated pairs of variables from Classes IV and V considered for quark-gluon discrimination as functions of  $R$  and  $p_T$ .

### 5.3 Combined Performance and Correlations

The quark/gluon tagging performance can be further improved over cuts on single observables by combining multiple observables in a BDT; due to the challenging nature of  $q/g$ -tagging, any improvement in performance with multivariable techniques could be critical for certain analyses,

and the improvement could be more substantial in data than the marginal benefit found in MC and shown in Fig. 2. Furthermore, insight can be gained into the features allowing for quark/gluon discrimination if the origin of the improvement is understood. To quantitatively study this improvement, we build quark/gluon taggers from every pair-wise combination of variables studied in the previous section for

comparison with the all-variable combination. To illustrate the results achieved in this way we will exhibit the same sort 2D of surface plots as in Figure 3. Based on our discussion of the correlated properties of observables within a single class, we expect little improvement in the rejection rate when combining observables from the same class and substantial improvement when combining observables from different classes.

Figure 4 shows pairwise plots for (a) Class IV and (b) Class V. Comparing to the corresponding plots in Figure 3 we see that combining  $C_1^{\beta=1} + \tau_1^{\beta=1}$  provides a small improvement in the rejection rate of about 10% (0.5 out of 5) with essentially no change in the  $R$  and  $p_T$  dependence, while combining  $C_1^{\beta=2} + \tau_1^{\beta=2}$  yields a rejection rate that is essentially identical to the single observable rejection rate for all  $R$  and  $p_T$  values (with a similar conclusion if one of these observables is replaced with the ungroomed jet mass  $m$ ). This again confirms that expectation that the observables within a single class effectively probe the same jet properties.

Next we consider the cross-class pairs of observables indicated in Figure 5, where only one member of Classes IV and V is included. As expected the largest rejection rates are obtained from combining another observable with  $N_{\text{constits}}$  (Figures 5(a) to (d)). In general, the rates are larger than for the single variable case with similar  $R$  and  $p_T$  dependence. In particular, the pair  $N_{\text{constits}} + C_1^{\beta=1}$  yields rejection rates in the range 6.4 to 14.7 (6.4 to 15 for the similar case  $N_{\text{constits}} + \tau_1^{\beta=1}$ ) with the largest values at small  $R$  and large  $p_T$ . The other pairings with  $N_{\text{constits}}$  (except with  $\tau_1^{\beta=1}$ ) yield smaller rejection rates and smaller dynamic range. The pair  $N_{\text{constits}} + C_1^{\beta=0}$  (Figure 5(d)) exhibits the smallest range of rates (8.3 to 11.3) suggesting that the differences between these two observables serve to substantially reduce the  $R$  and  $p_T$  dependence for the pair, but this also reduces the possible optimization. The other pairs indicated exhibit similar behavior. The pair rejection rates are somewhat better than either observable alone (since we are always combining from different classes), and the  $R$  and  $p_T$  dependence is generally similar to the more variant single observable case. The smallest  $R$  and  $p_T$  variation always occurs when pairing with  $C_1^{\beta=0}$ . Changing any of the observables in these pairs with a different observable in the same class (e.g.,  $C_1^{\beta=2}$  for  $\tau_1^{\beta=2}$  produces very similar results (at the few percent level) Figure 5(k) shows the result of a BDT analysis including all of the current observables with rejection rates in the range 10.5 to 17.1. This is a somewhat narrower range than in Figure 5(b) but with somewhat larger maximum values.

Another way to present the same data but by fixing  $R$  and  $p_T$  and showing all single observables and pairs of observables at once is in terms of the “matrices” indicated in Figures 6 and 7. The numbers in each cell are the now familiar

rejection factor values of  $1/\epsilon_{\text{bkg}}$  (gluons) for  $\epsilon_{\text{sig}} = 50\%$  (quarks). Figure 6 corresponds  $p_T = 1 - 1.1$  TeV and  $R = 0.4, 0.8, 1.2$ , while Figure 7 is for  $R = 0.4$  and the 3  $p_T$  bins. The actual numbers should be familiar from the discussion above with the single observable rejection rates appearing on the diagonal and the pairwise results off the diagonal. The correlations indicated by the shading should be largely understood as indicating the organization of the observables into the now familiar classes. The all-observable (BDT) result appears as the number at the lower right in each plot.

#### 5.4 QCD Jet Masses

To close the discussion of the tagging of jets as either quark jets or gluon jets we provide some insight into the behavior of the masses of such QCD jets, both with and without grooming. Recall that, in practice, an identified jet is simply a list of constituents, *i.e.*, objects in the detector. To the extent that the masses of these individual constituents are irrelevant, typically because the detected constituents are relativistic, each constituent has a “well” defined 4-momentum. It follows that the 4-momentum of the jet is simply the sum of the 4-momenta of the constituents and its square is the jet mass squared. We have already seen one set of jet mass distributions in Figure 1(h) for quark and gluon jets found with the anti- $k_T$  algorithm with  $R = 0.8$  and  $p_T$  in the bin 500-600 GeV. If we consider the mass distributions for other kinematic points (other values of  $R$  and  $p_T$ ), we observe considerable variation but that variation can largely be removed by plotting versus the scaled variable  $m/p_T/R$ . Simply on dimensional grounds we know that jet mass must scale essentially linearly with  $p_T$ , with the remaining  $p_T$  dependence arising predominantly from the running of the coupling,  $\alpha_s(p_T)$ . The  $R$  dependence is also crudely linear as the mass scales approximately with the largest angular opening between any 2 constituents and that is set by  $R$ . The mass distributions for quark and gluon jets versus  $m/p_T/R$  for all of our kinematic points are indicated in Figure 8, where we use a logarithmic scale on the y-axis to clearly exhibit the behavior of these distributions over a large dynamic range. We observe that the distributions for the different kinematic points do approximately scale, *i.e.*, the simple arguments above do capture most of the variation with  $R$  and  $p_T$ . We will consider shortly an explanation of the residual non-scaling.

Several features of Figure 8 can be easily understood. The distributions all cut-off rapidly for  $m/p_T/R > 0.5$ , which is understood as the precise limit (maximum mass) for a jet composed of just 2 constituents. As expected from the soft and collinear singularities in QCD, the mass distribution peaks at small mass values. The actual peak is “pushed” away from the origin by the so-called Sudakov form factor. Summing the corresponding logarithmic structure (sin-

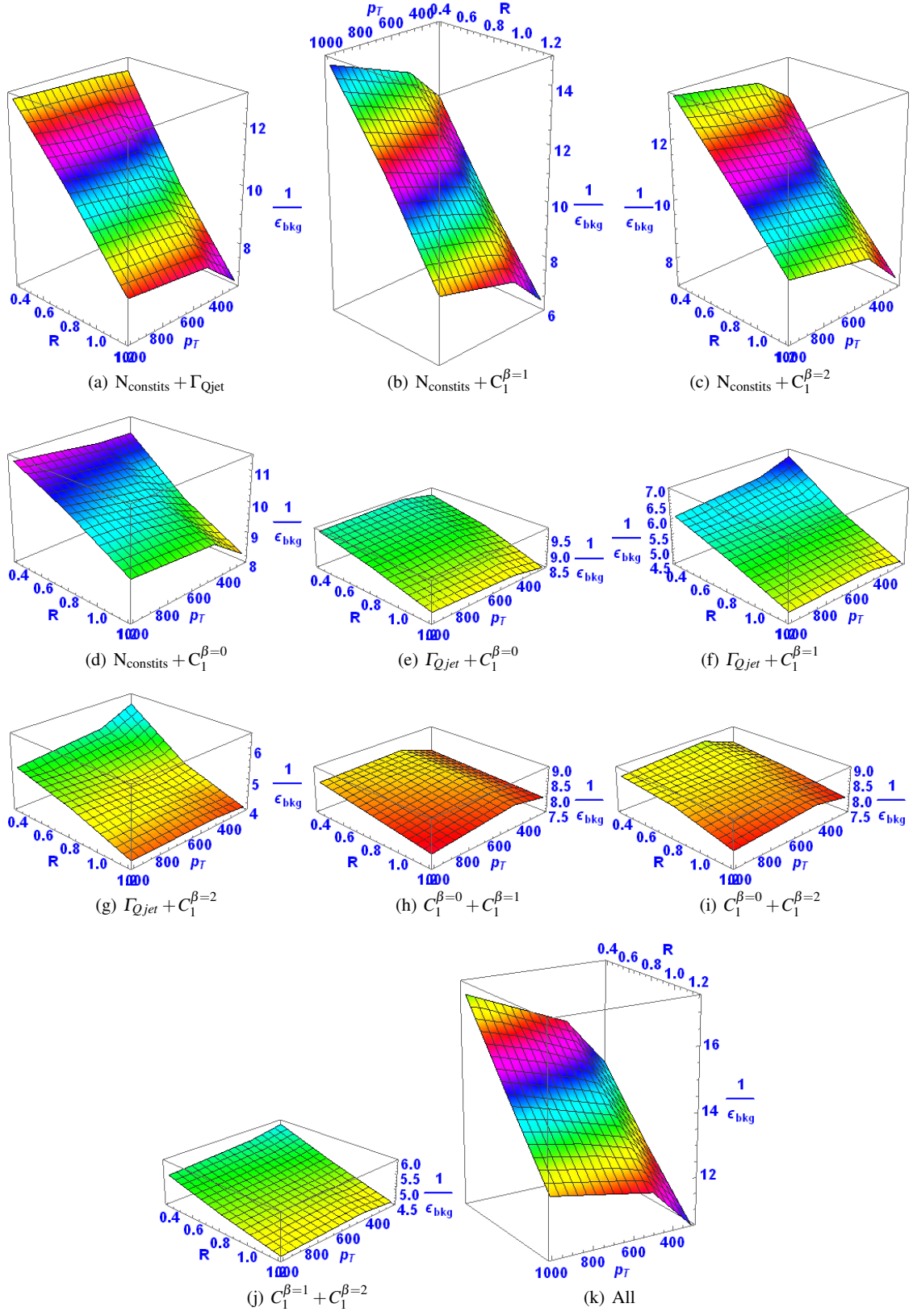


**Fig. 5** Surface plots of  $1/\epsilon_{\text{bkg}}$  for the indicated pairs of variables from different classes considered for quark-gluon discrimination as functions of  $R$  and  $p_T$ .

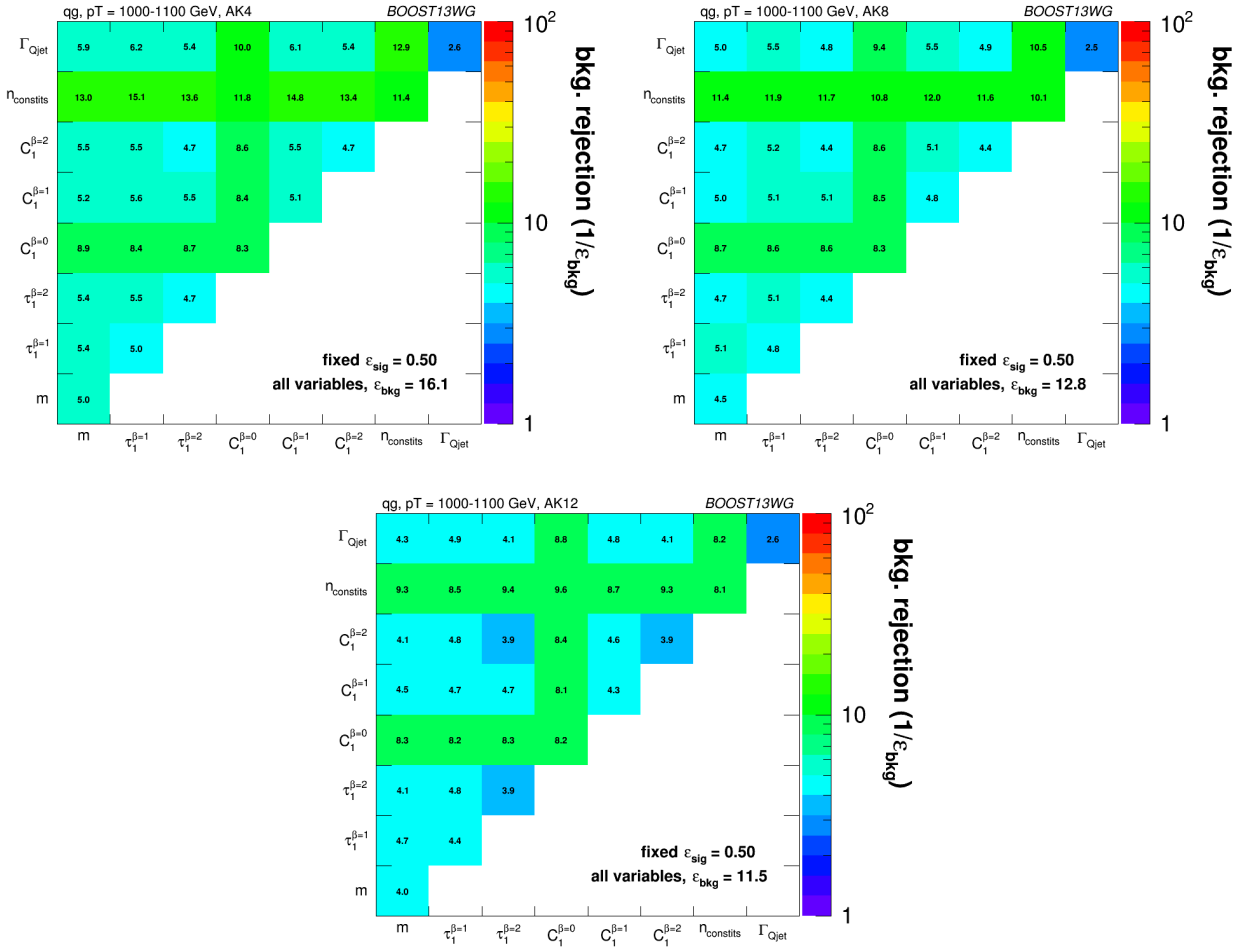


**Fig. 6** Gluon rejection defined as  $1/\epsilon_{\text{gluon}}$  when using each 2-variable combination as a tagger with 50% acceptance for quark jets. Results are shown for jets with  $p_T = 1 - 1.1$  TeV and for (top left)  $R = 0.4$ ; (top right)  $R = 0.8$ ; (bottom)  $R = 1.2$ . The rejection obtained with a tagger that uses all variables is also shown in the plots.

gular in both  $p_T$  and angle) to all orders in perturbation theory yields a distribution that is highly damped as the mass vanishes. In words, there is precisely *zero* probability that a color parton emits *no* radiation (and the resulting jet has zero mass). The large mass “shoulder” ( $0.3 < m/p_T/R < 0.5$ ) is driven largely by the presence of a single large angle, energetic emission in the underlying QCD shower, *i.e.*, this regime is quite well described by low-order perturbation theory. (The shoulder label will be more clear after we groom the jet.) In contrast, we should think of the peak region as corresponding to multiple soft emissions. This simple (approximate) picture provides an understanding of the bulk of the differences between the quark and gluon jet mass distributions. Since the probability of the single large angle, energetic emission is proportional to the color charge, the gluon distribution should be enhanced in this region by a factor of about  $C_A/C_F = 9/4$ , consistent with what is observed in Figure 8. Similarly the exponent in the Sudakov damping factor for the gluon jet mass distribution is enhanced by the

same factor, leading to a peak “pushed” further from the origin. So the gluon jet mass distribution exhibits a larger average jet mass than the quark jet, with a larger relative contribution arising from the perturbative shoulder region. Recall also that the number of constituents in the jet is also larger (on average) for the gluon jet simply because a gluon will radiate more than a quark. These features explain much of what we observed earlier in terms of the effectiveness of the various observable to separate quark jets from gluon jets. Note in particular that the enhanced role of the shoulder for gluon jet explains, at least qualitatively, the difference in the distributions for the observable  $\Gamma_{Qjet}$ . Since the shoulder is dominated by a single large angle, hard emission, it is minimally impacted by pruning, which removes the large angle, *soft* constituents (as illustrated just below). Thus jets in the shoulder exhibit small volatility and they are a larger component in the gluon jet distribution. Hence gluon jets, on average, have smaller values of  $\Gamma_{Qjet}$  than quark jets as in Figure 1(b). Further this feature of gluon jets is distinct

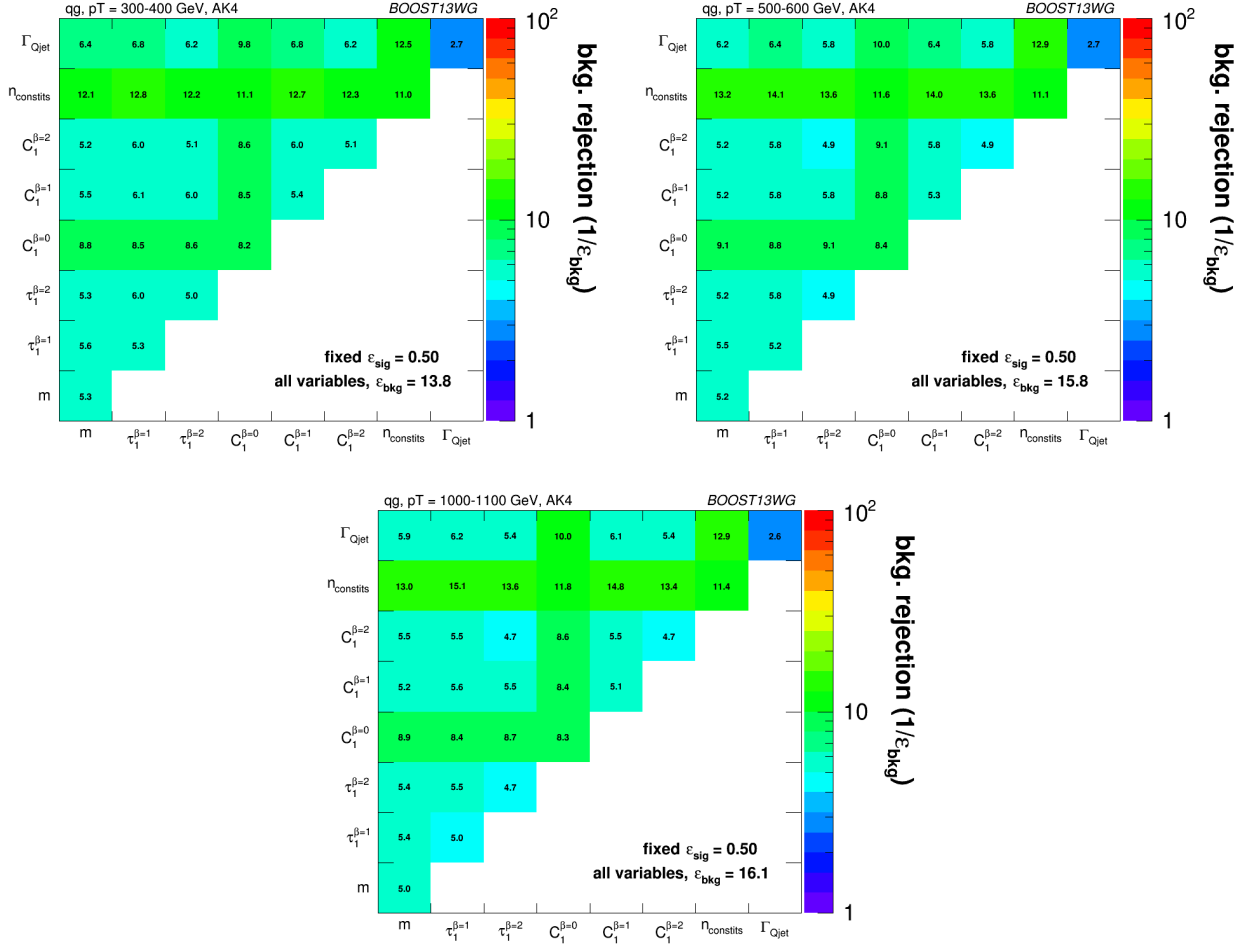


**Fig. 7** Gluon rejection defined as  $1/\epsilon_{\text{gluon}}$  when using each 2-variable combination as a tagger with 50% acceptance for quark jets. Results are shown for  $R=0.4$  jets with (top left)  $p_T = 300 - 400$  GeV, (top right)  $p_T = 500 - 600$  GeV and (bottom)  $p_T = 1 - 1.1$  TeV. The rejection obtained with a tagger that uses all variables is also shown in the plots.



**Fig. 8** Comparisons of quark and gluon ungroomed mass distributions versus the scaled variable  $m/p_T/R$ .



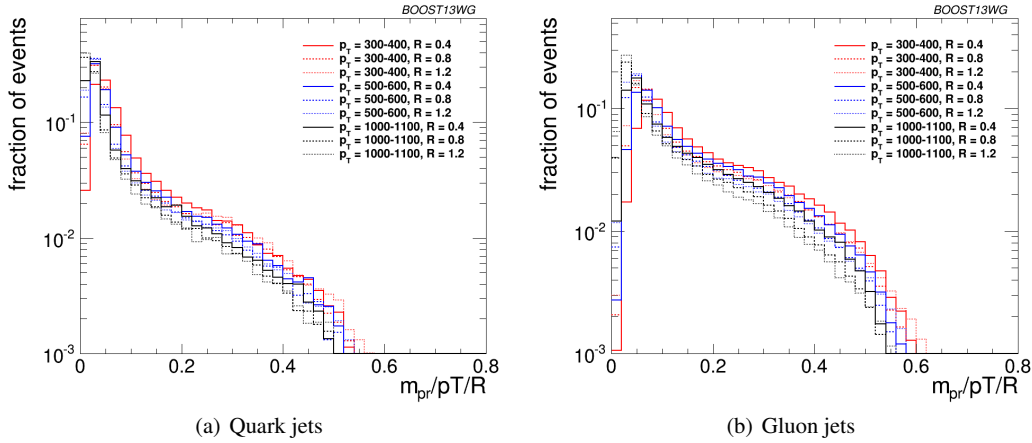


**Fig. 9** Comparisons of quark and gluon pruned mass distributions versus the scaled variable  $m_{\text{pr}}/p_T/R$ .

from fact that there are more constituents, which explains why  $\Gamma_{Qjet}$  and  $N_{\text{constits}}$  supply largely independent information for distinguishing quark and gluon jets.

To illustrate some of these points in more detail, Figure 9 exhibits the jet mass distributions (of Figure 8) after pruning [34, 48]. Removing the large angle, soft constituents moves the peak in both of the distributions from  $m/p_T/R \sim 0.1 - 0.2$  to the region around  $m/p_T/R \sim 0.05$ . This explains why pruning works to reduce the QCD background when looking for a signal in a specific jet mass bin. The “shoulder” feature is much more apparent after pruning, as is the larger shoulder for the gluon jets.

Our final topic is the residual  $R$  and  $p_T$  dependence exhibited in Figures 8 and 9, where we are using the scaled variable  $m/p_T/R$ . As already suggested, the residual  $p_T$  dependence can be understood as arising primarily from the slow decrease of the strong coupling  $\alpha_s(p_T)$  as  $p_T$  increases. This will lead to a corresponding decrease in the (largely perturbative) shoulder regime for both distributions as  $p_T$  increases. At the same time, and for the same reason, the Sudakov damping is less strong with increasing  $p_T$  and the peak moves towards the origin. Thus the overall impact of increasing  $p_T$  for both distributions is a (slow) shift to smaller values of  $m/p_T/R$ . This is just what is observed in Figures 8 and 9, although the numerical size of the effect is reduced in the pruned case. The  $R$  dependence is more complicated as there are effectively three different contributions to the mass distribution. The perturbative large angle, energetic single emission contribution largely scales in the variable  $m/p_T/R$ , which is why we see little residual  $R$  dependence in either figure for  $m/p_T/R > 0.4$ . The large angle soft emissions can both contribute at mass values that scale like  $R$  and increase in number as  $R$  increases (*i.e.*, as the area of the jet grows as  $R^2$ ). Such contributions can yield a distribution that moves to the right as  $R$  increases and presumably explain the behavior at small  $p_T$  in Figure 8. Since pruning largely removes this

contribution, we observe no such behavior in Figure 9. The contribution of small angle, soft emissions will be at fixed  $m$  values and thus shift to the left versus the scaled variable as  $R$  increases. This presumably explains the small shifts in this direction observed in both figures.

## 5.5 Conclusions

In Section 5 we have seen that a variety of jet observables provide information about the jet that can be employed effectively to separately tag quark and gluon jets. Further, when used in combination, these observables can provide even better separation. We saw that the best performing single observable is simply the number of constituents in the jet,  $N_{\text{constits}}$ , while the largest further improvement comes from combining with  $C_1^{\beta=1}$  (or  $\tau_1^{\beta=1}$ ), but the smallest  $R$  and  $p_T$  dependence arises from combining with  $C_1^{\beta=0}$ . On the other hand, some of the commonly used observables are highly correlated and do not provide extra information and enhanced tagging when used together. We have both demonstrated these correlations and provided a discussion of the physics behind the structure of the correlation. In particular, using the jet mass as a specific example observable we have tried to explicitly explain the differences between jets initiated by both quarks and gluons.

## 6 Boosted W-Tagging

In this section, we study the discrimination of a boosted hadronically decaying  $W$  signal against a gluon background, comparing the performance of various groomed jet masses, substructure variables, and BDT combinations of groomed mass and substructure. A range of different distance parameters  $R$  for the anti- $k_T$  jet algorithm are explored, as well as a variety of kinematic regimes (lead jet  $p_T$  300-400 GeV,

500-600 GeV, 1.0-1.1 TeV). This allows us to determine the performance of observables as a function of jet radius and jet boost, and to see where different approaches may break down. The groomed mass and substructure variables are then combined in a BDT as described in Section 4, and the performance of the resulting BDT discriminant explored through ROC curves to understand the degree to which variables are correlated, and how this changes with jet boost and jet radius.

## 6.1 Methodology

These studies use the  $WW$  samples as signal and the  $dijet\ gg$  as background, described previously in Section 2. Whilst only gluonic backgrounds are explored here, the conclusions as to the dependence of the performance and correlations on the jet boost and radius are not expected to be substantially different for quark backgrounds; we will see that the differences in the substructure properties of quark- and gluon-initiated jets, explored in the last section, are significantly smaller than the differences between  $W$ -initiated and gluon-initiated jets.

As in the  $q/g$  tagging studies, the showered events were clustered with FASTJET 3.03 using the anti- $k_T$  algorithm with jet radii of  $R = 0.4, 0.8, 1.2$ . In both signal and background samples, an upper and lower cut on the leading jet  $p_T$  is applied after showering/clustering, to ensure similar  $p_T$  spectra for signal and background in each  $p_T$  bin. The bins in leading jet  $p_T$  that are considered are 300-400 GeV, 500-600 GeV, 1.0-1.1 TeV, for the 300-400 GeV, 500-600 GeV, 1.0-1.1 TeV parton  $p_T$  slices respectively. The jets then have various grooming approaches applied and substructure observables reconstructed as described in Section 3.4. The substructure observables studied in this section are:

- The ungroomed, trimmed ( $m_{\text{trim}}$ ), and pruned ( $m_{\text{prun}}$ ) jet masses.
- The mass output from the modified mass drop tagger ( $m_{\text{mmdi}}$ ).
- The soft drop mass with  $\beta = -1, 2$  ( $m_{\text{sd}}$ ).
- 2-point energy correlation function ratio  $C_2^{\beta=1}$  (we also studied  $\beta = 2$  but do not show its results because it showed poor discrimination power).
- $N$ -subjettiness ratio  $\tau_2/\tau_1$  with  $\beta = 1$  ( $\tau_{21}^{\beta=1}$ ) and with axes computed using one-pass  $k_t$  axis optimization (we also studied  $\beta = 2$  but did not show its results because it showed poor discrimination power).
- The pruned Qjet mass volatility,  $\Gamma_{\text{Qjet}}$ .

## 6.2 Single Variable Performance

In this section we will explore the performance of the various groomed jet mass and substructure variables in terms

of discriminating signal and background. Since we have not attempted to optimise the grooming parameter settings of each grooming algorithm, we do not want to place too much emphasis here on the relative performance of the groomed masses, but instead concentrate on how their performance changes depending on the kinematic bin and jet radius considered.

Figure 10 compares the signal and background in terms of the different groomed masses explored for the anti- $k_T$   $R=0.8$  algorithm in the  $p_T$  500-600 bin. One can clearly see that in terms of separating signal and background the groomed masses will be significantly more performant than the ungroomed anti- $k_T$   $R=0.8$  mass. Figure 11 compares signal and background in the different substructure variables explored for the same jet radius and kinematic bin.

Figures 12, 13 and 14 show the single variable ROC curves compared to the ROC curve for a BDT combination of all the variables (labelled “allvars”), for each of the anti- $k_T$  distance parameters considered in each of the kinematic bins. One can see that, in all cases, the “allvars” option is considerably better performant than any of the individual single variables considered, indicating that there is considerable complementarity between the variables, and this will be explored further in the next section.

Although the ROC curves give all the relevant information, it is hard to compare performance quantitatively. In Figures 15, 16 and 17 are shown matrices which give the background rejection for a signal efficiency of 70% when two variables (that on the x-axis and that on the y-axis) are combined in a BDT. These are shown separately for each  $p_T$  bin and jet radius considered. In the final column of these plots are shown the background rejection performance for three-variable BDT combinations of  $m_{\text{sd}}^{\beta=2} + C_2^{\beta=1} + X$ . These results will be discussed later in Section 6.3.3. The diagonal of these plots correspond to the background rejections for a single variable BDT, and can thus be examined to get a quantitative measure of the individual single variable performance, and to study how this changes with jet radius and momenta.

One can see that in general the most performant single variables are the groomed masses. However, in certain kinematic bins and for certain jet radii,  $C_2^{\beta=1}$  has a background rejection that is comparable to or better than the groomed masses.

By comparing Figures 15(a), 16(a) and 17(b), we can see how the background rejection performance evolves as we increase momenta whilst keeping the jet radius fixed to  $R=0.8$ . Similarly, by comparing Figures 15(b), 16(b) and 17(c) we can see how performance evolves with  $p_T$  for  $R=1.2$ . For both  $R=0.8$  and  $R=1.2$  the background rejection power of the groomed masses increases with increasing  $p_T$ , with a factor 1.5-2.5 increase in rejection in going from the 300-400 GeV to 1.0-1.1 TeV bins. In Figure 18 we show the

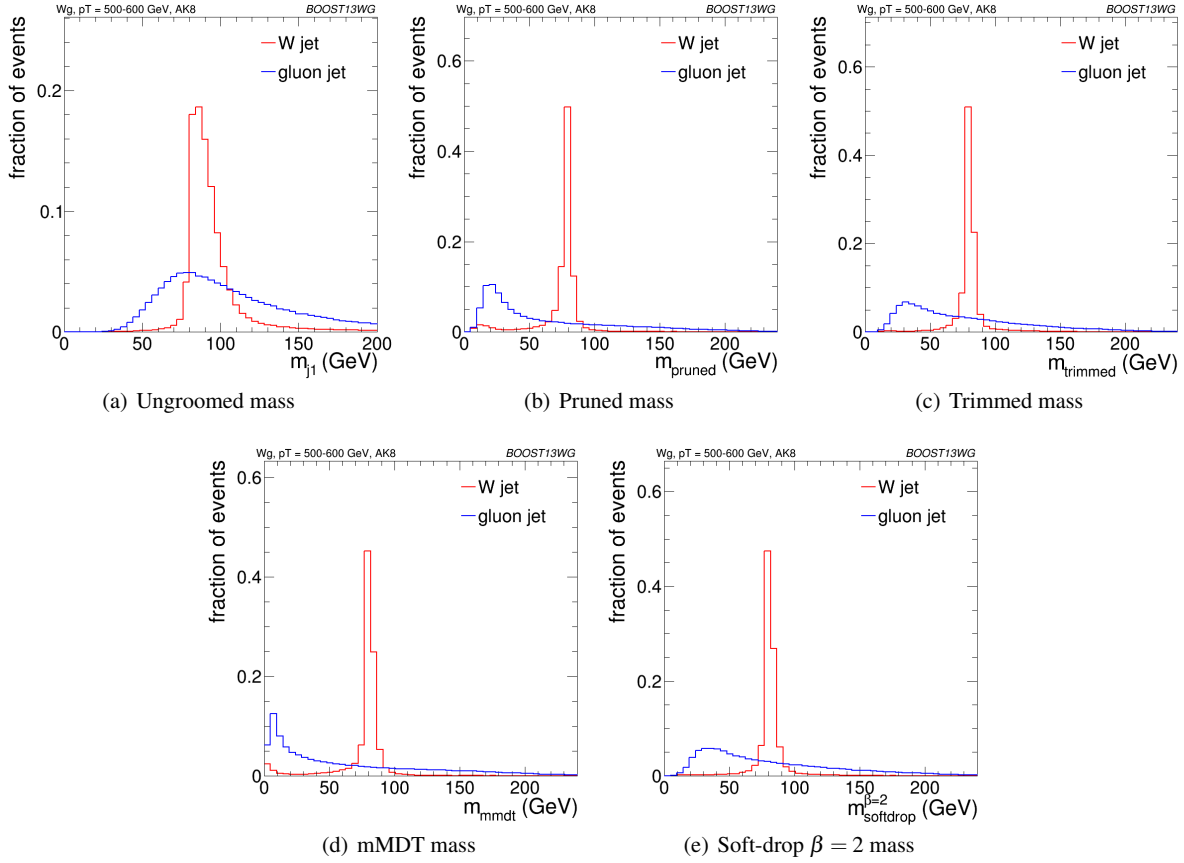


**Fig. 10** Comparisons of the QCD background to the WW signal in the  $p_T$  500-600 GeV bin using the anti- $k_T$   $R=0.8$  algorithm: leading jet mass distributions.

Soft-drop  $\beta = 2$  groomed mass and the pruned mass for signal and background in the  $p_T$  300-400 and  $p_T$  1.0-1.1 TeV bins for  $R=1.2$  jets. Two effects result in the improved performance of the groomed mass at high  $p_T$ . Firstly, as is evident from the figure, the resolution of the signal peak after grooming improves, because the groomer finds it easier to pick out the hard signal component of the jet against the softer components of the underlying event when the signal is boosted. Secondly, one can see from Figure 9 that as  $p_T$  increases the perturbative shoulder of the gluon distribution decreases in size, as discussed in Section 5.4, and thus there is a slight decrease (or at least no increase) in the level of background in the signal mass region ( $m/p_T/R \sim 0.5$ ).

However, one can see from the Figures 15(b), 16(b) and 17(c) that the  $C_2^{\beta=1}$ ,  $\Gamma_{Qjet}$  and  $\tau_{21}^{\beta=1}$  substructure variables behave somewhat differently. The background rejection power of the  $\Gamma_{Qjet}$  and  $\tau_{21}^{\beta=1}$  variables both decrease with increasing  $p_T$ , by up to a factor two in going from the 300-400 GeV to 1.0-1.1 TeV bins. Conversely the rejection power of  $C_2^{\beta=1}$  dramatically increases with increasing  $p_T$  for  $R=0.8$ , but does not improve with  $p_T$  for the larger jet radius  $R=1.2$ . In Figure 19 we show the  $\tau_{21}^{\beta=1}$  and  $C_2^{\beta=1}$  distributions for

signal and background in the  $p_T$  300-400 and  $p_T$  1.0-1.1 TeV bins for  $R=0.8$  jets. For  $\tau_{21}^{\beta=1}$  one can see that in moving from the lower to the higher  $p_T$  bin, the signal peak remains fairly unchanged, whereas the background peak shifts to smaller  $\tau_{21}^{\beta=1}$  values, reducing the discrimination power of the variable. This is expected, since jet substructure methods explicitly relying on identifying hard prongs would expect to work better at low  $p_T$ , where the prongs would tend to be more separated. However,  $C_2^{\beta=1}$  does not rely on the explicit identification of subjets, and one can see from Figure 19 that the discrimination power visibly increases with increasing  $p_T$ . This is in line with the observation in [42] that  $C_2^{\beta=1}$  performs best when  $m/p_T$  is small.

By comparing the individual sub-figures of Figures 15, 16 and 17 we can see how the background rejection performance depends on jet radius within the same  $p_T$  bin. To within  $\sim 25\%$ , the background rejection power of the groomed masses remains constant with respect to the jet radius. Figure 20 shows how the groomed mass changes for varying jet radius in the  $p_T$  1.0-1.1 TeV bin. One can see that the signal mass peak remains unaffected by the increased radius, as expected, since grooming removes the soft contam-

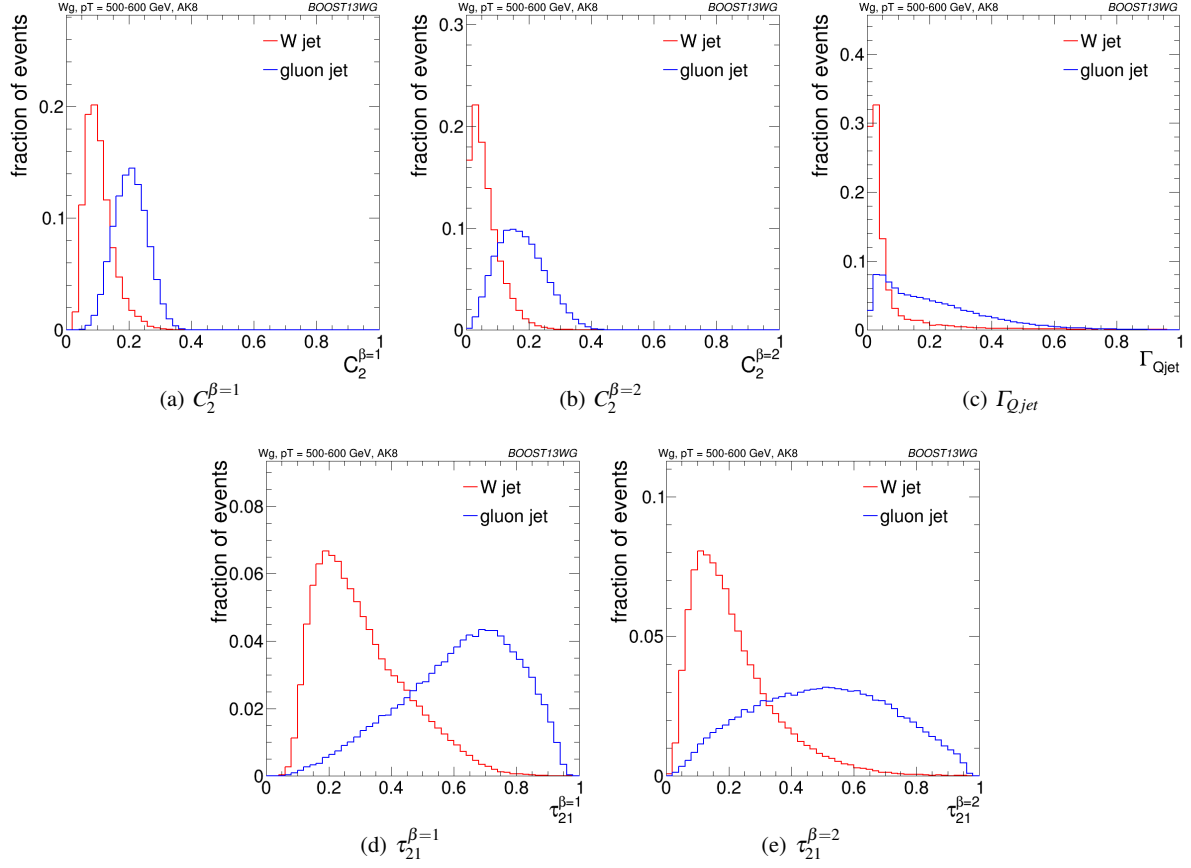


**Fig. 11** Comparisons of the QCD background to the WW signal in the  $p_T$  500-600 GeV bin using the anti- $k_T$  R=0.8 algorithm: substructure variables.

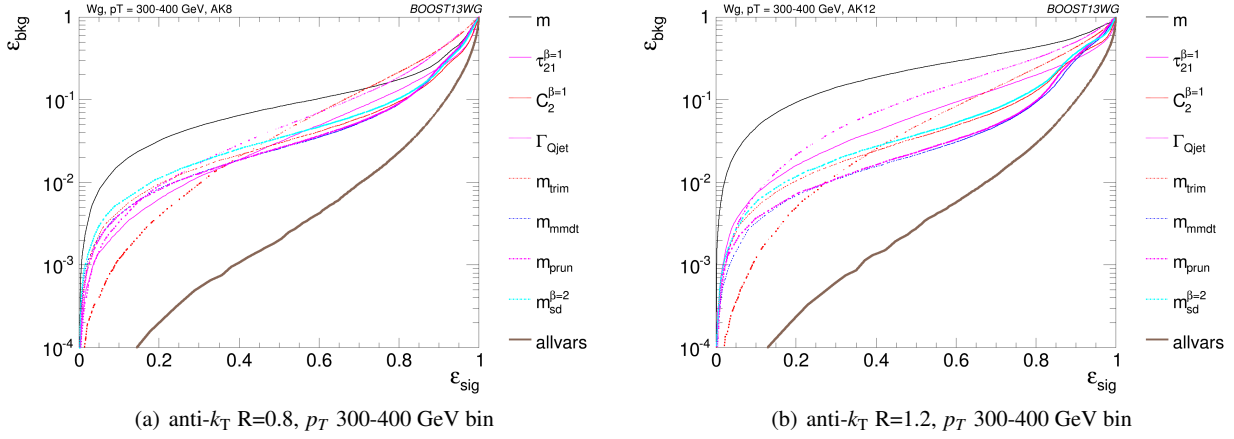


**Fig. 12** The ROC curve for all single variables considered for  $W$  tagging in the  $p_T$  300-400 GeV bin using the anti- $k_T$  R=0.8 algorithm and R=1.2 algorithm.

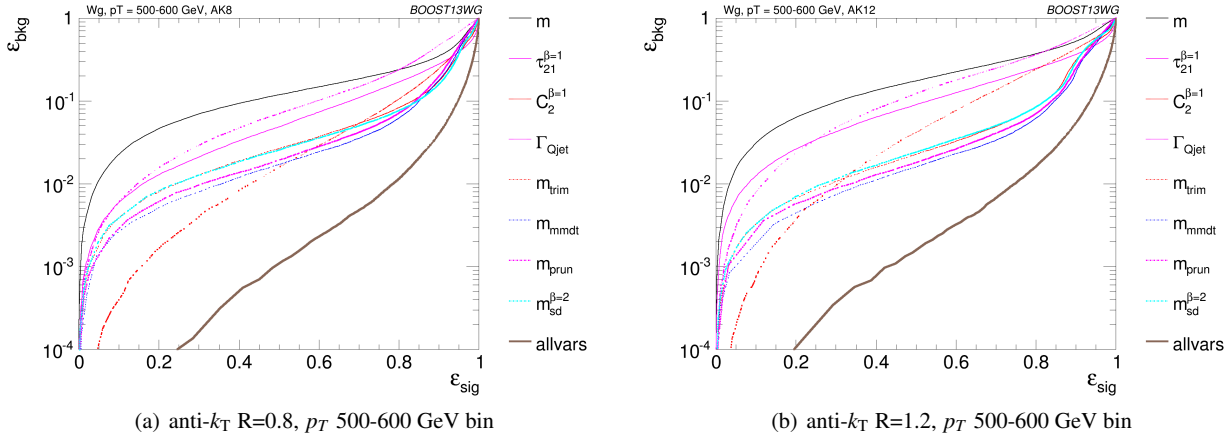


**Fig. 13** The ROC curve for all single variables considered for  $W$  tagging in the  $p_T$  500-600 GeV bin using the anti- $k_T$   $R=0.8$  algorithm and  $R=1.2$  algorithm.

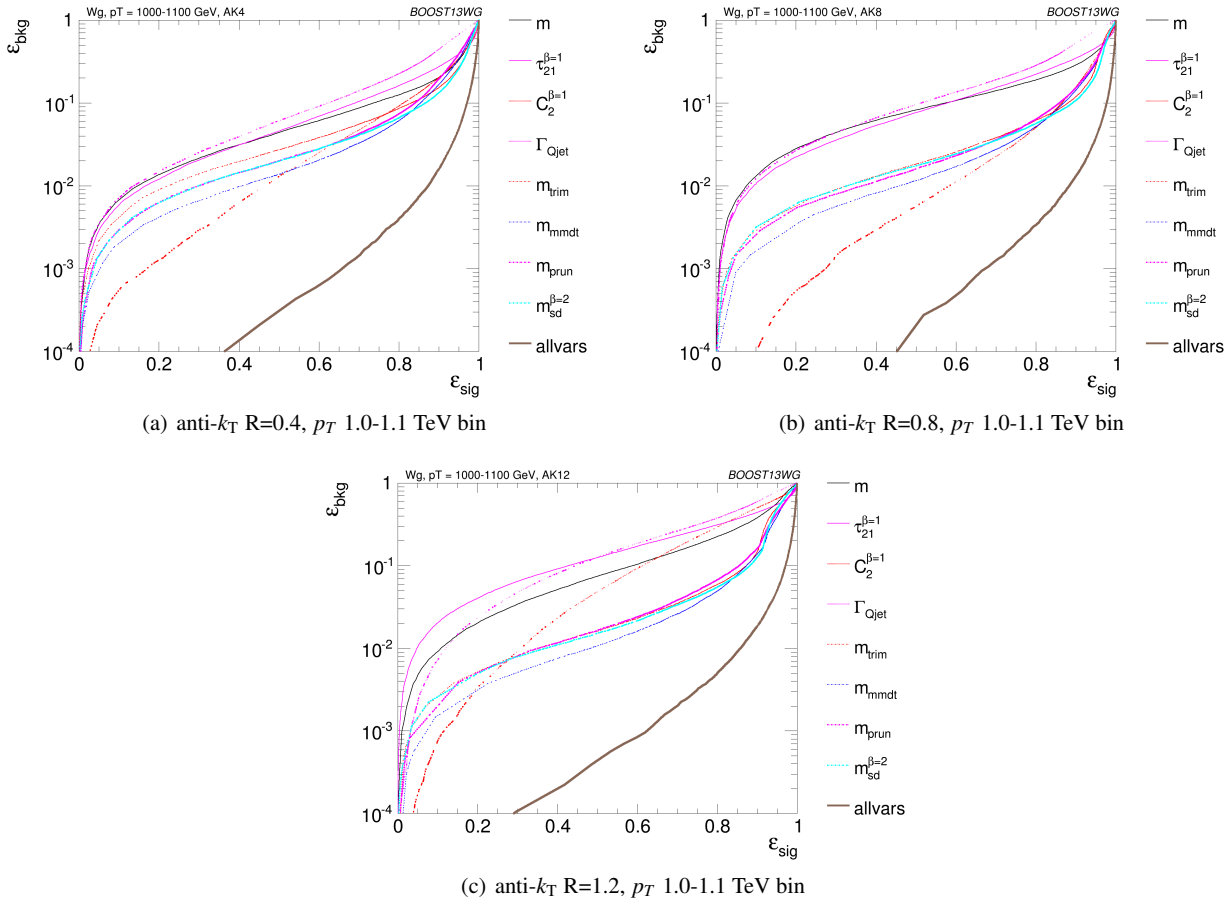


**Fig. 14** The ROC curve for all single variables considered for  $W$  tagging in the  $p_T$  1.0-1.1 TeV bin using the anti- $k_T$   $R=0.4$  algorithm, anti- $k_T$   $R=0.8$  algorithm and  $R=1.2$  algorithm.



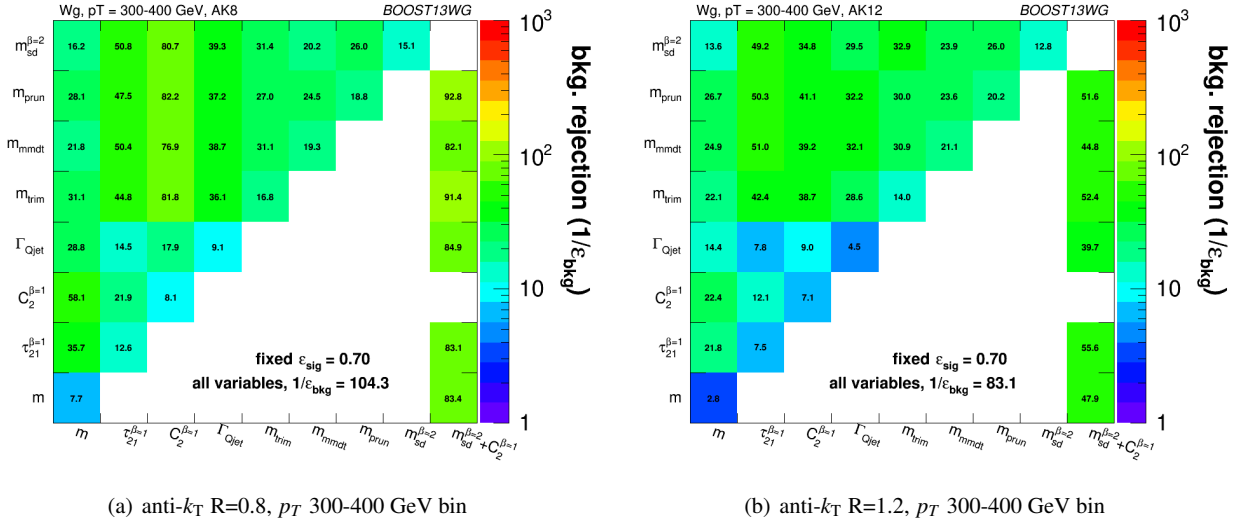


**Fig. 15** The background rejection for a fixed signal efficiency (70%) of each BDT combination of each pair of variables considered, in the  $p_T$  300-400 GeV bin using the anti- $k_T$   $R=0.8$  algorithm and  $R=1.2$  algorithm. Also shown is the background rejection for a BDT combination of all of the variables considered.

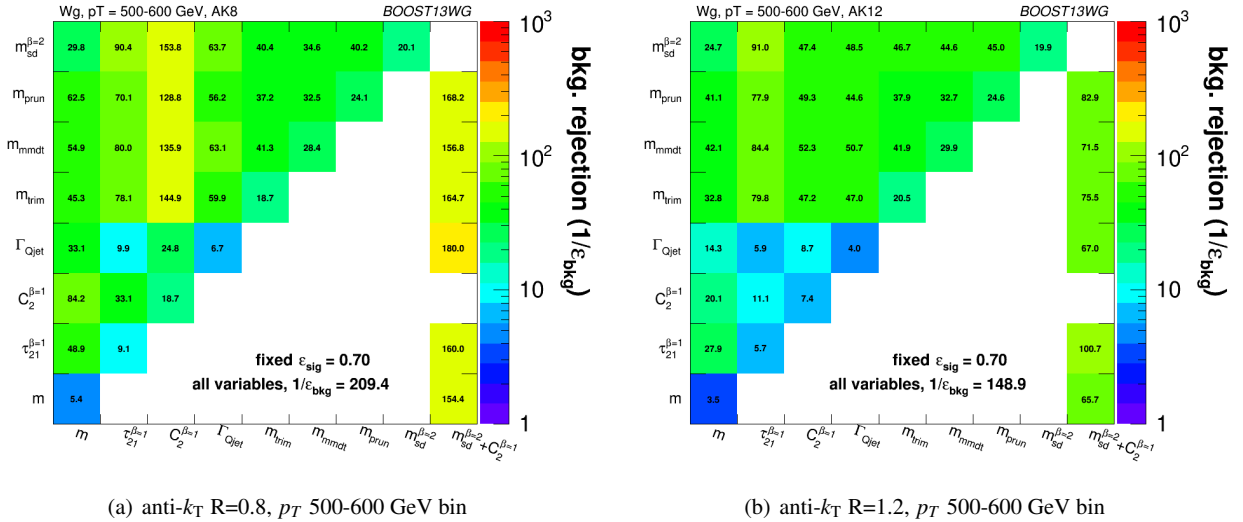


**Fig. 16** The background rejection for a fixed signal efficiency (70%) of each BDT combination of each pair of variables considered, in the  $p_T$  500-600 GeV bin using the anti- $k_T$   $R=0.8$  algorithm and  $R=1.2$  algorithm. Also shown is the background rejection for a BDT combination of all of the variables considered.

ination which could otherwise increase the mass of the jet as the radius increased. The gluon background in the signal mass region also remains largely unaffected, as expected from Figure 9, which shows very little dependence of the groomed gluon mass distribution on  $R$  in the signal region ( $m/p_T/R \sim 0.5$ ). This is discussed further in Section 5.4.

However, we again see rather different behaviour versus  $R$  for the substructure variables. In all  $p_T$  bins considered the most performant substructure variable,  $C_2^{\beta=1}$ , performs best for an anti- $k_T$  distance parameter of  $R=0.8$ . The performance of this variable is dramatically worse for the larger jet radius of  $R=1.2$  (a factor seven worse background rejection in the

1.0-1.1 TeV bin), and substantially worse for  $R=0.4$ . For the other jet substructure variables considered,  $\Gamma_{Qjet}$  and  $\tau_{21}^{\beta=1}$ , their background rejection power also reduces for larger jet radius, but not to the same extent. Figure 21 shows the  $\tau_{21}^{\beta=1}$  and  $C_2^{\beta=1}$  distributions for signal and background in the 1.0-1.1 TeV  $p_T$  bin for  $R=0.8$  and  $R=1.2$  jet radii. One can clearly see that for the larger jet radius the  $C_2^{\beta=1}$  distribution of both signal and background get wider, and consequently the discrimination power decreases. For  $\tau_{21}^{\beta=1}$  there is comparatively little change in the distributions with increasing jet radius. The increased sensitivity of  $C_2$  to soft

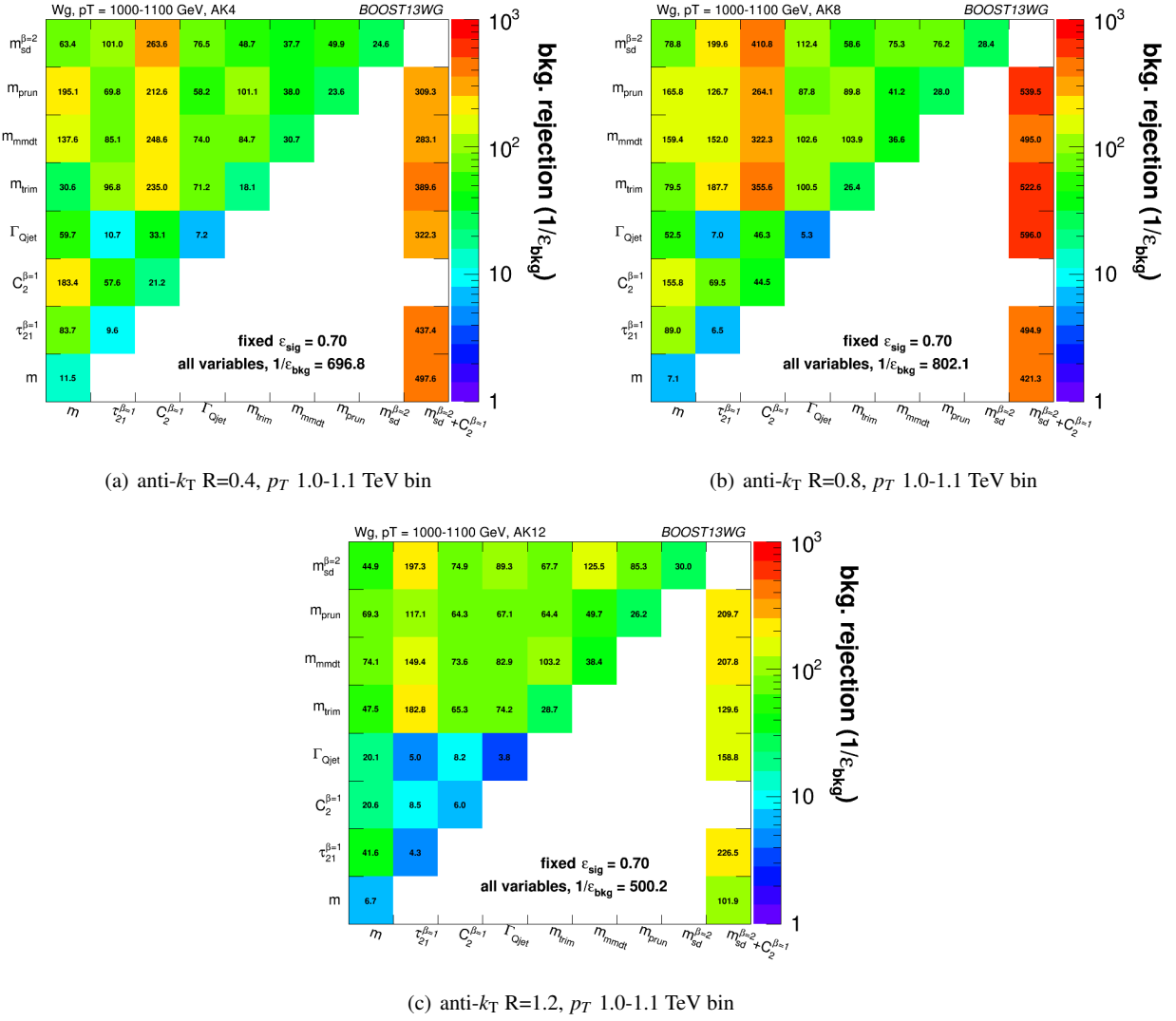


**Fig. 17** The background rejection for a fixed signal efficiency (70%) of each BDT combination of each pair of variables considered, in the  $p_T$  1.0-1.1 TeV bin using the anti- $k_T$   $R=0.4$ ,  $R=0.8$  and  $R=1.2$  algorithm. Also shown is the background rejection for a BDT combination of all of the variables considered.

wide angle radiation in comparison to  $\tau_{21}$  is a known feature of this variable [42], and a useful feature in discriminating coloured versus colour singlet jets. However, at very large jet radii ( $R \sim 1.2$ ), this feature becomes disadvantageous; the jet can pick up a significant amount of initial state or other uncorrelated radiation, and  $C_2$  is more sensitive to this than  $\tau_{21}$ . This uncorrelated radiation has no (or very little) dependence on whether the jet is W- or gluon-initiated, and so sensitivity to this radiation means that the discrimination power will decrease.

### 6.3 Combined Performance

The off-diagonal entries in Figures 15, 16 and 17 can be used to compare the performance of different BDT two-variable

combinations, and see how this varies as a function of  $p_T$  and  $R$ . By comparing the background rejection achieved for the two-variable combinations to the background rejection of the “all variables” BDT, one can understand how much more discrimination is possible by adding further variables to the two-variable BDTs.

One can see that in general the most powerful two-variable combinations involve a groomed mass and a non-mass substructure variable ( $C_2^{\beta=1}$ ,  $\Gamma_{Qjet}$  or  $\tau_{21}^{\beta=1}$ ). Two-variable combinations of the substructure variables are not powerful in comparison. Which particular mass + substructure variable combination is the most powerful depends strongly on the  $p_T$  and  $R$  of the jet, as discussed in the sections that follow.

There is also modest improvement in the background rejection when different groomed masses are combined, compared to the single variable groomed mass performance, in-

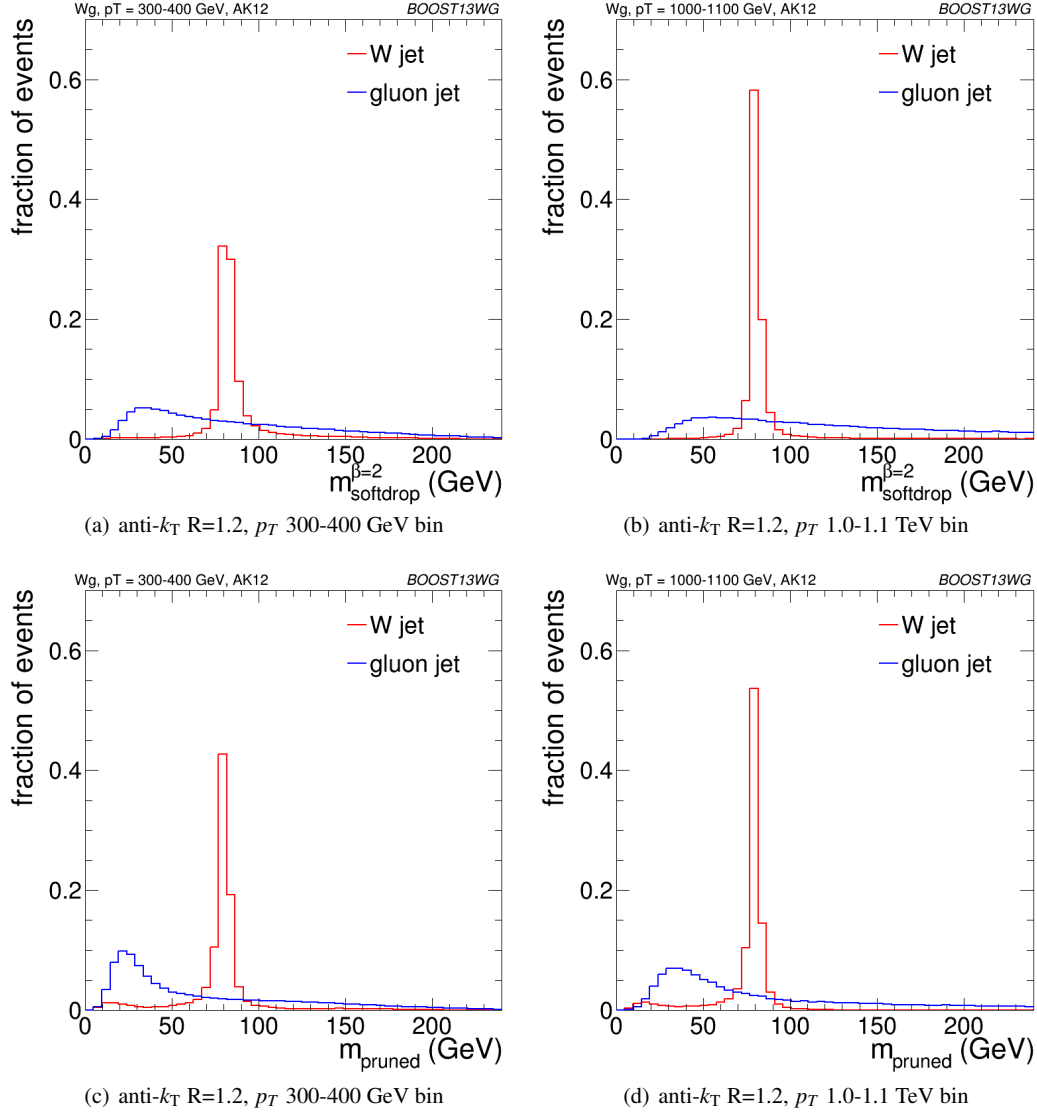


**Fig. 18** The Soft-drop  $\beta = 2$  and pruned groomed mass distribution for signal and background  $R=1.2$  jets in two different  $p_T$  bins.

dicating that there is complementary information between the different groomed masses. In addition, there is an improvement in the background rejection when the groomed masses are combined with the ungroomed mass, indicating that grooming removes some useful discriminatory information from the jet. These observations are explored further in the section below.

Generally one can see that the  $R=0.8$  jets offer the best two-variable combined performance in all  $p_T$  bins explored here. This is despite the fact that in the highest 1.0-1.1 GeV  $p_T$  bin the average separation of the quarks from the  $W$  decay is much smaller than 0.8, and well within 0.4. This conclusion could of course be susceptible to pile-up, which is not considered in this study.

### 6.3.1 Mass + Substructure Performance

As already noted, the largest background rejection at 70% signal efficiency are in general achieved using those two variable BDT combinations which involve a groomed mass and a non-mass substructure variable. For both  $R=0.8$  and  $R=1.2$  jets, the rejection power of these two variable combinations increases substantially with increasing  $p_T$ , at least within the  $p_T$  range considered here.

For a jet radius of  $R=0.8$ , across the full  $p_T$  range considered, the groomed mass + substructure variable combinations with the largest background rejection are those which involve  $C_2^{\beta=1}$ . For example, in combination with  $m_{sd}^{\beta=2}$ , this produces a five-, eight- and fifteen-fold increase in background rejection compared to using the groomed mass alone. In Figure 22 the low degree of correlation between  $m_{sd}^{\beta=2}$

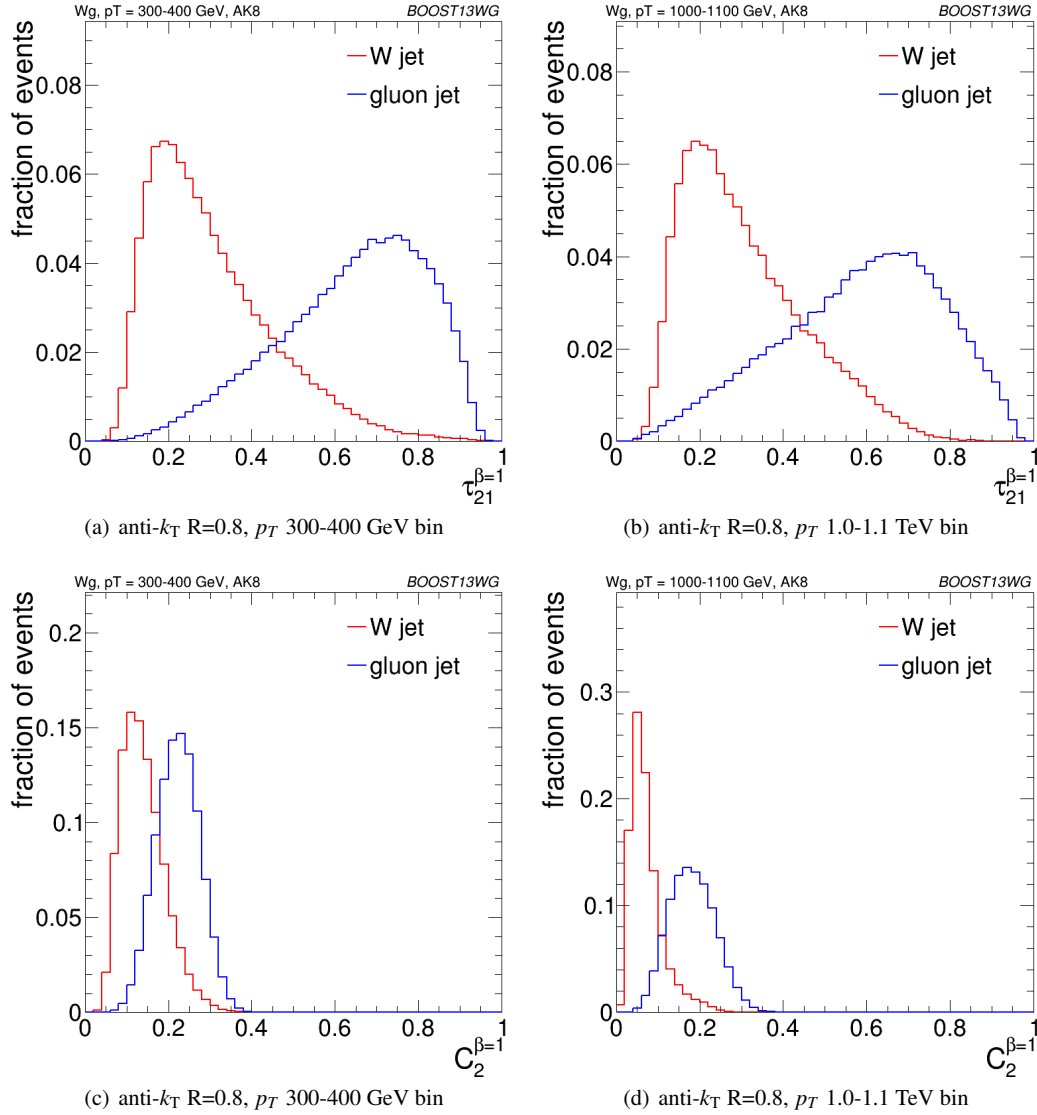


**Fig. 19** The  $\tau_{21}^{\beta=1}$  and  $C_2^{\beta=1}$  distributions for signal and background  $R=0.8$  jets in two different  $p_T$  bins.

versus  $C_2^{\beta=1}$  that leads to these large improvements in background rejection can be seen. One can also see that what little correlation exists is rather non-linear in nature, changing from a negative to a positive correlation as a function of the groomed mass, something which helps to improve the background rejection in the region of the W mass peak.

However, when we switch to a jet radius of  $R=1.2$  the picture for  $C_2^{\beta=1}$  combinations changes dramatically. These become significantly less powerful, and the most powerful variable in groomed mass combinations becomes  $\tau_{21}^{\beta=1}$  for all jet  $p_T$  considered. Figure 23 shows the correlation between  $m_{sd}^{\beta=2}$  and  $C_2^{\beta=1}$  in the  $p_T$  1.0 - 1.2 TeV bin for the various jet radii considered. Figure 24 is the equivalent set of distributions for  $m_{sd}^{\beta=2}$  and  $\tau_{21}^{\beta=1}$ . One can see from Figure 23 that, due to the sensitivity of the observable to soft, wide-angle radiation, as the jet radius increases  $C_2^{\beta=1}$  increases and becomes more and more smeared out for both signal and background, leading to worse discrimination power. This does not happen to the same extent for  $\tau_{21}^{\beta=1}$ . We can see from Figure 24 that the negative correlation between  $m_{sd}^{\beta=2}$  and  $\tau_{21}^{\beta=1}$  that is clearly visible for  $R=0.4$  decreases for larger jet radius, such that the groomed mass and substructure variable are far less correlated and  $\tau_{21}^{\beta=1}$  offers improved discrimination within a  $m_{sd}^{\beta=2}$  mass window.

6.3.2 Mass + Mass Performance

The different groomed masses and the ungroomed mass are of course not fully correlated, and thus one can always see some kind of improvement in the background rejection (rel-

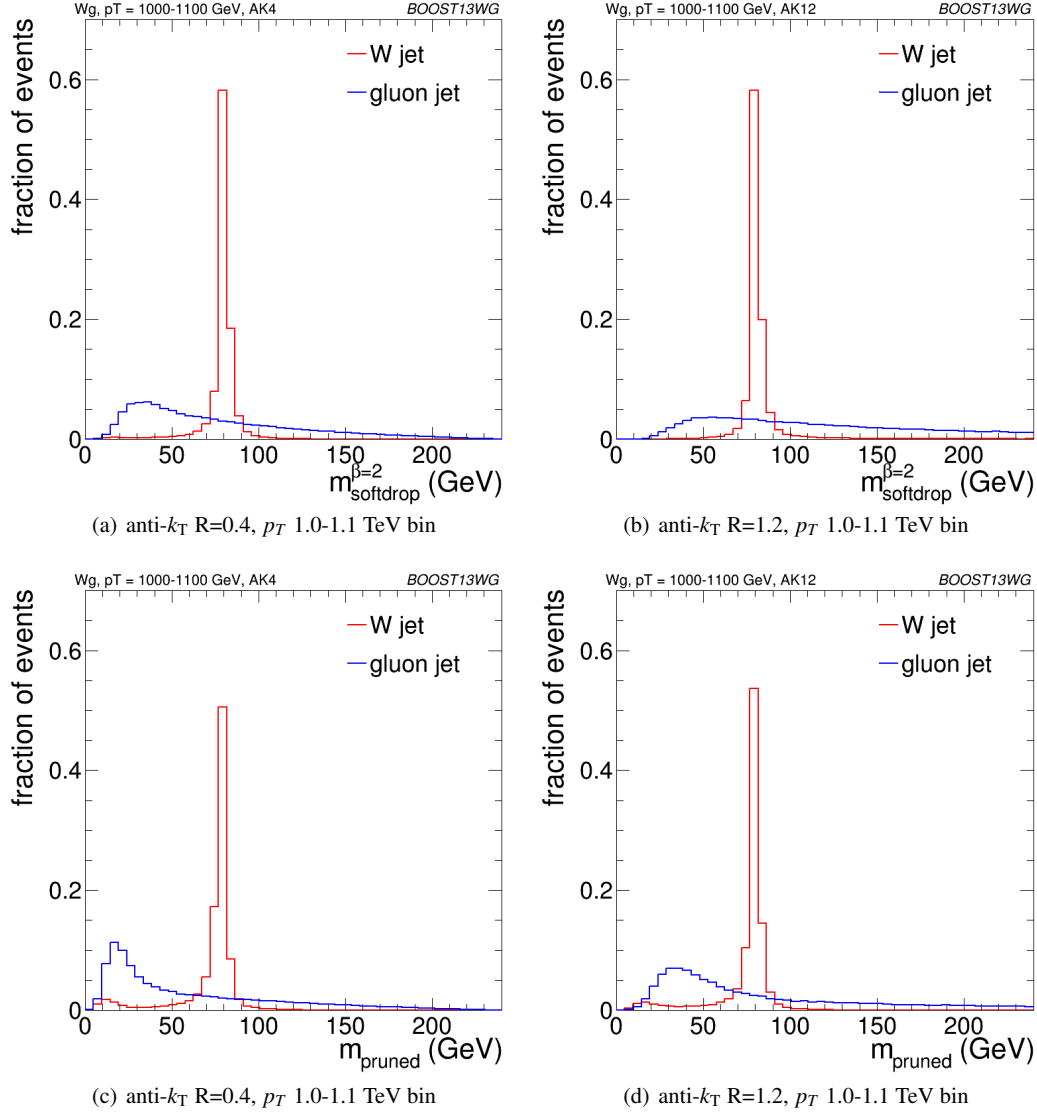


**Fig. 20** The Soft-drop  $\beta = 2$  and pruned groomed mass distribution for signal and background  $R=0.4$  and  $R=1.2$  jets in the 1.0-1.1 TeV  $p_T$  bin.

ative to the single mass performance) when two different mass variables are combined in the BDT. However, in some cases the improvement can be dramatic, particularly at high  $p_T$ , and particularly for combinations with the ungroomed mass. For example, in Figure 17 we can see that in the 1.0-1.1 TeV bin the combination of pruned mass with ungroomed mass produces a greater than eight-fold improvement in the background rejection for  $R=0.4$  jets, a greater than five-fold improvement for  $R=0.8$  jets, and a factor  $\sim$ two improvement for  $R=1.2$  jets. A similar behaviour can be seen for mMDT mass. In Figures 25, 26 and 27 is shown the 2-D correlation plots of the pruned mass versus the ungroomed mass separately for the WW signal and  $gg$  background samples in the  $p_T$  1.0-1.1 TeV bin, for the various jet radii considered. For comparison, the correlation of the trimmed mass with the ungroomed mass, a combination that does not

improve on the single mass as dramatically, is shown. In all cases one can see that there is a much smaller degree of correlation between the pruned mass and the ungroomed mass in the background sample than for the trimmed mass and the ungroomed mass. This is most obvious in Figure 25, where the high degree of correlation between the trimmed and ungroomed mass is expected, since with the parameters used (in particular  $R_{\text{trim}} = 0.2$ ) we cannot expect trimming to have a significant impact on an  $R=0.4$  jet. The reduced correlation with ungroomed mass for pruning in the background means that, once we have made the requirement that the pruned mass is consistent with a W (i.e.  $\sim 80$  GeV), a relatively large difference between signal and background in the ungroomed mass still remains, and can be exploited to improve the background rejection further. In other words, many of the background events which pass the pruned mass



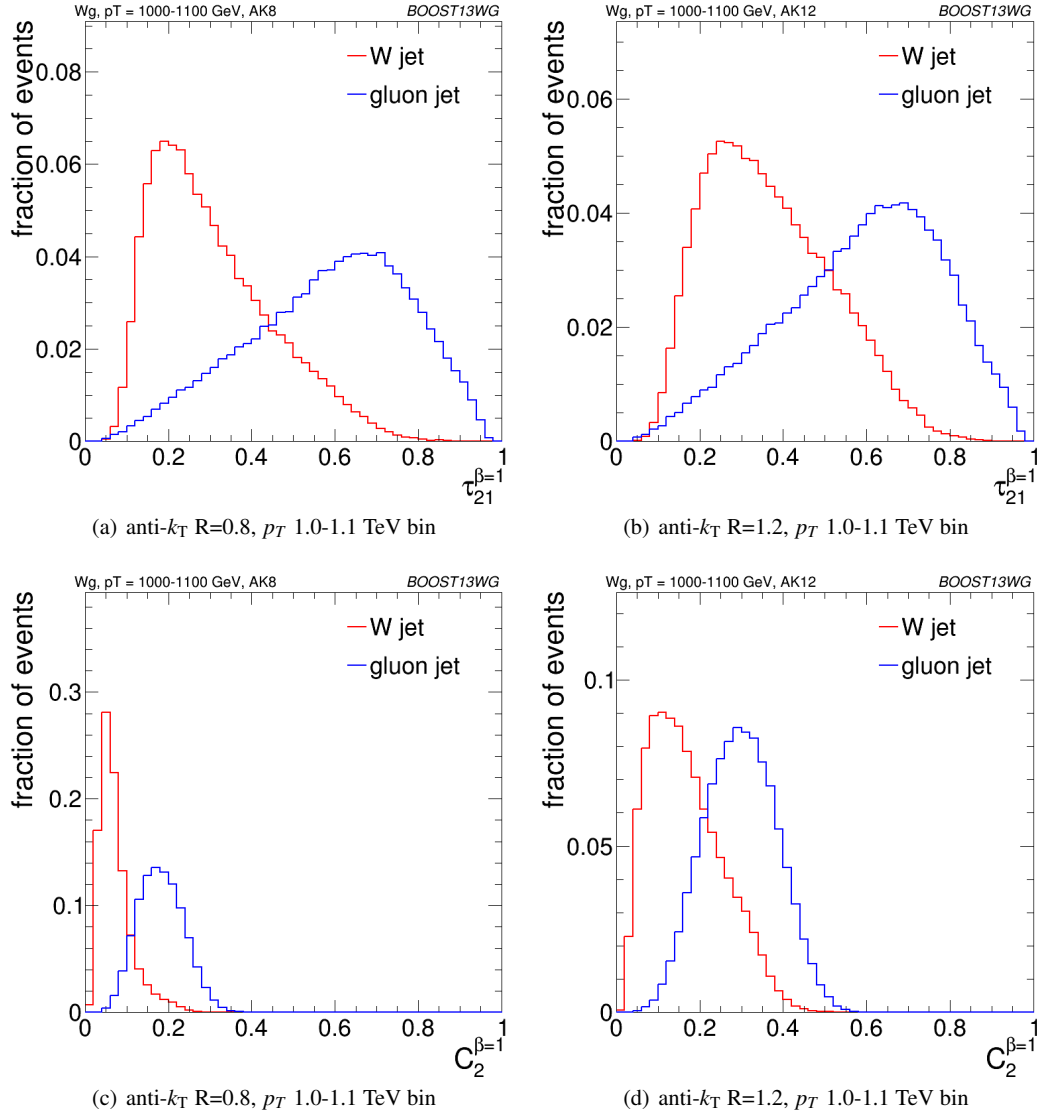


**Fig. 21** The  $\tau_{21}^{\beta=1}$  and  $C_2^{\beta=1}$  distributions for signal and background R=0.8 and R=1.2 jets in the 1.0-1.1 TeV  $p_T$  bin.

requirement do so because they are shifted to lower mass (to be within a signal mass window) by the grooming, but these events still have the property that they look very much like background events before the grooming. A single requirement on the groomed mass only does not exploit this. Of course, the impact of pile-up, not considered in this study could significantly limit the degree to which the ungroomed mass could be used to improve discrimination in this way.

### 6.3.3 “All Variables” Performance

As well as the background rejection at a fixed 70% signal efficiency for two-variable combinations, Figures 15, 16 and 17 also report the background rejection achieved by a combination of all the variables considered into a single BDT discriminant. One can see that, in all cases, the

rejection power of this “all variables” BDT is significantly larger than the best two-variable combination. This indicates that beyond the best two-variable combination there is still significant complementary information available in the remaining variables in order to improve the discrimination of signal and background. How much complementary information is available appears to be  $p_T$  dependent. In the lower  $p_T$  300-400 and 500-600 GeV bins the background rejection of the “all variables” combination is a factor  $\sim 1.5$  greater than the best two-variable combination, but in the highest  $p_T$  bin it is a factor  $\sim 2.5$  greater.

The final column in Figures 15, 16 and 17 allows us to explore the all variables performance a little further. It shows the background rejection for three variable BDT combinations of  $m_{sd}^{\beta=2} + C_2^{\beta=1} + X$ , where  $X$  is the variable on the y-axis. For jets with R=0.4 and R=0.8, the combination

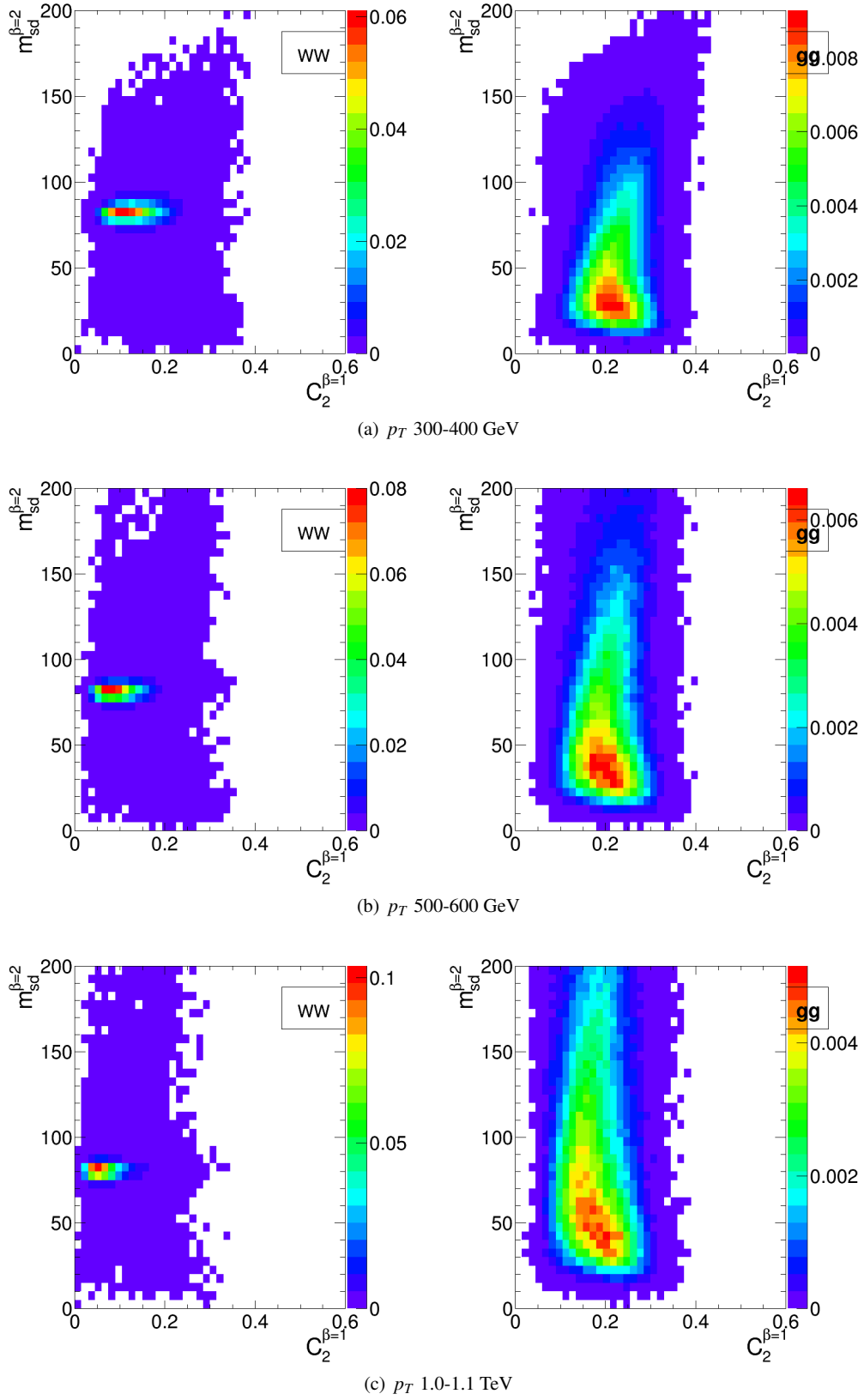


**Fig. 22** 2-D plots showing  $m_{sd}^{\beta=2}$  versus  $C_2^{\beta=1}$  for  $R=0.8$  jets in the various  $p_T$  bins considered.

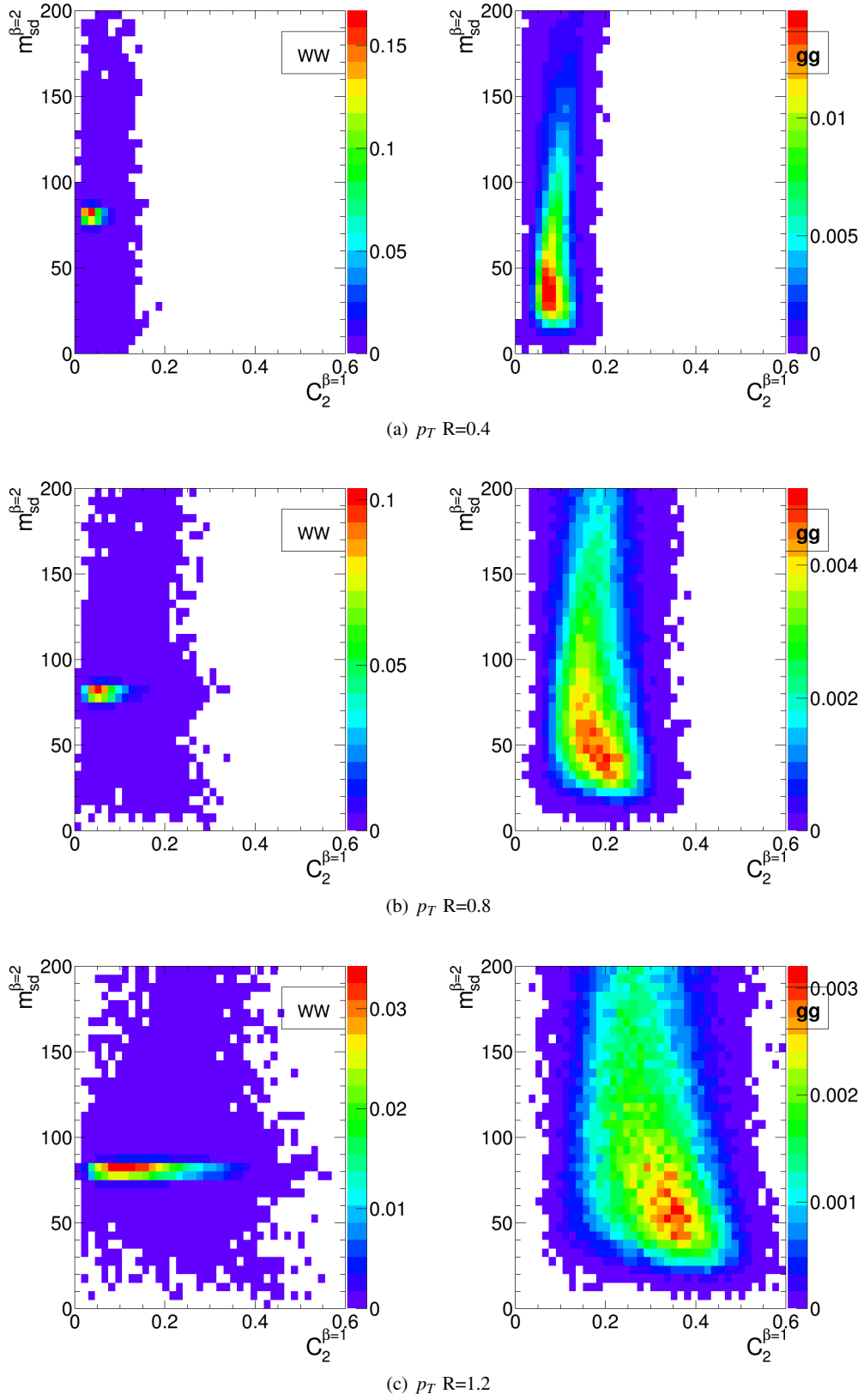


**Fig. 23** 2-D plots showing  $m_{sd}^{\beta=2}$  versus  $C_2^{\beta=1}$  for  $R=0.4, 0.8$  and  $1.2$  jets in the  $p_T$  1.0-1.1 TeV bin.

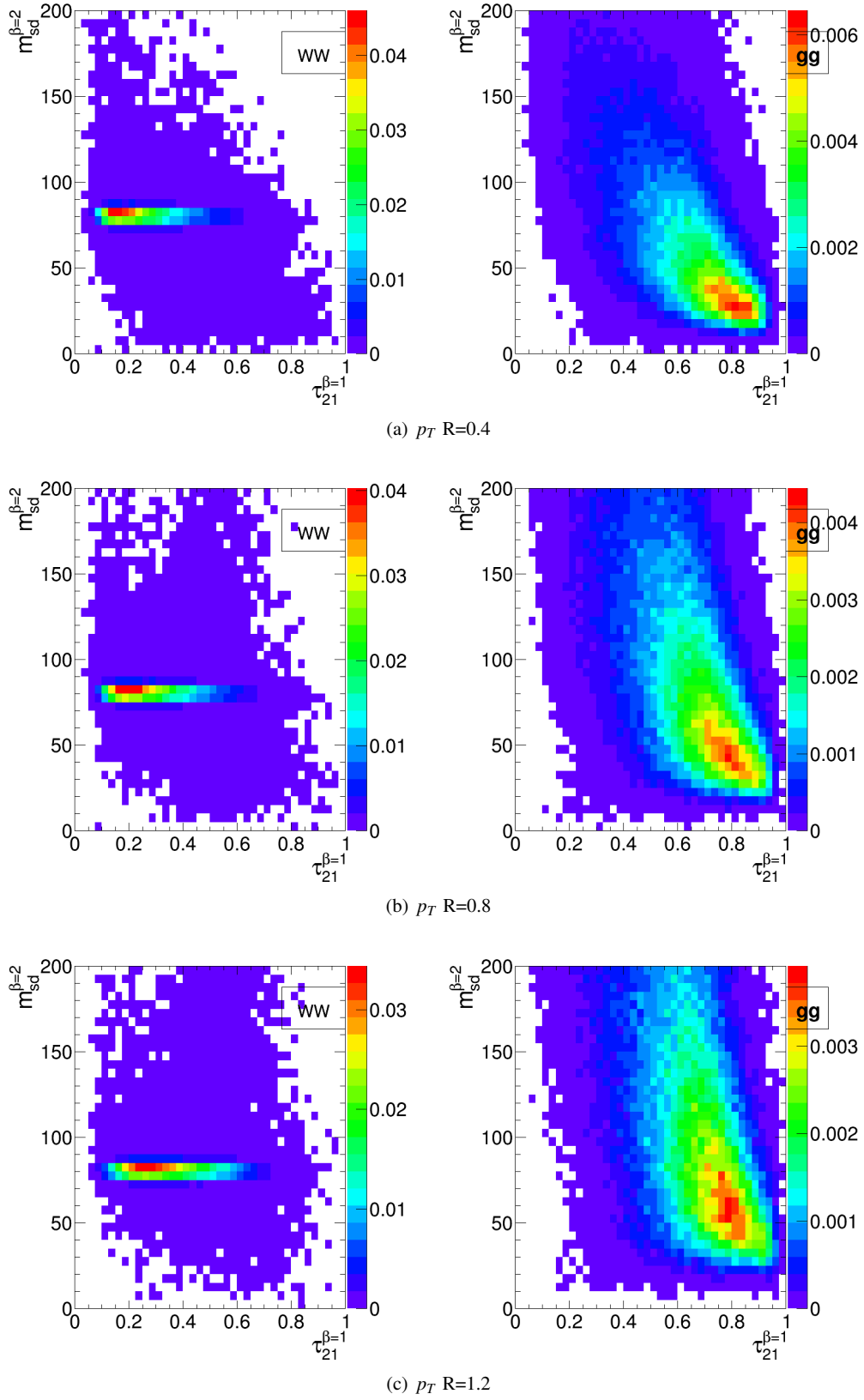


**Fig. 24** 2-D plots showing  $m_{sd}^{\beta=2}$  versus  $\tau_{21}^{\beta=1}$  for  $R=0.4, 0.8$  and  $1.2$  jets in the  $p_T$  1.0-1.1 TeV bin.

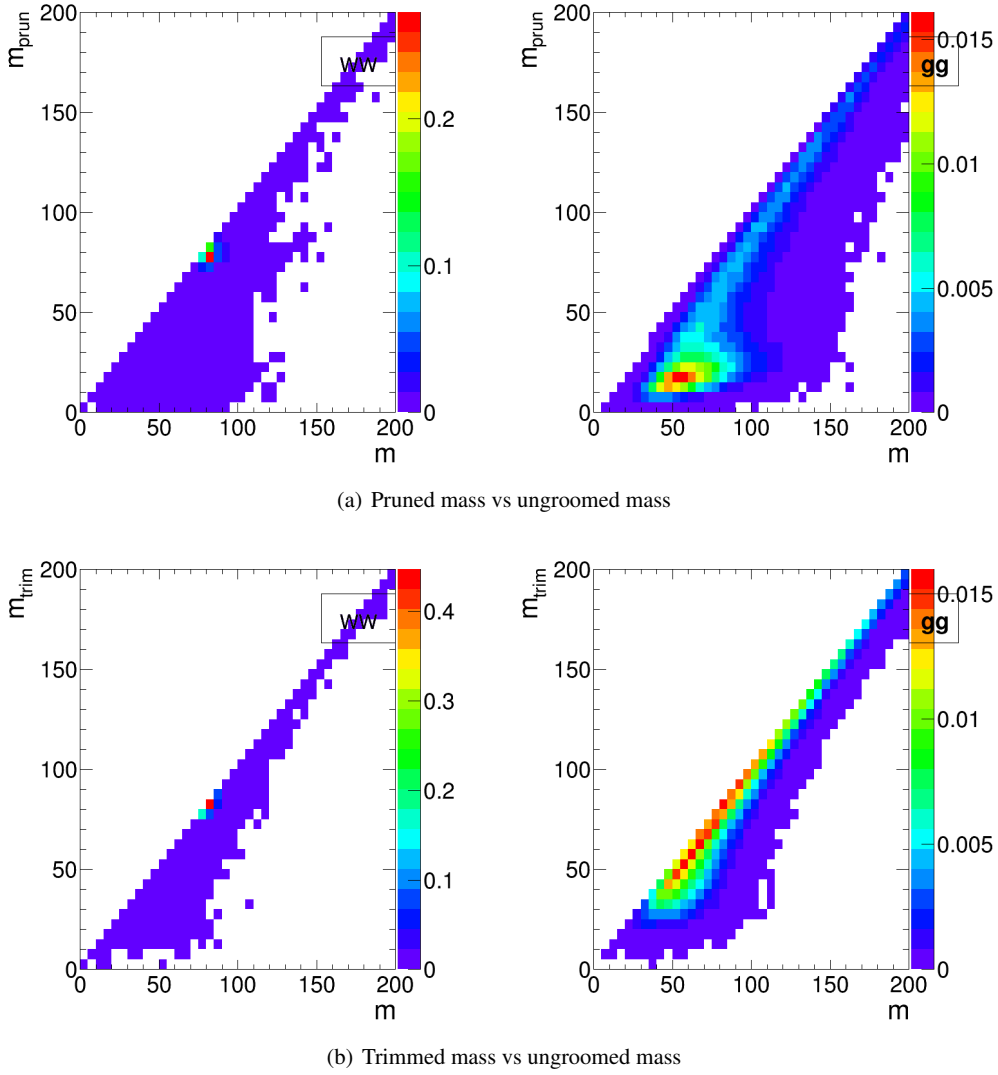


**Fig. 25** 2-D plots showing the correlation between groomed and ungroomed mass for  $WW$  and  $gg$  events in the  $p_T$  1.0-1.1 TeV bin using the anti- $k_T$   $R=0.4$  algorithm.

$m_{sd}^{\beta=2} + C_2^{\beta=1}$  is the best performant (or very close to the best performant) two-variable combination in every  $p_T$  bin considered. For  $R=1.2$  this is not the case, as  $C_2^{\beta=1}$  is superseded by  $\tau_{21}^{\beta=1}$  in performance, as discussed earlier. Thus, in considering the three-variable combination results it is best to focus on the  $R=0.4$  and  $R=0.8$  cases. Here we see that, for the lower  $p_T$  300-400 and 500-600 GeV bins, adding the third variable to the best two-variable combination brings us to within  $\sim 15\%$  of the “all variables” background rejection. However, in the highest  $p_T$  1.0-1.1 TeV bin, whilst adding the third variable does improve the performance considerably, we are still  $\sim 40\%$  from the observed “all variables” background rejection, and clearly adding a fourth or maybe even fifth variable would bring considerable gains. In terms of which variable offers the best improvement when added to the  $m_{sd}^{\beta=2} + C_2^{\beta=1}$  combination, it is hard to see an obvious

pattern; the best third variable changes depending on the  $p_T$  and  $R$  considered.

In conclusion, it appears that there is a rich and complex structure in terms of the degree to which the discriminatory information provided by the set of variables considered overlaps, with the degree of overlap apparently decreasing at higher  $p_T$ . This suggests that in all  $p_T$  ranges, but especially at higher  $p_T$ , there are substantial performance gains to be made by designing a more complex multivariate  $W$  tagger.

#### 6.4 Conclusions

We have studied the performance, in terms of the degree to which a hadronically decaying  $W$  boson can be separated from a gluonic background, of a number of groomed jet masses, substructure variables, and BDT combinations of



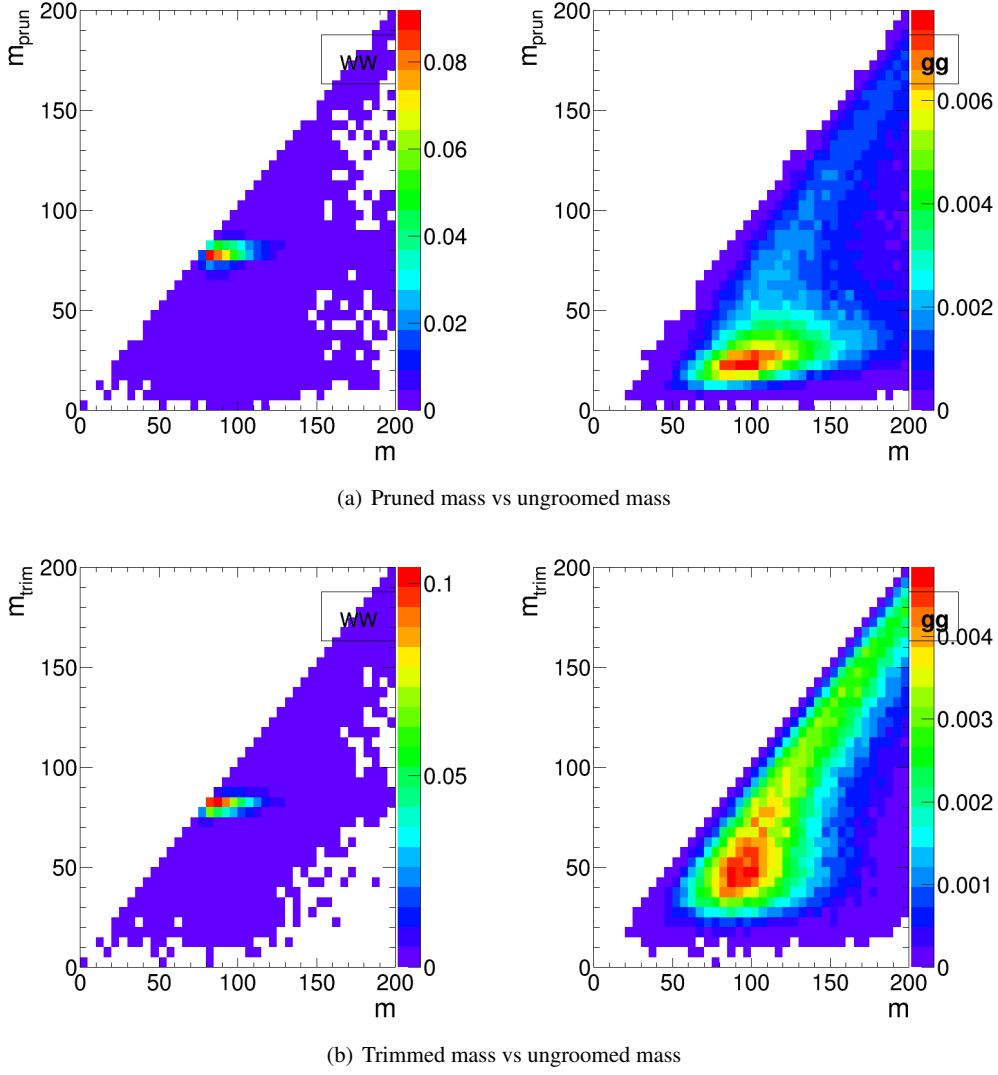


**Fig. 26** 2-D plots showing the correlation between groomed and ungroomed mass for  $WW$  and  $gg$  events in the  $p_T$  1.0-1.1 TeV bin using the anti- $k_T$   $R=0.8$  algorithm.

the above. We have used this to build a picture of how the discriminatory information contained in the variables overlaps, and how this complementarity between the variables changes with  $p_T$  and anti- $k_T$  distance parameter  $R$ .

In terms of the performance of individual variables, we find that, in agreement with other studies [49], in general the groomed masses perform best, with a background rejection power that increases with increasing  $p_T$ , but which is more constant with respect to changes in  $R$ . We have explained the dependence of the groomed mass performance on  $p_T$  and  $R$  using the understanding of the QCD mass distribution gleaned in Section 5.4. Conversely, the performance of other substructure variables, such as  $C_2^{\beta=1}$  and  $\tau_{21}^{\beta=1}$  is more susceptible to changes in radius, with background rejection power decreasing with increasing  $R$ . This is due to the in-

herent sensitivity of these observables to soft, wide angle radiation.

The best two-variable performance is obtained by combining a groomed mass with a substructure variable. Which particular substructure variable works best in combination is strongly dependent on  $p_T$  and  $R$ .  $C_2^{\beta=1}$  offers significant complementarity to groomed mass at smaller  $R$ , owing to the small degree of correlation between the variables. However, the sensitivity of  $C_2^{\beta=1}$  to soft, wide-angle radiation leads to worse discrimination power at large  $R$ , where  $\tau_{21}^{\beta=1}$  performs better in combination. Our studies also demonstrate the potential for enhanced discrimination by combining groomed and ungroomed mass information, although the use of ungroomed mass in this may in practice be limited by the presence of pile-up that is not considered in these studies.

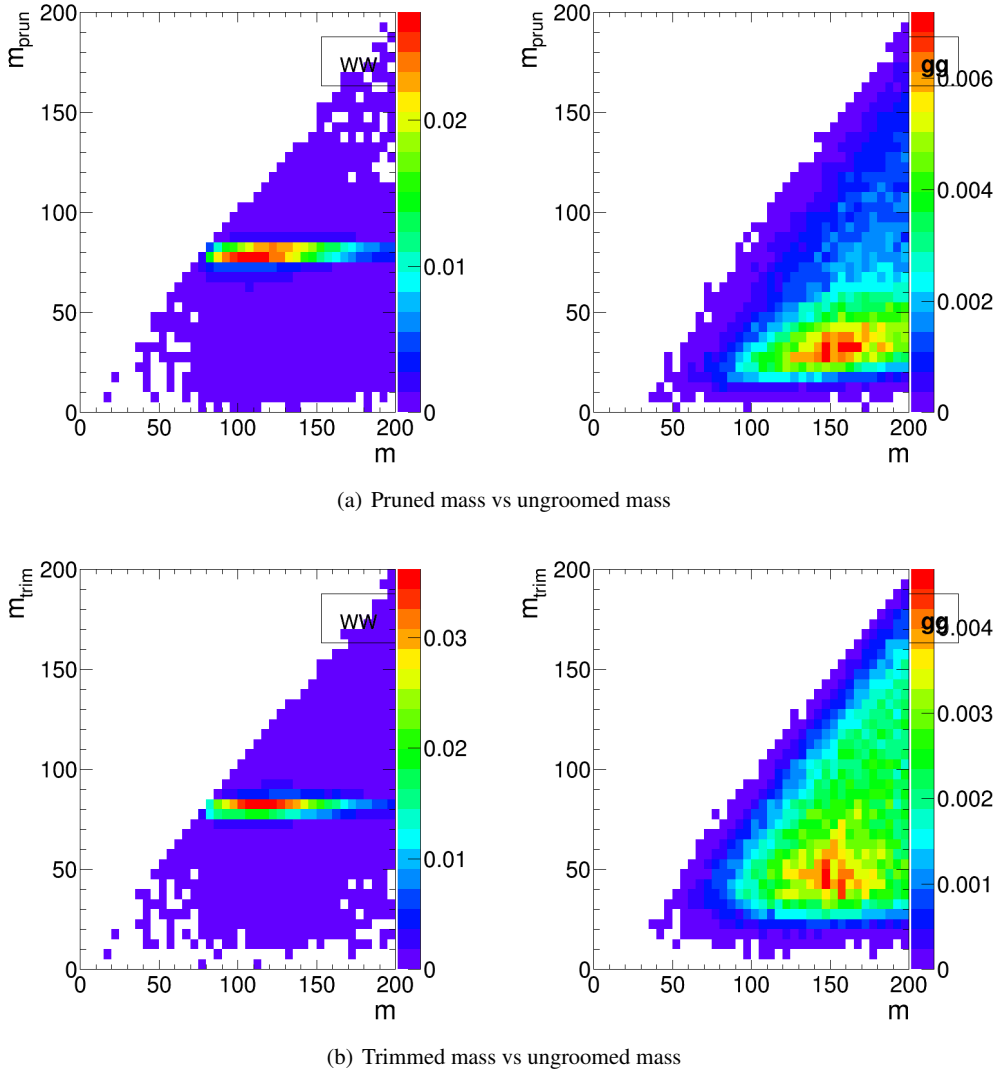


**Fig. 27** 2-D plots showing the correlation between groomed and ungroomed mass for  $WW$  and  $gg$  events in the  $p_T$  1.0-1.1 TeV bin using the anti- $k_T$   $R=1.2$  algorithm.

By examining the performance of a BDT combination of all the variables considered, it is clear that there are potentially substantial performance gains to be made by designing a more complex multivariate  $W$  tagger, especially at high  $p_T$ .

## 7 Top Tagging

In this section, we study the identification of boosted top quarks at Run II of the LHC. Boosted top quarks result in large-radius jets with complex substructure, containing a  $b$ -subjett and a boosted  $W$ . The additional kinematic handles coming from the reconstruction of the  $W$  mass and  $b$ -tagging allow a very high degree of discrimination of top quark jets from QCD backgrounds.

We consider top quarks with moderate boost (600-1000 GeV), and perhaps most interestingly, at high boost ( $\gtrsim 1500$  GeV). Top tagging faces several challenges in the high- $p_T$  regime. For such high- $p_T$  jets, the  $b$ -tagging efficiencies are no longer reliably known. Also, the top jet can also be accompanied by additional radiation with  $p_T \sim m_t$ , leading to combinatoric ambiguities of reconstructing the top and  $W$ , and the possibility that existing taggers or observables shape the background by looking for subjet combinations that reconstruct  $m_t/m_W$ . To study this, we examine the performance of both mass-reconstruction variables, as well as shape observables that probe the three-pronged nature of the top jet and the accompanying radiation pattern.

We use the top quark MC samples for each bin described in Section 2.2. The analysis relies on FASTJET 3.0.3 for jet clustering and calculation of jet substructure observables.

Jets are clustered using the anti- $k_t$  algorithm. An upper and lower  $p_T$  cut are applied after jet clustering to each sample to ensure similar  $p_T$  spectra in each bin. The bins in leading jet  $p_T$  that are investigated for top tagging are 600-700 GeV, 1-1.1 TeV, and 1.5-1.6 TeV. Jets are clustered with radii  $R = 0.4, 0.8$ , and 1.2;  $R = 0.4$  jets are only studied in the 1.5-1.6 TeV bin because for top quarks with this boost, the top decay products are all contained within an  $R = 0.4$  jet.

## 7.1 Methodology

We study a number of top-tagging strategies, in particular:

1. HEPTopTagger
2. Johns Hopkins Tagger (JH)
3. Trimming
4. Pruning

The top taggers have criteria for reconstructing a top and  $W$  candidate, and a corresponding top and  $W$  mass, as described in Section 3.3, while the grooming algorithms (trimming and pruning) do not incorporate a  $W$ -identification step. For a level playing field, where grooming is used we construct a  $W$  candidate mass,  $m_W$ , from the three leading subjets by taking the mass of the pair of subjets with the smallest invariant mass; in the case that only two subjets are reconstructed, we take the mass of the leading subjet. The top mass,  $m_t$ , is the mass of the groomed jet. All of the above taggers and groomers incorporate a step to remove pile-up and other soft radiation.

We also consider the performance of the following jet shape observables:

- The ungroomed jet mass.
- $N$ -subjettiness ratios  $\tau_2/\tau_1$  and  $\tau_3/\tau_2$  with  $\beta = 1$  and the “winner-takes-all” axes.
- 2-point energy correlation function ratios  $C_2^{\beta=1}$  and  $C_3^{\beta=1}$ .
- The pruned Qjet mass volatility,  $\Gamma_{\text{Qjet}}$ .

In addition to the jet shape performance, we combine the jet shapes with the mass-reconstruction methods described above to determine the optimal combined performance.

For determining the performance of multiple variables, we combine the relevant tagger output observables and/or jet shapes into a boosted decision tree (BDT), which determines the optimal cut. Additionally, because each tagger has two input parameters, as described in Section 3.3, we scan over reasonable values of the parameters to determine the optimal value that gives the largest background rejection for each top tagging signal efficiency. This allows a direct comparison of the optimized version of each tagger. The input values scanned for the various algorithms are:

- **HEPTopTagger:**  $m \in [30, 100]$  GeV,  $\mu \in [0.5, 1]$
- **JH Tagger:**  $\delta_p \in [0.02, 0.15]$ ,  $\delta_R \in [0.07, 0.2]$
- **Trimming:**  $f_{\text{cut}} \in [0.02, 0.14]$ ,  $R_{\text{trim}} \in [0.1, 0.5]$
- **Pruning:**  $z_{\text{cut}} \in [0.02, 0.14]$ ,  $R_{\text{cut}} \in [0.1, 0.6]$

## 7.2 Single-observable performance

We start by investigating the behaviour of individual jet substructure observables. Because of the rich, three-pronged structure of the top decay, it is expected that combinations of masses and jet shapes will far outperform single observables in identifying boosted tops. However, a study of the top-tagging performance of single variables facilitates a direct comparison with the  $W$  tagging results in Section 6, and also allows a straightforward examination of the performance of each observable for different  $p_T$  and jet radius.

Fig. 28 shows the ROC curves for each of the top-tagging observables, with the bare (ungroomed) jet mass also plotted for comparison. The jet shape observables all perform substantially worse than jet mass, unlike  $W$  tagging for which several observables are competitive with or perform better than jet mass (see, for example, Fig. 10). To understand why this is the case, consider  $N$ -subjettiness. The  $W$  is two-pronged and the top is three-pronged; therefore, we expect  $\tau_{21}$  and  $\tau_{32}$  to be the best-performant  $N$ -subjettiness ratio, respectively. However,  $\tau_{21}$  also contains an implicit cut on the denominator,  $\tau_1$ , which is strongly correlated with jet mass. Therefore,  $\tau_{21}$  combines both mass and shape information to some extent. By contrast, and as is clear in Fig. 28(a), the best shape for top tagging is  $\tau_{32}$ , which contains no information on the mass. Therefore, it is unsurprising that the shapes most useful for top tagging are less sensitive to the jet mass, and under-perform relative to the corresponding observables for  $W$  tagging.

Of the two top tagging algorithms, we can see from Figure 28 that the Johns Hopkins (JH) tagger out-performs the HEPTopTagger in terms of its signal-to-background separation power in both the top and  $W$  candidate masses. In Figure 29 we show the histograms for the top mass output from the JH and HEPTopTagger for different  $R$  in the  $p_T$  1.5-1.6 TeV bin, and in Figure 30 for different  $p_T$  at  $R = 0.8$ , optimized at a signal efficiency of 30%. One can see from these figures that the likely reason for the better performance of the JH tagger is that, in the HEPTopTagger algorithm, the jet is filtered to select the five hardest subjets, and then three subjets are chosen which reconstruct the top mass. This requirement tends to shape a peak in the QCD background around  $m_t$  for the HEPTopTagger, while the JH tagger has no such requirement. It has been suggested by Anders *et al.* [50] that performance in the HEPTopTagger may be improved by selecting the three subjets reconstructing the top only among those that pass the  $W$  mass constraints, which somewhat reduces the shaping of the background. The discrepancy between the JH and HEPTopTaggers is more pronounced at higher  $p_T$  and larger jet radius (see Figs. 33 and 36).

We also see in Figure 28(b) that the top mass from the JH tagger and the HEPTopTagger has superior performance

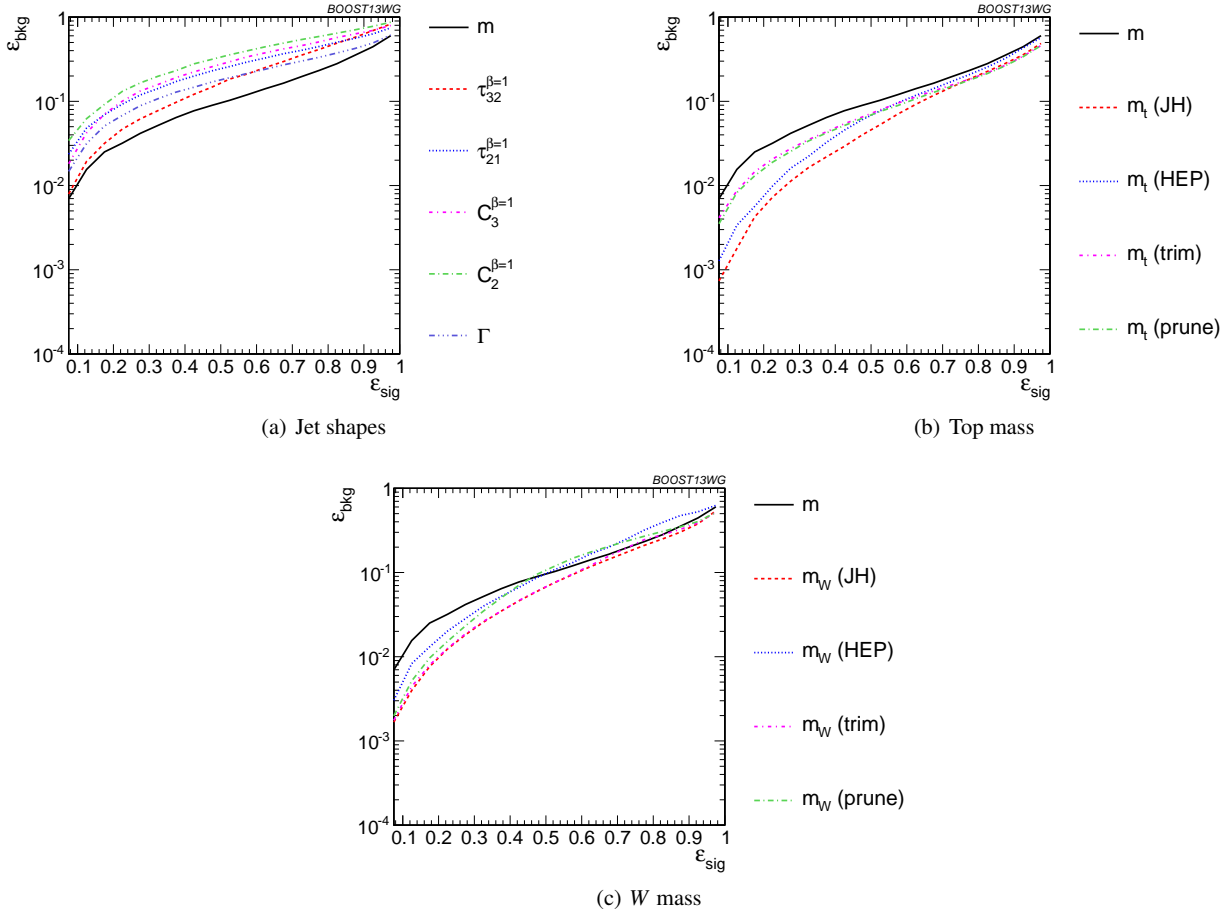


**Fig. 28** Comparison of single-variable top-tagging performance in the  $p_T = 1 - 1.1$  GeV bin using the anti- $k_T$ ,  $R=0.8$  algorithm.

relative to either of the grooming algorithms; this is because the pruning and trimming algorithms do not have inherent  $W$ -identification steps and are not optimized for this purpose. Indeed, because of the lack of a  $W$ -identification step, grooming algorithms are forced to strike a balance between under-grooming the jet, which broadens the signal peak due to UE contamination and features a larger background rate, and over-grooming the jet, which occasionally throws out the  $b$ -jet and preserves only the  $W$  components inside the jet. We demonstrate this effect in Figures 29 and 30, showing that with  $\epsilon_{\text{sig}} = 0.3 - 0.35$ , the optimal performance of the tagger over-grooms a substantial fraction of the jets (20–30%), leading to a spurious second peak at the  $W$  mass. This effect is more pronounced at large  $R$  and  $p_T$ , since more aggressive grooming is required in these limits to combat the increased contamination from UE and QCD radiation.

In Figures 31 and 33 we directly compare ROC curves for jet shape observable performance and top mass performance respectively in the three different  $p_T$  bins considered whilst keeping the jet radius fixed at  $R=0.8$ . The input parameters of the taggers, groomers and shape variables are separately optimized in each  $p_T$  bin. One can see from Figure

31 that the tagging performance of jet shapes do not change substantially with  $p_T$ . The observables  $\tau_{32}^{(\beta=1)}$  and Qjet volatility  $\Gamma$  have the most variation and tend to degrade with higher  $p_T$ , as can be seen in Figure 32. This makes sense, as higher- $p_T$  QCD jets have more, harder emissions within the jet, giving rise to substructure that fakes the signal. By contrast, from Figure 33 we can see that most of the top mass observables have superior performance at higher  $p_T$  due to the radiation from the top quark becoming more collimated. The notable exception is the HEPTopTagger, which degrades at higher  $p_T$ , likely in part due to the background-shaping effects discussed earlier.

In Figures 34 and 36 we directly compare ROC curves for jet shape observable performance and top mass performance respectively for the three different jet radii considered within the  $p_T$  1.5–1.6 TeV bin. Again, the input parameters of the taggers, groomers and shape variables are separately optimized for each jet radius. We can see from these figures that most of the top tagging variables, both shape and reconstructed top mass, perform best for smaller radius. This is likely because, at such high  $p_T$ , most of the radiation from the top quark is confined within  $R = 0.4$ , and having a larger

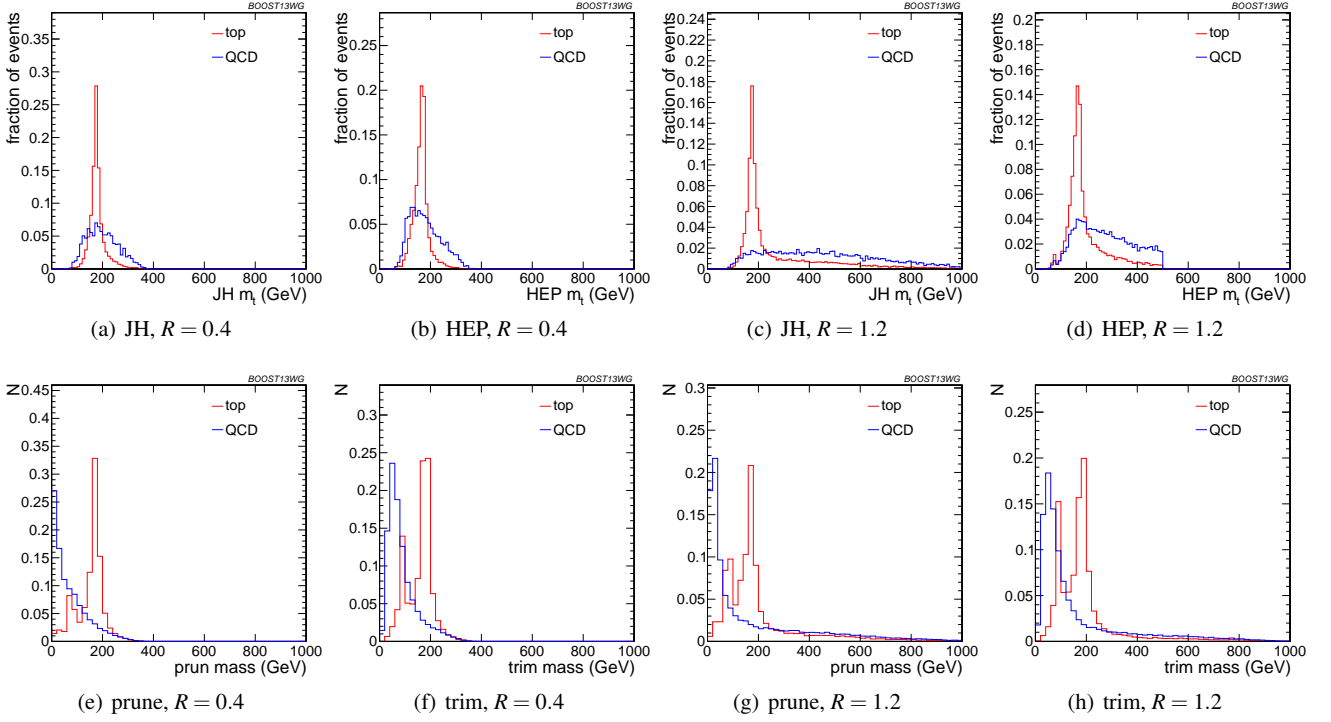


**Fig. 29** Comparison of top mass reconstruction with the Johns Hopkins (JH), HEPTopTaggers (HEP), pruning, and trimming at different  $R$  using the anti- $k_T$  algorithm,  $p_T = 1.5 - 1.6$  TeV. Each histogram is shown for the working point optimized for best performance with  $m_t$  in the  $0.3 - 0.35$  signal efficiency bin, and is normalized to the fraction of events passing the tagger. In this and subsequent plots, the HEPTopTagger distribution cuts off at 500 GeV because the tagger fails to tag jets with a larger mass.

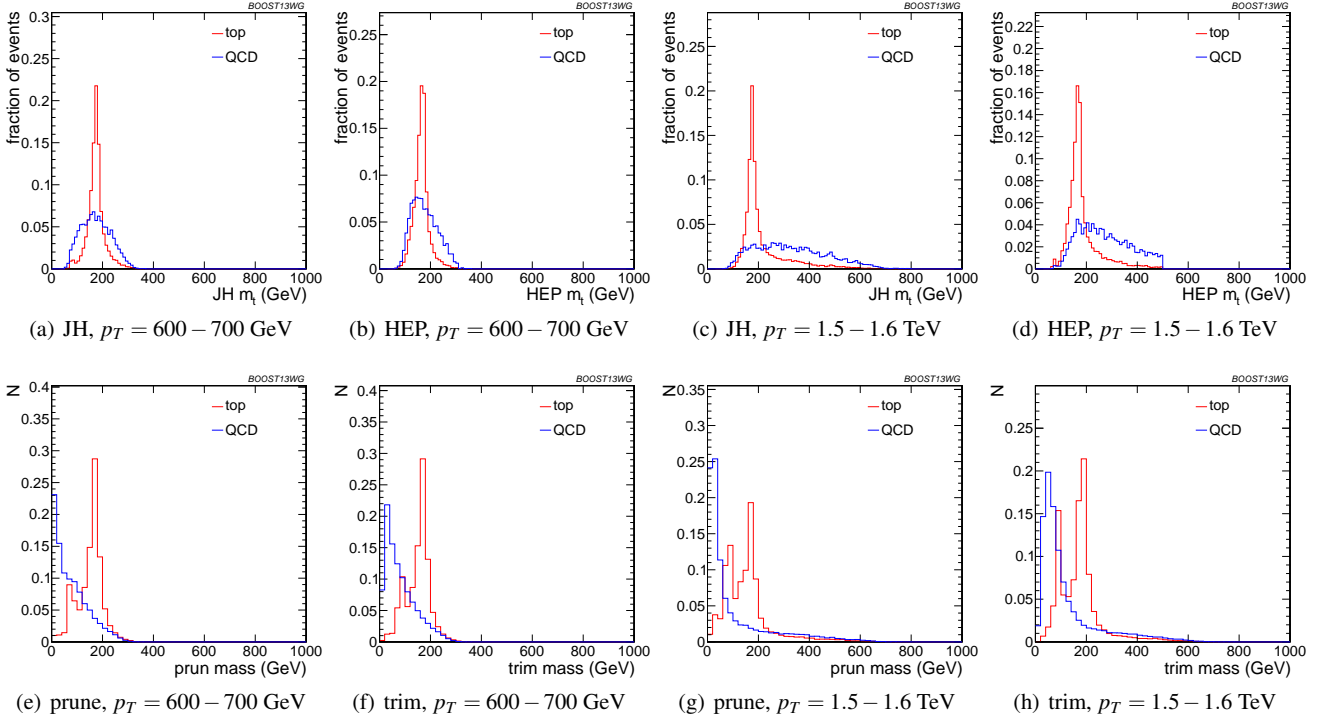


**Fig. 30** Comparison of top mass reconstruction with the Johns Hopkins (JH), HEPTopTaggers (HEP), pruning, and trimming at different  $p_T$  using the anti- $k_T$  algorithm,  $R = 0.8$ . Each histogram is shown for the working point optimized for best performance with  $m_t$  in the  $0.3 - 0.35$  signal efficiency bin, and is normalized to the fraction of events passing the tagger.

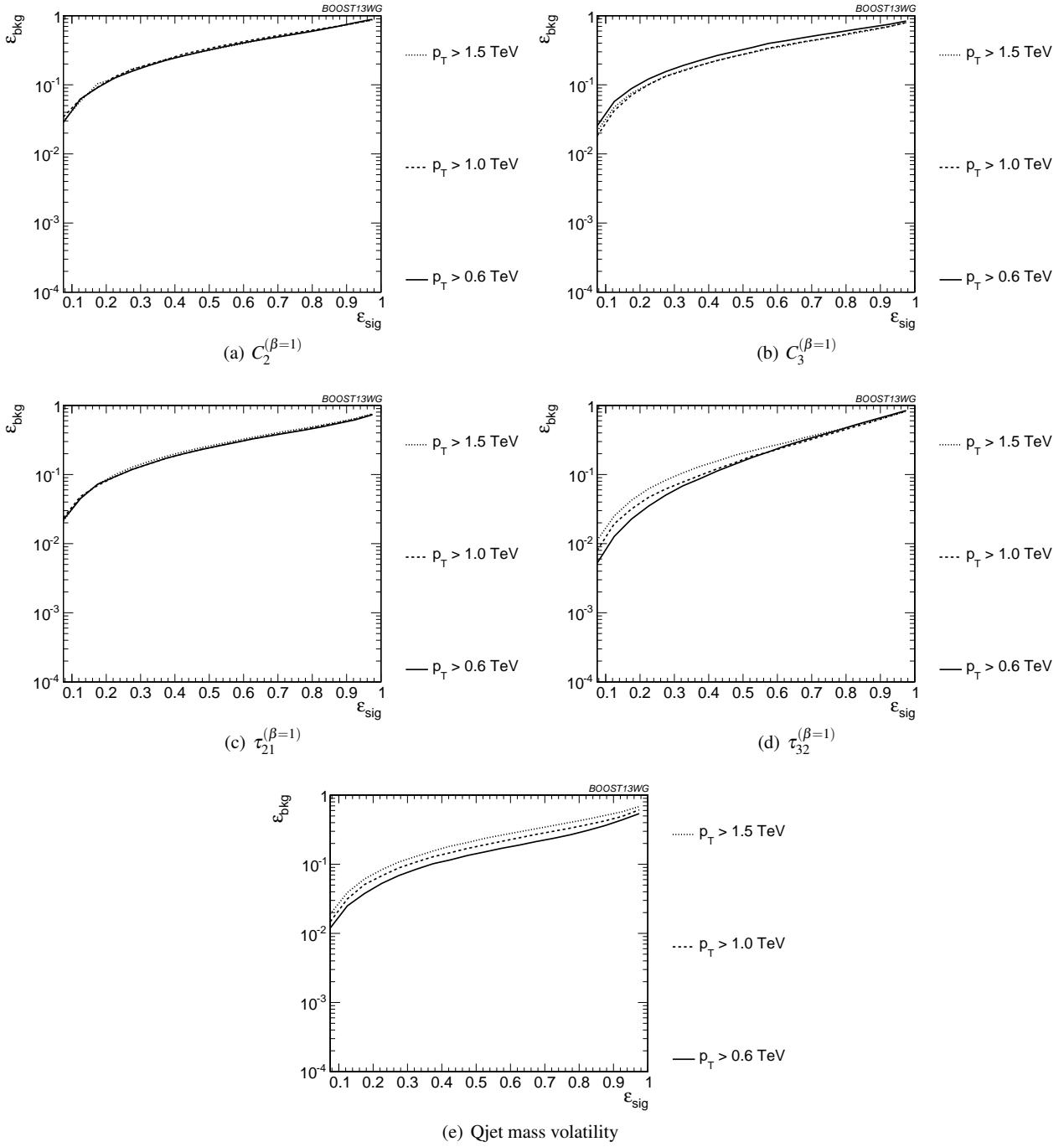


**Fig. 31** Comparison of individual jet shape performance at different  $p_T$  using the anti- $k_T$   $R=0.8$  algorithm.

jet radius makes the observable more susceptible to contamination from the underlying event and other uncorrelated radiation. In Figure 35, we compare the individual top signal and QCD background distributions for each shape variable considered in the  $p_T$  1.5-1.6 TeV bin for the various jet radii. One can see that the distributions for both signal and background broaden with increasing  $R$ , degrading the discriminating power. For  $C_2^{(\beta=1)}$  and  $C_3^{(\beta=1)}$ , the background distributions

are shifted upward as well. Therefore, the discriminating power generally gets worse with increasing  $R$ . The main exception is for  $C_3^{(\beta=1)}$ , which performs optimally at  $R = 0.8$ ; in this case, the signal and background coincidentally happen to have the same distribution around  $R = 0.4$ , and so  $R = 0.8$  gives better discrimination.



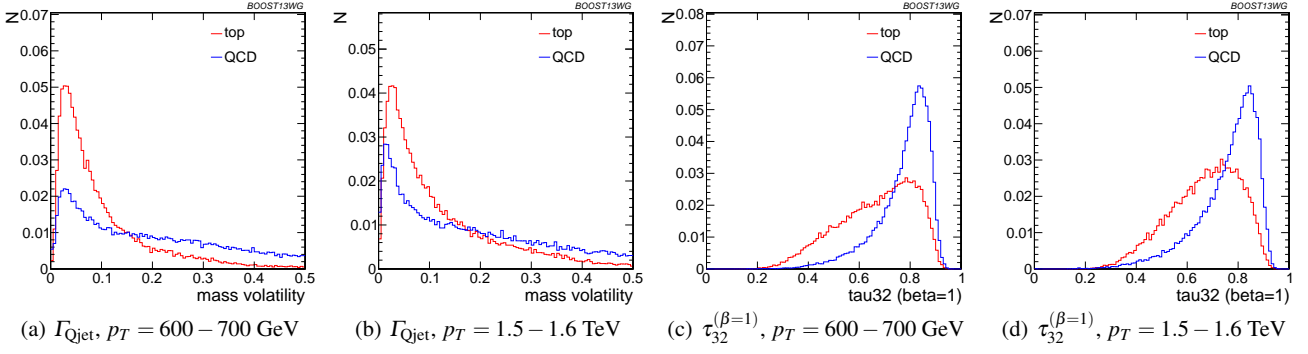


**Fig. 32** Comparison of  $\Gamma_{Qjet}$  and  $\tau_{32}^{\beta=1}$  at  $R = 0.8$  and different values of the  $p_T$ . These shape observables are the most sensitive to varying  $p_T$ .

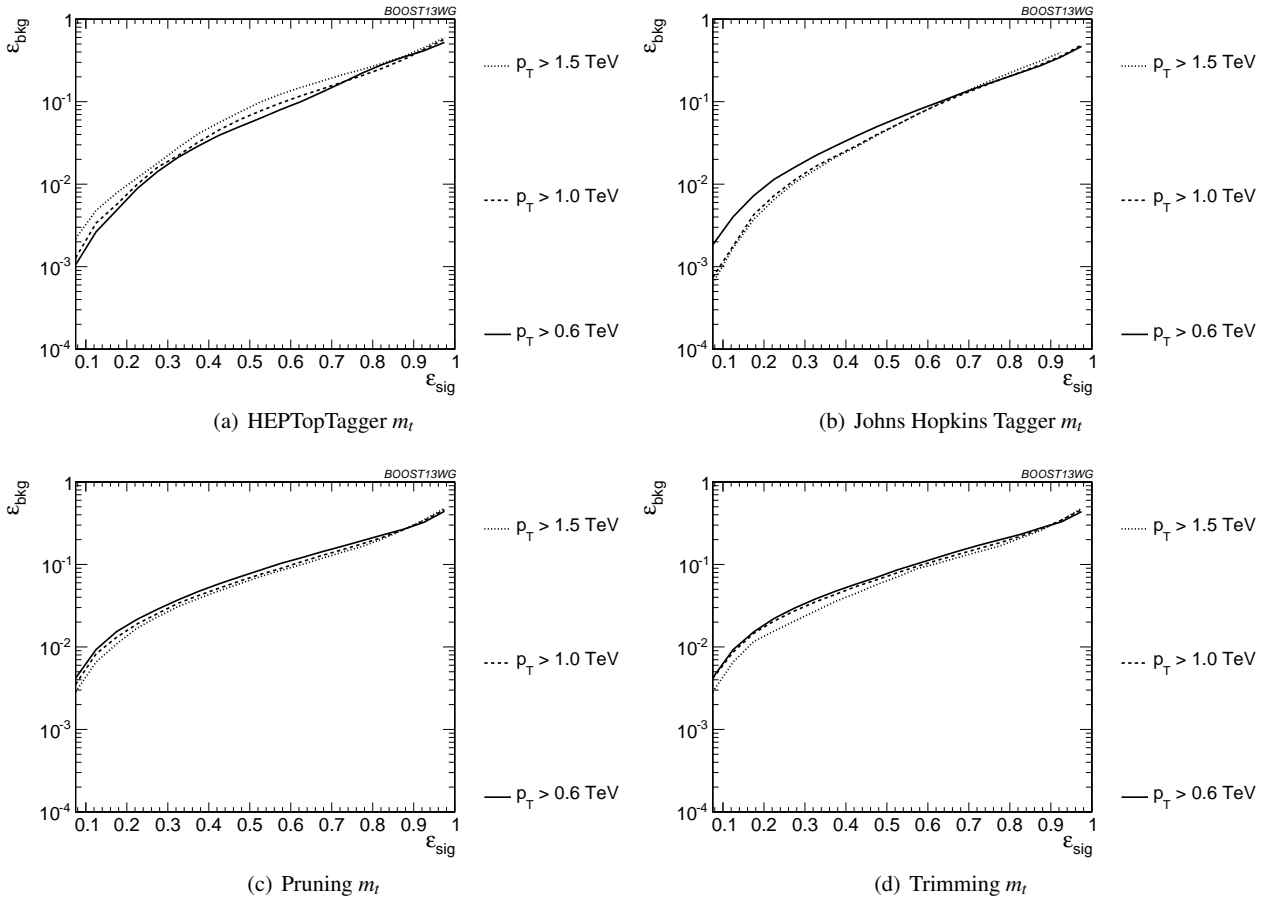


**Fig. 33** Comparison of top mass performance of different taggers at different  $p_T$  using the anti- $k_T$   $R=0.8$  algorithm.

### 7.3 Performance of multivariable combinations

We now consider various BDT combinations of the observables from Section 7.2, using the techniques described in Section 4. In particular, we consider the performance of individual taggers such as the JH tagger and HEPTopTagger, which output information about the top and  $W$  candidate masses and the helicity angle; groomers, such as trimming and pruning, which remove soft, uncorrelated radiation from

the top candidate to improve mass reconstruction, and to which we have added a  $W$  reconstruction step; and the combination of the outputs of the above taggers/groomers, both with each other, and with shape variables such as  $N$ -subjettiness ratios and energy correlation ratios. For all observables with tuneable input parameters, we scan and optimize over realistic values of such parameters, as described in Section 7.1.

In Figure 37, we directly compare the performance of the HEPTopTagger, the JH tagger, trimming, and pruning, in

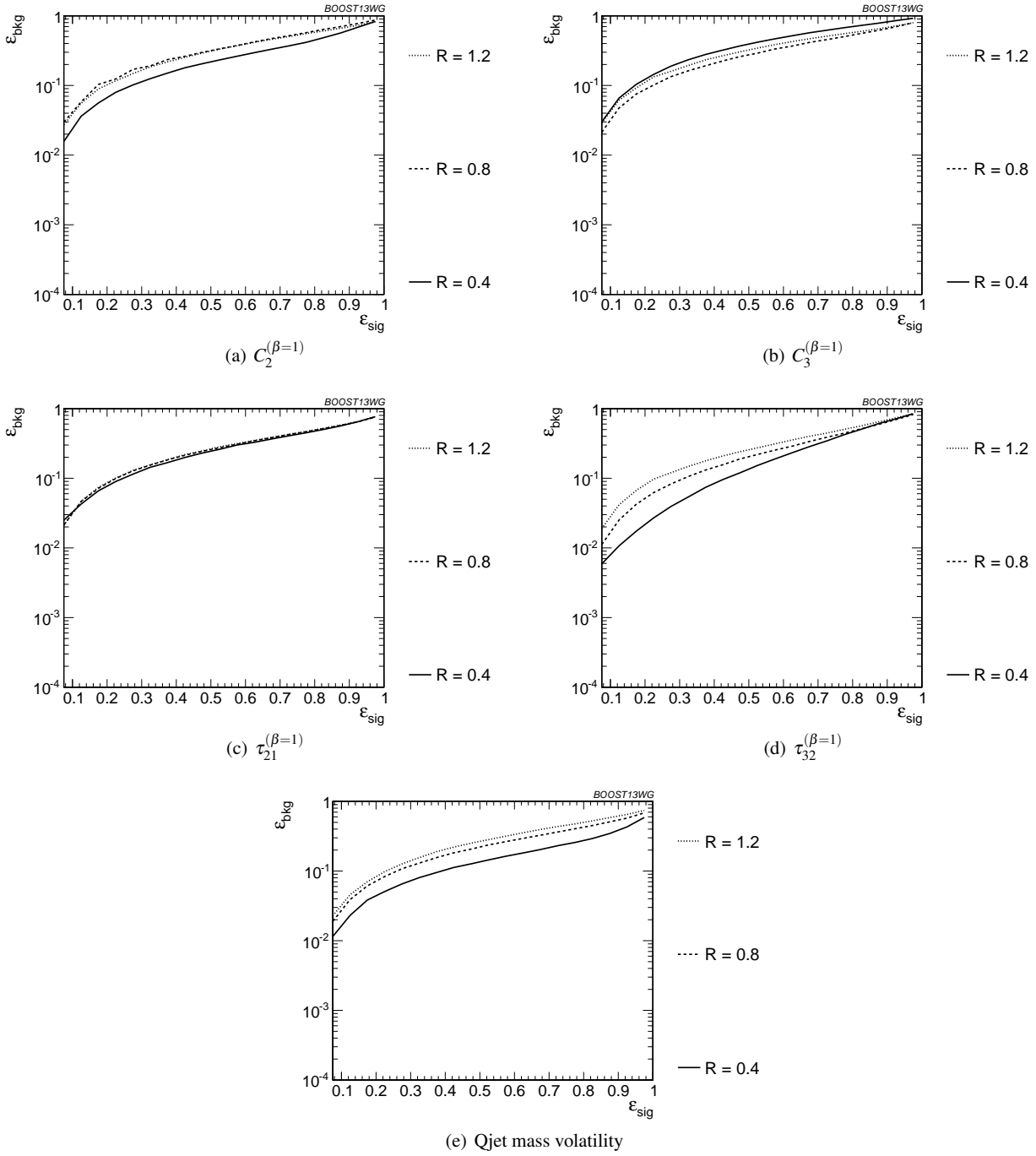


**Fig. 34** Comparison of individual jet shape performance at different  $R$  in the  $p_T = 1.5 - 1.6$  TeV bin.

the  $p_T = 1 - 1.1$  TeV bin using jet radius  $R=0.8$ , where both  $m_t$  and  $m_W$  are used in the groomers. Generally, we find that pruning, which does not naturally incorporate subjets into the algorithm, does not perform as well as the others. Interestingly, trimming, which does include a subjet-identification step, performs comparably to the HEPTopTagger over much of the range, possibly due to the background-shaping observed in Section 7.2. By contrast, the JH tagger outperforms

the other algorithms. To determine whether there is complementary information in the mass outputs from different top taggers, we also consider in Figure 37 a multivariable combination of all of the JH and HEPTopTagger outputs. The maximum efficiency of the combined JH and HEPTopTaggers is limited, as some fraction of signal events inevitably fails either one or other of the taggers. We do see a 20-50% improvement in performance when combining all outputs,

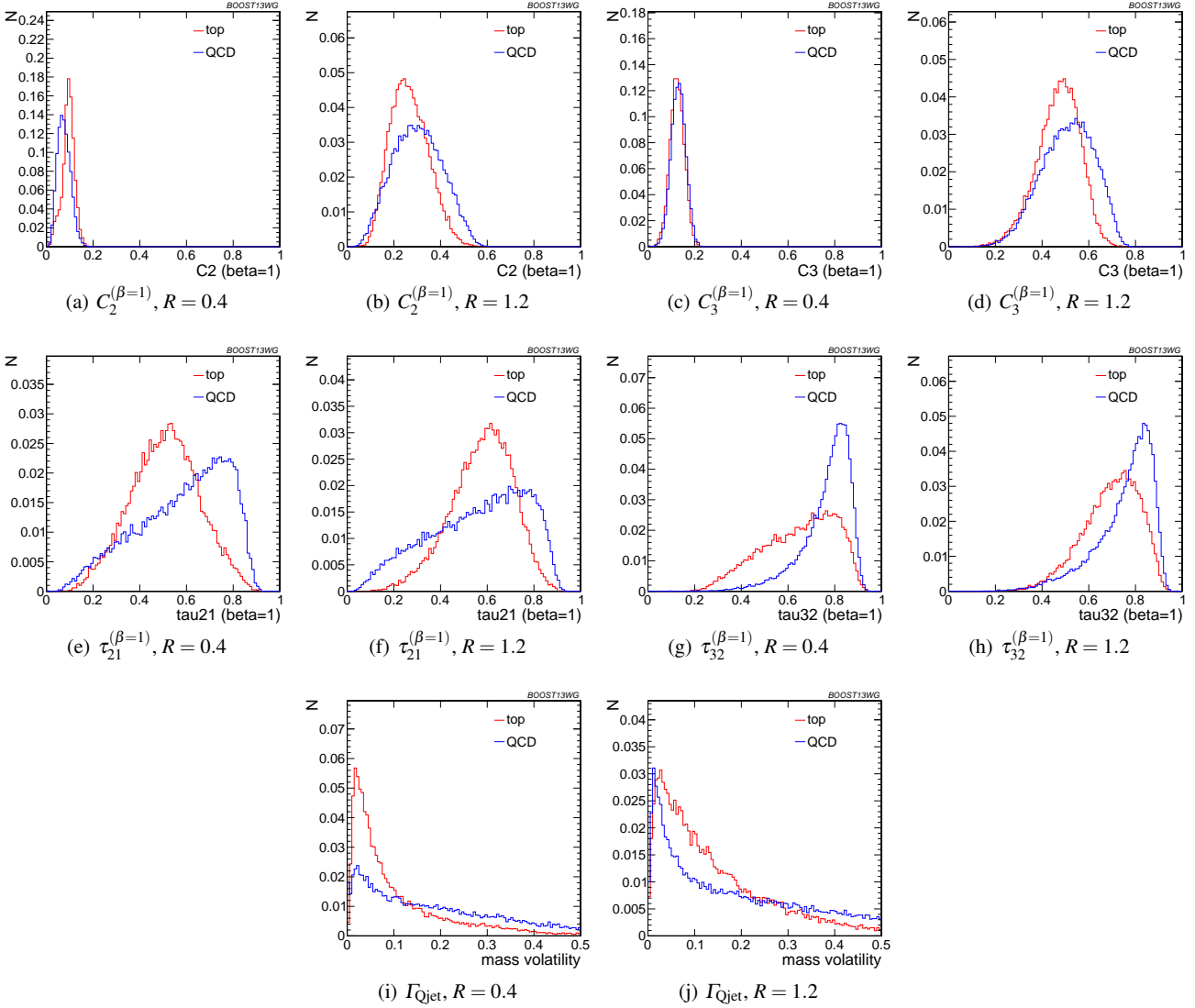


**Fig. 35** Comparison of various shape observables in the  $p_T = 1.5 - 1.6$  TeV bin and different values of the anti- $k_T$  radius  $R$ .

which suggests that the different algorithms used to identify the top and  $W$  for different taggers contains complementary information.

In Figure 38 we present the results for multivariable combinations of the top tagger outputs with and without shape variables. We see that, for both the HEPTopTagger and the JH tagger, the shape observables contain additional information uncorrelated with the masses and helicity angle, and give on average a factor 2-3 improvement in signal discrimination. We see that, when combined with the tagger outputs, both the energy correlation functions  $C_2 + C_3$  and the  $N$ -subjettiness ratios  $\tau_{21} + \tau_{32}$  give comparable performance while the Qjet mass volatility is slightly worse; this is unsurprising, as Qjets accesses shape information in a more indirect way from other shape observables. Combining all shape observables with a single top tagger provides even

greater enhancement in discrimination power. We directly compare the performance of the JH and HEPTopTaggers in Figure 38(c). Combining the taggers with shape information nearly erases the difference between the tagging methods observed in Figure 37; this indicates that combining the shape information with the HEPTopTagger identifies the differences between signal and background missed by the tagger alone. This also suggests that further improvement to discriminating power may be minimal, as various multivariable combinations are converging to within a factor of 20% or so.

In Figure 39 we present the results for multivariable combinations of groomer outputs with and without shape variables. As with the tagging algorithms, combinations of groomers with shape observables improves their discriminating power; combinations with  $\tau_{32} + \tau_{21}$  perform comparably to those

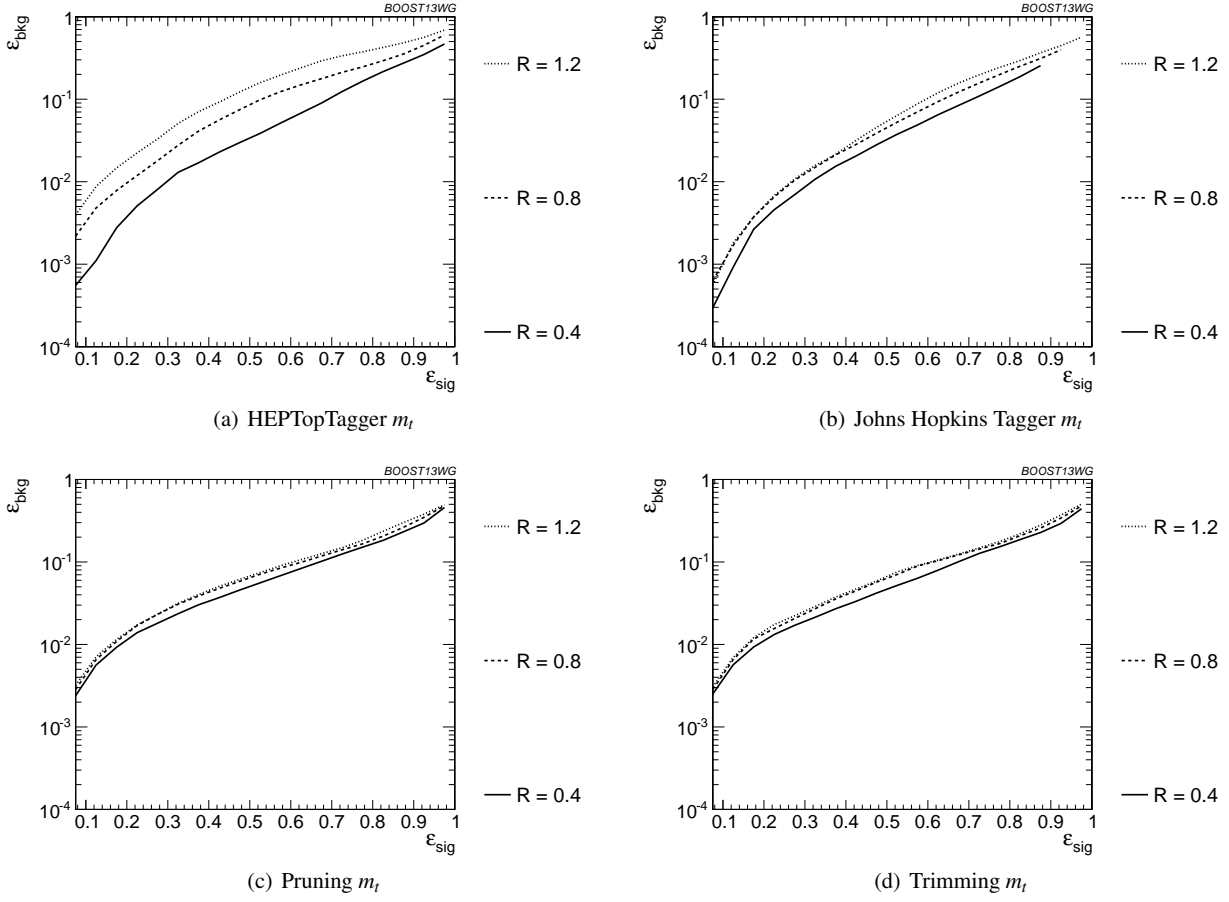


**Fig. 36** Comparison of top mass performance of different taggers at different  $R$  in the  $p_T = 1.5 - 1.6$  TeV bin.

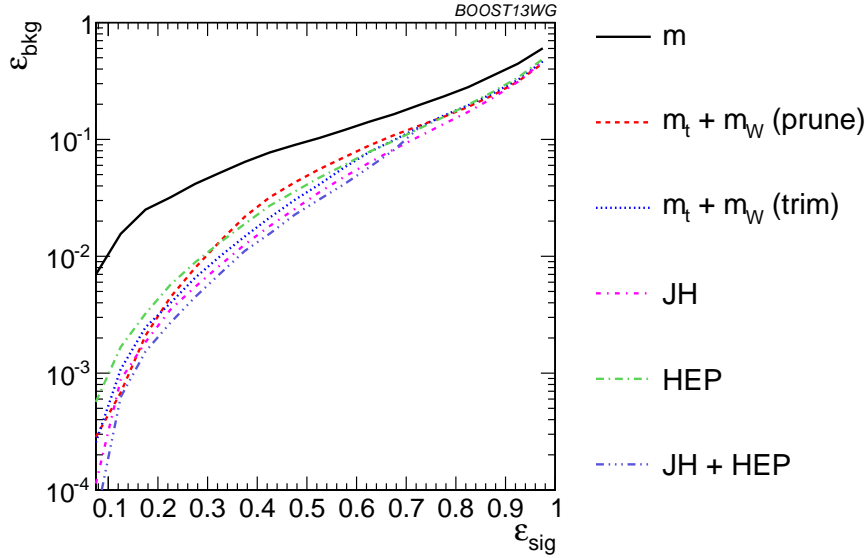


**Fig. 37** The performance of the various taggers in the  $p_T = 1 - 1.1$  TeV bin using the anti- $k_T$   $R=0.8$  algorithm. For the groomers a BDT combination of the reconstructed  $m_t$  and  $m_W$  are used. Also shown is a multivariable combination of all of the JH and HEPTopTagger outputs. The ungroomed mass performance is shown for comparison.

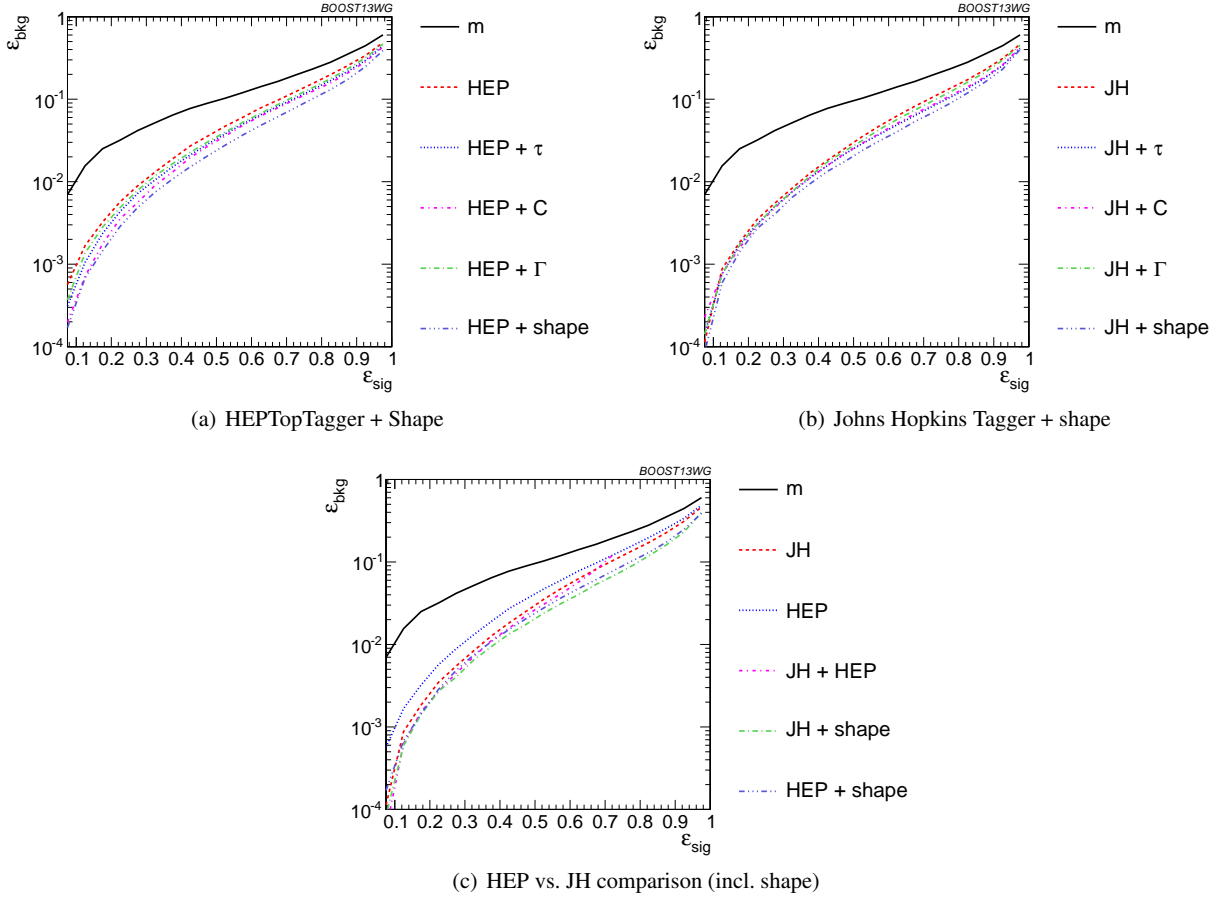


**Fig. 38** The performance of BDT combinations of the JH and HepTopTagger outputs with various shape observables in the  $p_T = 1 - 1.1$  TeV bin using the anti- $k_T$   $R=0.8$  algorithm. Taggers are combined with the following shape observables:  $\tau_{21}^{(\beta=1)} + \tau_{32}^{(\beta=1)}$ ,  $C_2^{(\beta=1)} + C_3^{(\beta=1)}$ ,  $\Gamma_{\text{Qjet}}$ , and all of the above (denoted “shape”).

with  $C_3 + C_2$ , and both of these are superior to combinations with the mass volatility,  $\Gamma$ . Substantial improvement is further possible by combining the groomers with all shape observables. Not surprisingly, the taggers that lag behind in performance enjoy the largest gain in signal-background discrimination with the addition of shape observables. Once again, in Figure 39(c), we find that the differences between pruning and trimming are erased when combined with shape information.

Finally, in Figure 40, we compare the performance of each of the tagger/groomers when their outputs are combined with all of the shape observables considered. One can see that the discrepancies between the performance of the different taggers/groomers all but vanishes, suggesting perhaps that we are here utilising all available signal-background discrimination information, and that this is the optimal tagging performance that could be achieved in these conditions.

Up to this point we have just considered the combined multivariable performance in the  $p_T$  1.0-1.1 TeV bin with jet radius  $R=0.8$ . We now compare the BDT combinations

of tagger outputs, with and without shape variables, at different  $p_T$ . The taggers are optimized over all input parameters for each choice of  $p_T$  and signal efficiency. As with the single-variable study, we consider anti- $k_T$  jets clustered with  $R = 0.8$  and compare the outcomes in the  $p_T = 500 - 600$  GeV,  $p_T = 1 - 1.1$  TeV, and  $p_T = 1.5 - 1.6$  TeV bins. The comparison of the taggers/groomers is shown in Figure 41. The behaviour with  $p_T$  is qualitatively similar to the behaviour of the  $m_t$  observable for each tagger/groomer shown in Figure 33; this suggests that the  $p_T$  behaviour of the taggers is dominated by the top mass reconstruction. As before, the HEPTopTagger performance degrades slightly with increased  $p_T$  due to the background shaping effect, while the JH tagger and groomers modestly improve in performance.

In Figure 42, we show the  $p_T$  dependence of BDT combinations of the JH tagger output combined with shape observables. We find that the curves look nearly identical: the  $p_T$  dependence is dominated by the top mass reconstruction, and combining the tagger outputs with different shape observables does not substantially change this behaviour. The same holds true for trimming and pruning. By contrast,

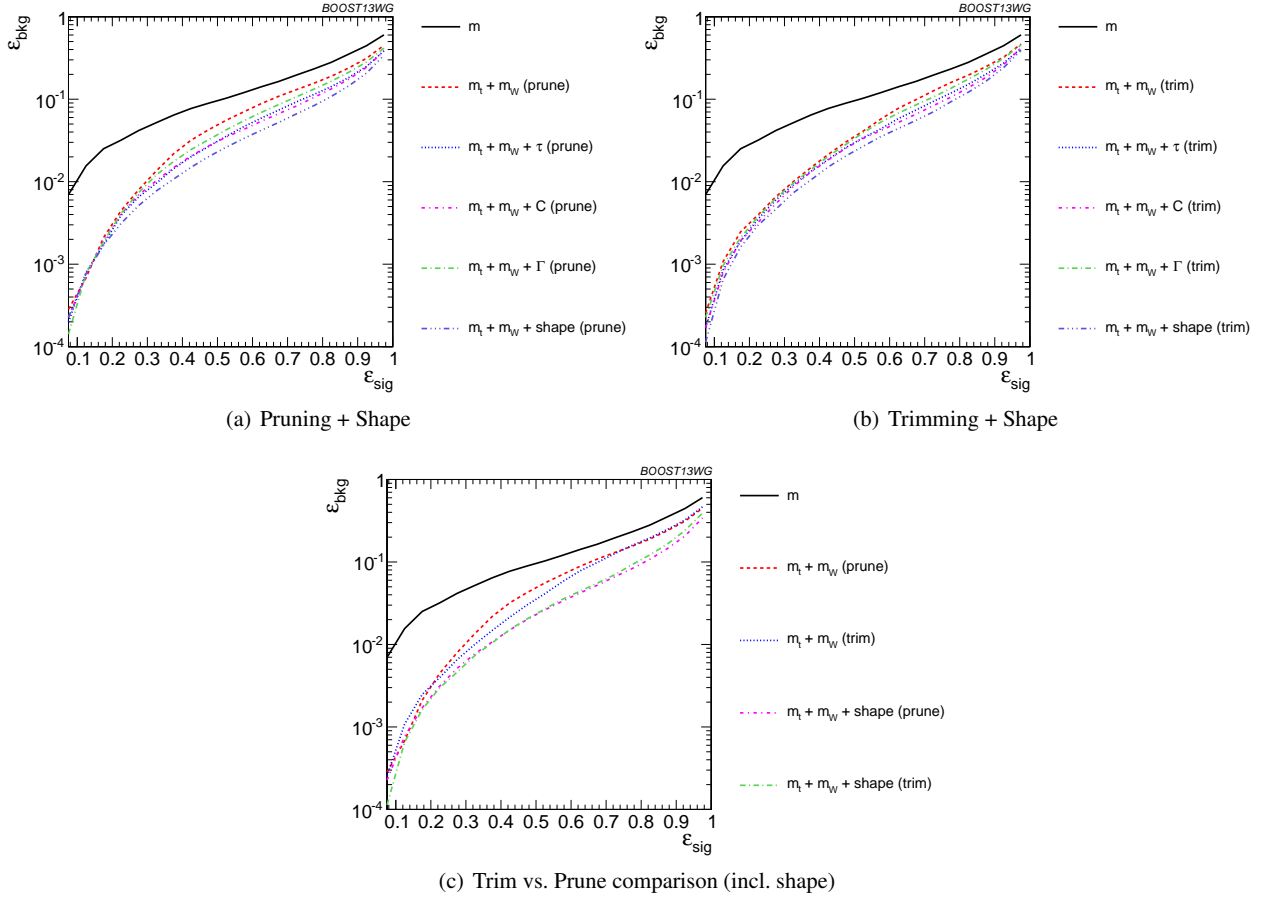


**Fig. 39** The performance of the BDT combinations of the trimming and pruning outputs with various shape observables in the  $p_T = 1 - 1.1$  TeV bin using the anti- $k_T$   $R=0.8$  algorithm. Groomer mass outputs are combined with the following shape observables:  $\tau_{21}^{(\beta=1)} + \tau_{32}^{(\beta=1)}$ ,  $C_2^{(\beta=1)} + C_3^{(\beta=1)}$ ,  $\Gamma_{\text{Qjet}}$ , and all of the above (denoted “shape”).

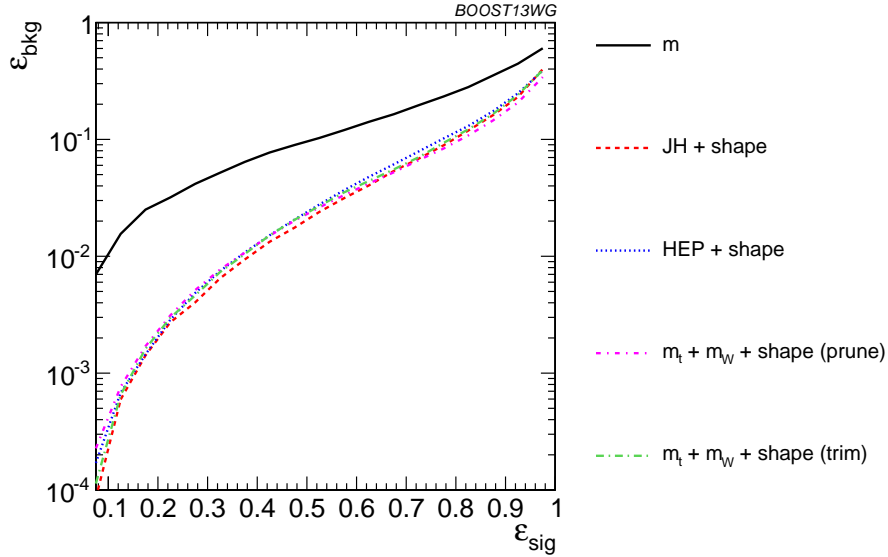


**Fig. 40** Comparison of the performance of the BDT combinations of all the groomer/tagger outputs with all the available shape observables in the  $p_T = 1 - 1.1$  TeV bin using the anti- $k_T$   $R=0.8$  algorithm. Tagger/groomer outputs are combined with all of the following shape observables:  $\tau_{21}^{(\beta=1)} + \tau_{32}^{(\beta=1)}$ ,  $C_2^{(\beta=1)} + C_3^{(\beta=1)}$ ,  $\Gamma_{\text{Qjet}}$ .



HEPTopTagger ROC curves, shown in Figure 43, do change somewhat when combined with different shape observables due to the suboptimal performance of the HEPTopTagger at high  $p_T$ , we find that combining the HEPTopTagger with  $C_3^{(\beta=1)}$ , which in Figure 31(b) is seen to have some modest improvement at high  $p_T$ , can improve its performance. Combining the HEPTopTagger with multiple shape observables gives the maximum improvement in performance at high  $p_T$  relative to at low  $p_T$ .

In Figure 44 we compare the BDT combinations of tagger outputs, with and without shape variables, at different jet radius  $R$  in the  $p_T = 1.5 - 1.6$  TeV bin. The taggers are optimized over all input parameters for each choice of  $R$  and signal efficiency. We find that, for all taggers and groomers, the performance is always best at small  $R$ ; the choice of  $R$  is sufficiently large to admit the full top quark decay at such high  $p_T$ , but is small enough to suppress contamination from additional radiation. This is not altered when the taggers are combined with shape observable. For example, in Figure 45 is shown the dependence on  $R$  of the JH tagger when combined with shape observables, where one can see that the  $R$ -dependence is identical for all combinations. The same holds true for the HEPTopTagger, trimming, and pruning.

#### 7.4 Performance at Sub-Optimal Working Points

Up until now, we have re-optimized our tagger and groomer parameters for each  $p_T$ ,  $R$ , and signal efficiency working point. In reality, experiments will choose a finite set of working points to use. How do our results hold up when this is taken into account? To address this concern, we replicate our analyses, but only optimize the top taggers for a particular  $p_T/R$ /efficiency and apply the same parameters to other scenarios. This allows us to determine the extent to which re-optimization is necessary to maintain the high signal-background discrimination power seen in the top tagging algorithms we study. The shape observables typically do not have any input parameters to optimize. Therefore, we focus on the taggers and groomers, and their combination with shape observables, in this section.

**Optimizing at a single  $p_T$ :** We show in Figure 46 the performance of the top taggers, using just the reconstructed top mass as the discriminating variable, with all input parameters optimized to the  $p_T = 1.5 - 1.6$  TeV bin, relative to the performance optimized at each  $p_T$ . We see that while the performance degrades by about 50% when the high- $p_T$  optimized points are used at other momenta, this is only an order-one adjustment of the tagger performance, with trimming and the Johns Hopkins tagger degrading the most. The jagged behaviour of the points is due to the finite resolution of the scan. We also observe a particular effect associated

with using suboptimal taggers: since taggers sometimes fail to return a top candidate, parameters optimized for a particular efficiency  $\epsilon_S$  at  $p_T = 1.5 - 1.6$  TeV may not return enough signal candidates to reach the same efficiency at a different  $p_T$ . Consequently, no point appears for that  $p_T$  value. This is not often a practical concern, as the largest gains in signal discrimination and significance are for smaller values of  $\epsilon_S$ , but it is something that must be considered when selecting benchmark tagger parameters and signal efficiencies.

The degradation in performance is more pronounced for the BDT combinations of the full tagger outputs, shown in Figure 47), particularly at very low signal efficiency where the optimization picks out a cut on the tail of some distribution that depends precisely on the  $p_T/R$  of the jet. Once again, trimming and the Johns Hopkins tagger degrade more markedly. Similar behaviour holds for the BDT combinations of tagger outputs plus all shape observables.

**Optimizing at a single  $R$ :** We perform a similar analysis, optimizing tagger parameters for each signal efficiency at  $R = 1.2$ , and then use the same parameters for smaller  $R$ , in the  $p_T$  1.5-1.6 TeV bin. In Figure 48 we show the ratio of the performance of the top taggers, using just the reconstructed top mass as the discriminating variable, with all input parameters optimized to the  $R = 1.2$  values compared to input parameters optimized separately at each radius. While the performance of each observable degrades at small  $\epsilon_{\text{sig}}$  compared to the optimized search, the HEPTopTagger fares the worst as the observed is quite sensitive to the selected value of  $R$ . It is not surprising that a tagger whose top mass reconstruction is susceptible to background-shaping at large  $R$  and  $p_T$  would require a more careful optimization of parameters to obtain the best performance.

The same holds true for the BDT combinations of the full tagger outputs, shown in Figure 49). The performance for the sub-optimal taggers is still within an  $O(1)$  factor of the optimized performance, and the HEPTopTagger performs better with the combination of all of its outputs relative to the performance with just  $m_t$ . The same behaviour holds for the BDT combinations of tagger outputs and shape observables.

**Optimizing at a single efficiency:** The strongest assumption we have made so far is that the taggers can be re-optimized for each signal efficiency point. This is useful for making a direct comparison of the power of different top tagging algorithms, but is not particularly practical for the LHC analyses. We now consider the effects when the tagger inputs are optimized once, in the  $\epsilon_S = 0.3 - 0.35$  bin, and then used to determine the full ROC curve. We do this in the  $p_T$  1 - 1.1 TeV bin and with  $R = 0.8$ .



**Fig. 41** Comparison of BDT combination of tagger performance at different  $p_T$  using the anti- $k_T$   $R=0.8$  algorithm.

The performance of each tagger, normalized to its performance optimized in each bin, is shown in Figure 50 for cuts on the top mass and  $W$  mass, and in Figure 51 for BDT combinations of tagger outputs and shape variables. In both plots, it is apparent that optimizing the taggers in the 0.3-0.35 efficiency bin gives comparable performance over efficiencies ranging from 0.2-0.5, although performance grades at small and large signal efficiencies. Pruning appears to give especially robust signal-background discrimination without re-optimization, possibly due to the fact that there are no absolute distance or  $p_T$  scales that appear in the algorithm. Figures 50 and 51 suggest that, while optimization at all signal efficiencies is a useful tool for comparing different algorithms, it is not crucial to achieve good top-tagging performance in experiments.

## 7.5 Conclusions

We have studied the performance of various jet substructure observables, groomed masses, and top taggers to study the performance of top tagging at different  $p_T$  and jet radius parameter. At each  $p_T$ ,  $R$ , and signal efficiency working point,

we optimize the parameters for those observables with tuneable inputs. Overall, we have found that these techniques, individually and in combination, continue to perform well at high  $p_T$ , which is important for future LHC running. In general, the Johns Hopkins tagger performs best, while jet grooming algorithms under-perform relative to the best top taggers due to the lack of an optimized  $W$ -identification step. Tagger performance can be improved by a further factor of 2-4 through combination with jet substructure observables such as  $\tau_{32}$ ,  $C_3$ , and  $Q_{\text{jet}}$  mass volatility; when combined with jet substructure observables, the performance of various groomers and taggers becomes very comparable, suggesting that, taken together, the observables studied are sensitive to nearly all of the physical differences between top and QCD jets. A small improvement is also found by combining the Johns Hopkins and HEPTopTaggers, indicating that different taggers are not fully correlated.

Comparing results at different  $p_T$  and  $R$ , top tagging performance is generally better at smaller  $R$  due to less contamination from uncorrelated radiation. Similarly, most observables perform better at larger  $p_T$  due to the higher degree of collimation of radiation. Some observables fare worse at

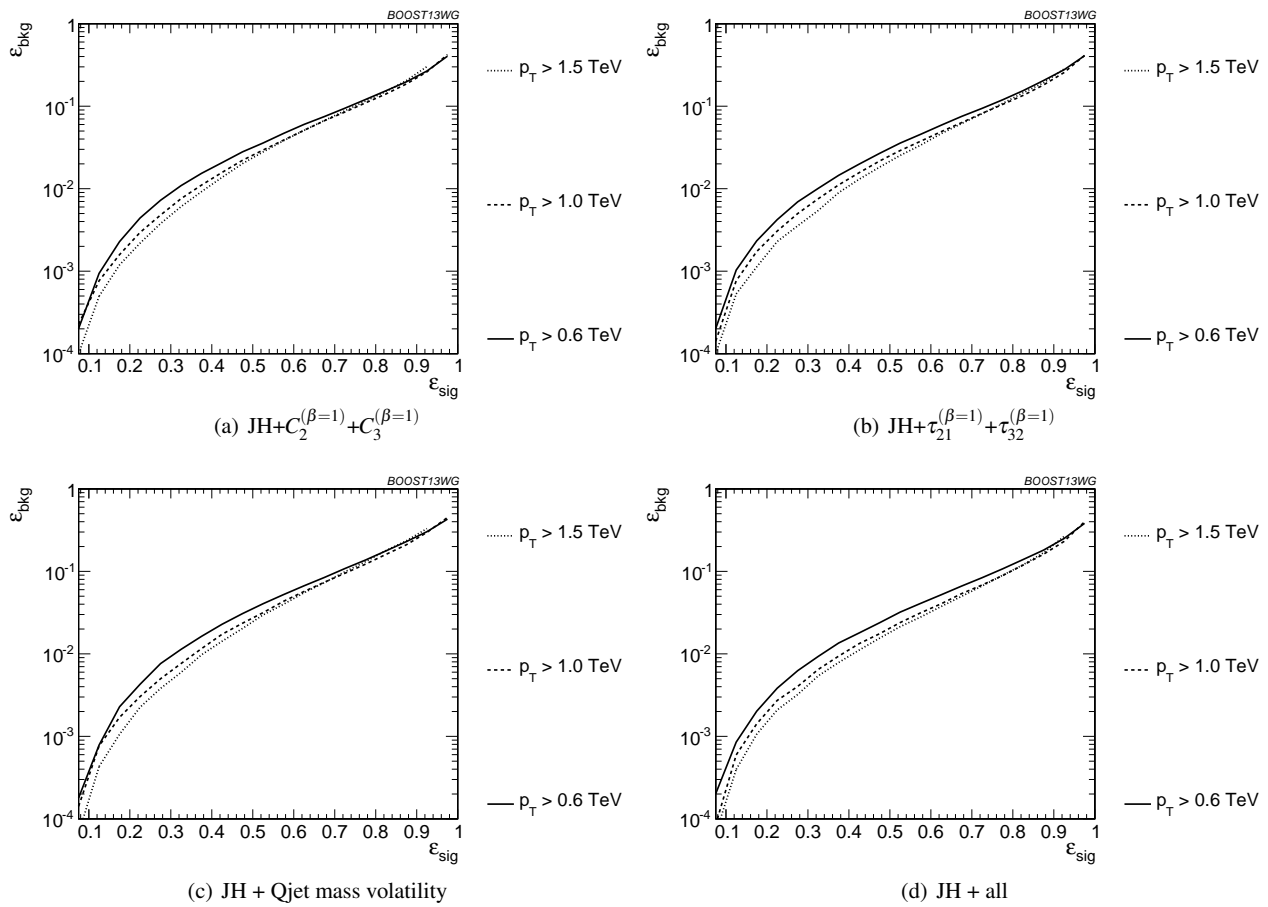


**Fig. 42** Comparison of BDT combination of JH tagger + shape at different  $p_T$  using the anti- $k_T$   $R=0.8$  algorithm.

higher  $p_T$ , such as the  $N$ -subjettiness ratio  $\tau_{32}$  and the Qjet mass volatility  $\Gamma$ , as higher- $p_T$  QCD jets have more, harder emissions that fake the top jet substructure. The HEPTopTagger is also worse at large  $p_T$  due to the tendency of the tagger to shape backgrounds around the top mass. The  $p_T$ - and  $R$ -dependence of the multivariable combinations dominated by the  $p_T$ - and  $R$ -dependence of the top mass reconstruction component of the tagger/groomer.

Finally, we consider the performance of various observable combinations under the more realistic assumption that the input parameters are only optimized at a single  $p_T$ ,  $R$ , or signal efficiency, and then the same inputs are used at other working points. Remarkably, the performance of all observables is typically within a factor of 2 of the fully optimized inputs, suggesting that while optimization can lead to substantial gains in performance, the general behaviour found in the fully optimized analyses extends to more general applications of each variable. In particular, the performance of pruning typically varies the least when comparing suboptimal working points to the fully optimized tagger due to the scale-invariant nature of the pruning algorithm.

## 8 Summary & Conclusions

In this report we have attempted to understand the degree to which the discriminatory information in various jet substructure observables/taggers overlaps, and how this varies as a function of the parameters of the jets, such as their  $p_T$  and radius. This has been done by combining the variables into BDT discriminants, and comparing the background rejection power of this discriminant to the rejection power achieved by the individual variables. The performance of “all variables” BDT discriminants has also been investigated, to understand the potential of the “ultimate” tagger where “all” available information (at least, all of that provided by the variables considered) is used.

## References

1. *Boost2009*, SLAC National Accelerator Laboratory, 9-10 July, 2009, [<http://www-conf.slac.stanford.edu/Boost2009>].
2. *Boost2010*, University of Oxford, 22-25 June 2010, [<http://www.physics.ox.ac.uk/boost2010>].

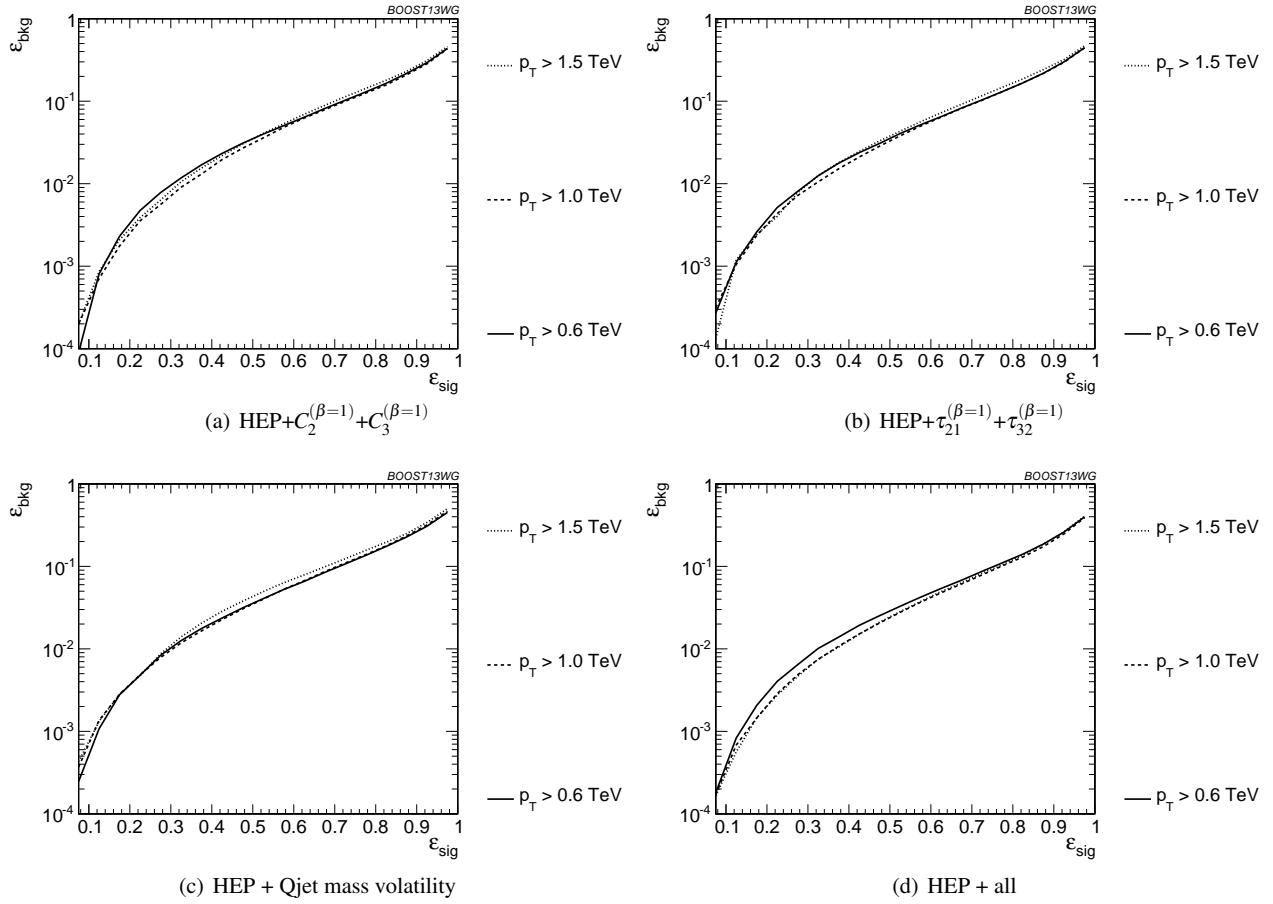


**Fig. 43** Comparison of BDT combination of HEP tagger + shape at different  $p_T$  using the anti- $k_T$   $R=0.8$  algorithm.

3. *Boost2011*, Princeton University, 22-26 May 2011, [\[https://indico.cern.ch/event/138809/\]](https://indico.cern.ch/event/138809/).
4. *Boost2012*, IFIC Valencia, 23-27 July 2012, [\[http://ific.uv.es/boost2012\]](http://ific.uv.es/boost2012).
5. *Boost2013*, University of Arizona, 12-16 August 2013, [\[https://indico.cern.ch/event/215704/\]](https://indico.cern.ch/event/215704/).
6. *Boost2014*, University College London, 18-22 August 2014, [\[http://http://www.hep.ucl.ac.uk/boost2014/\]](http://http://www.hep.ucl.ac.uk/boost2014/).
7. A. Abdesselam, E. B. Kuutmann, U. Bitenc, G. Brooijmans, J. Butterworth, et al., *Boosted objects: A Probe of beyond the Standard Model physics*, *Eur.Phys.J.* **C71** (2011) 1661, [[arXiv:1012.5412](#)].
8. A. Altheimer, S. Arora, L. Asquith, G. Brooijmans, J. Butterworth, et al., *Jet Substructure at the Tevatron and LHC: New results, new tools, new benchmarks*, *J.Phys.* **G39** (2012) 063001, [[arXiv:1201.0008](#)].
9. A. Altheimer, A. Arce, L. Asquith, J. Backus Mayes, E. Bergeaas Kuutmann, et al., *Boosted objects and jet substructure at the LHC*, [[arXiv:1311.2708](#)].
10. M. Cacciari, G. P. Salam, and G. Soyez, *FastJet User Manual*, *Eur.Phys.J.* **C72** (2012) 1896, [[arXiv:1111.6097](#)].
11. T. Plehn, M. Spannowsky, M. Takeuchi, and D. Zerwas, *Stop Reconstruction with Tagged Tops*, *JHEP* **1010** (2010) 078, [[arXiv:1006.2833](#)].
12. D. E. Kaplan, K. Rehermann, M. D. Schwartz, and B. Tweedie, *Top Tagging: A Method for Identifying Boosted Hadronically Decaying Top Quarks*, *Phys.Rev.Lett.* **101** (2008) 142001, [[arXiv:0806.0848](#)].
13. J. Alwall, M. Herquet, F. Maltoni, O. Mattelaer, and T. Stelzer, *MadGraph 5 : Going Beyond*, *JHEP* **1106** (2011) 128, [[arXiv:1106.0522](#)].
14. Y. Gao, A. V. Gritsan, Z. Guo, K. Melnikov, M. Schulze, et al., *Spin determination of single-produced resonances at hadron colliders*, *Phys.Rev.* **D81** (2010) 075022, [[arXiv:1001.3396](#)].
15. S. Bolognesi, Y. Gao, A. V. Gritsan, K. Melnikov, M. Schulze, et al., *On the spin and parity of a single-produced resonance at the LHC*, *Phys.Rev.* **D86** (2012) 095031, [[arXiv:1208.4018](#)].
16. I. Anderson, S. Bolognesi, F. Caola, Y. Gao, A. V. Gritsan, et al., *Constraining anomalous HVV*

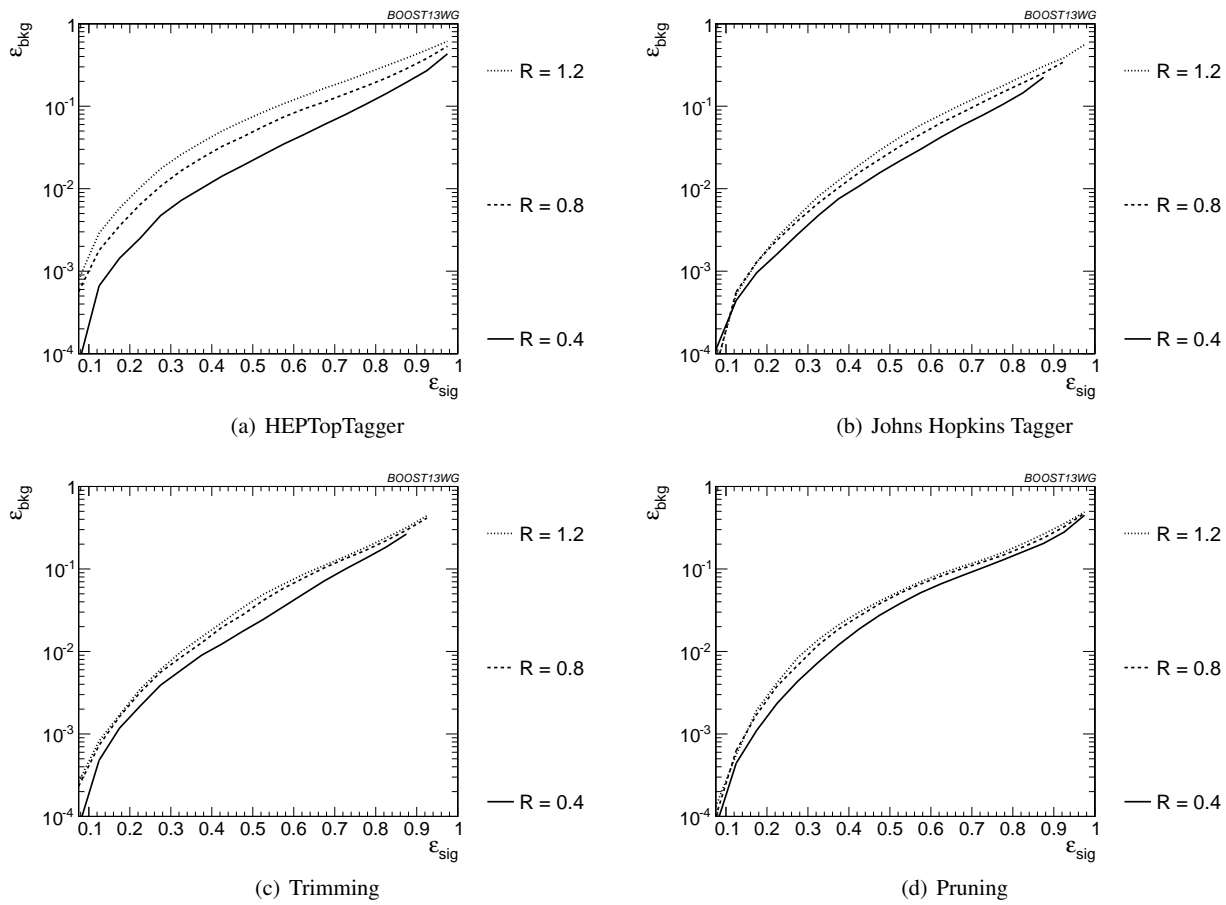


**Fig. 44** Comparison of tagger and jet shape performance at different radius at  $p_T = 1.5$ -1.6 TeV.

- interactions at proton and lepton colliders, *Phys.Rev.* **D89** (2014) 035007, [[arXiv:1309.4819](#)].
17. J. Pumplin, D. Stump, J. Huston, H. Lai, P. M. Nadolsky, et al., *New generation of parton distributions with uncertainties from global QCD analysis*, *JHEP* **0207** (2002) 012, [[hep-ph/0201195](#)].
18. T. Sjostrand, S. Mrenna, and P. Z. Skands, *A Brief Introduction to PYTHIA 8.1*, *Comput.Phys.Commun.* **178** (2008) 852–867, [[arXiv:0710.3820](#)].
19. A. Buckley, J. Butterworth, S. Gieseke, D. Grellscheid, S. Hoche, et al., *General-purpose event generators for LHC physics*, *Phys.Rept.* **504** (2011) 145–233, [[arXiv:1101.2599](#)].
20. T. Gleisberg, S. Hoeche, F. Krauss, M. Schonherr, S. Schumann, et al., *Event generation with SHERPA 1.1*, *JHEP* **0902** (2009) 007, [[arXiv:0811.4622](#)].
21. S. Schumann and F. Krauss, *A Parton shower algorithm based on Catani-Seymour dipole factorisation*, *JHEP* **0803** (2008) 038, [[arXiv:0709.1027](#)].
22. F. Krauss, R. Kuhn, and G. Soff, *AMEGIC++ 1.0: A Matrix element generator in C++*, *JHEP* **0202** (2002) 044, [[hep-ph/0109036](#)].
23. T. Gleisberg and S. Hoeche, *Comix, a new matrix element generator*, *JHEP* **0812** (2008) 039, [[arXiv:0808.3674](#)].
24. S. Hoeche, F. Krauss, S. Schumann, and F. Siegert, *QCD matrix elements and truncated showers*, *JHEP* **0905** (2009) 053, [[arXiv:0903.1219](#)].
25. M. Schonherr and F. Krauss, *Soft Photon Radiation in Particle Decays in SHERPA*, *JHEP* **0812** (2008) 018, [[arXiv:0810.5071](#)].
26. **JADE Collaboration** Collaboration, S. Bethke et al., *Experimental Investigation of the Energy Dependence of the Strong Coupling Strength*, *Phys.Lett.* **B213** (1988) 235.
27. M. Cacciari, G. P. Salam, and G. Soyez, *The Anti- $k(t)$  jet clustering algorithm*, *JHEP* **0804** (2008) 063, [[arXiv:0802.1189](#)].
28. Y. L. Dokshitzer, G. Leder, S. Moretti, and B. Webber, *Better jet clustering algorithms*, *JHEP* **9708** (1997) 001, [[hep-ph/9707323](#)].
29. M. Wobisch and T. Wengler, *Hadronization corrections to jet cross-sections in deep inelastic*

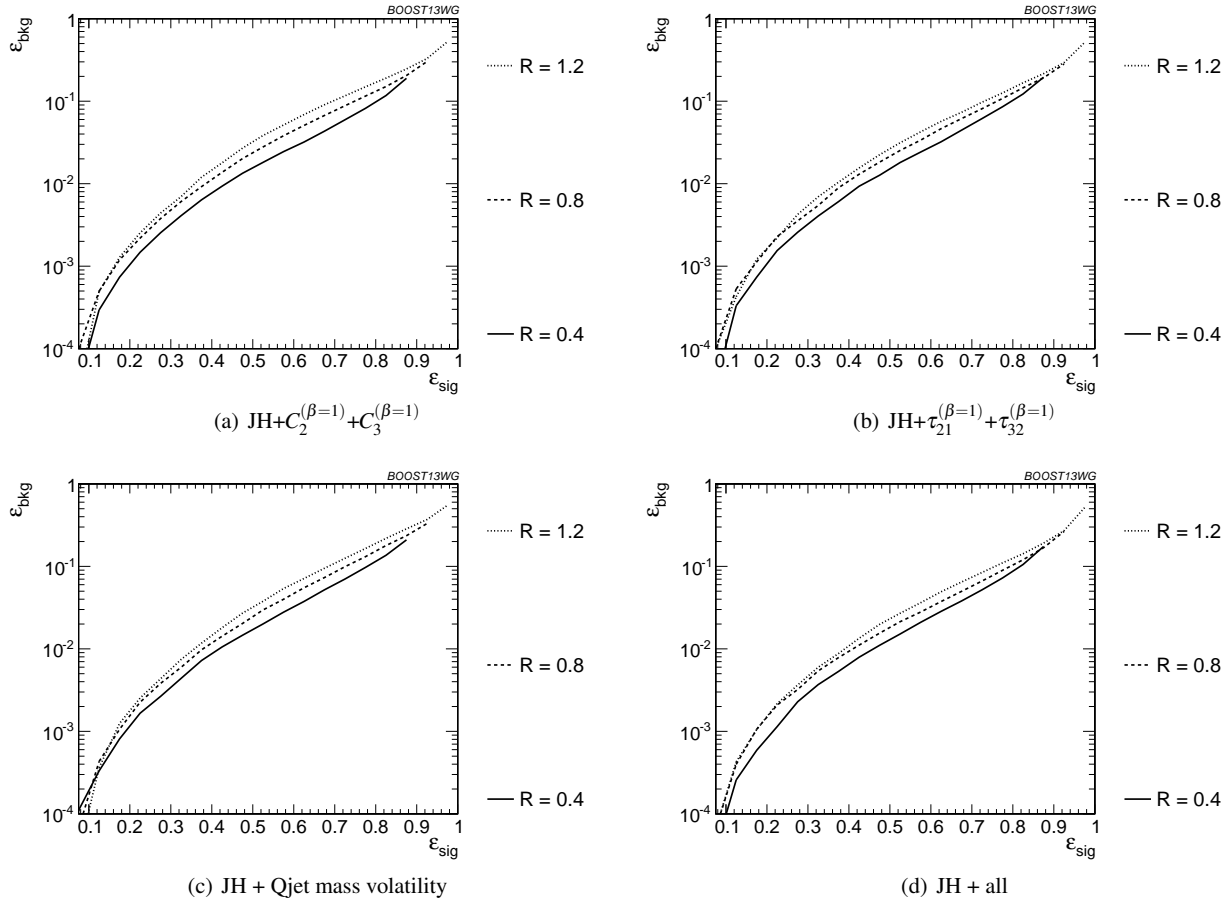


**Fig. 45** Comparison of BDT combination of JH tagger + shape at different radius at  $p_T = 1.5-1.6$  TeV.

- 1652 scattering, [hep-ph/9907280](#).  
1653 30. S. Catani, Y. L. Dokshitzer, M. Seymour, and  
1654 B. Webber, *Longitudinally invariant  $K_t$  clustering*  
1655 *algorithms for hadron hadron collisions*, *Nucl.Phys.*  
1656 **B406** (1993) 187–224.  
1657 31. S. D. Ellis and D. E. Soper, *Successive combination jet*  
1658 *algorithm for hadron collisions*, *Phys.Rev.* **D48** (1993)  
1659 3160–3166, [[hep-ph/9305266](#)].  
1660 32. S. D. Ellis, A. Hornig, T. S. Roy, D. Krohn, and M. D.  
1661 Schwartz, *Qjets: A Non-Deterministic Approach to*  
1662 *Tree-Based Jet Substructure*, *Phys.Rev.Lett.* **108** (2012)  
1663 182003, [[arXiv:1201.1914](#)].  
1664 33. S. D. Ellis, A. Hornig, D. Krohn, and T. S. Roy, *On*  
1665 *Statistical Aspects of Qjets*, *JHEP* **1501** (2015) 022,  
1666 [[arXiv:1409.6785](#)].  
1667 34. S. D. Ellis, C. K. Vermilion, and J. R. Walsh,  
1668 *Recombination Algorithms and Jet Substructure:*  
1669 *Pruning as a Tool for Heavy Particle Searches*,  
1670 *Phys.Rev.* **D81** (2010) 094023, [[arXiv:0912.0033](#)].  
1671 35. D. Krohn, J. Thaler, and L.-T. Wang, *Jet Trimming*,  
1672 *JHEP* **1002** (2010) 084, [[arXiv:0912.1342](#)].  
1673 36. J. M. Butterworth, A. R. Davison, M. Rubin, and G. P.  
1674 Salam, *Jet substructure as a new Higgs search channel*  
1675 *at the LHC*, *Phys.Rev.Lett.* **100** (2008) 242001,  
1676 [[arXiv:0802.2470](#)].  
1677 37. A. J. Larkoski, S. Marzani, G. Soyez, and J. Thaler,  
1678 *Soft Drop*, *JHEP* **1405** (2014) 146,  
1679 [[arXiv:1402.2657](#)].  
1680 38. M. Dasgupta, A. Fregoso, S. Marzani, and G. P. Salam,  
1681 *Towards an understanding of jet substructure*, *JHEP*  
1682 **1309** (2013) 029, [[arXiv:1307.0007](#)].  
1683 39. J. Thaler and K. Van Tilburg, *Identifying Boosted*  
1684 *Objects with  $N$ -subjettiness*, *JHEP* **1103** (2011) 015,  
1685 [[arXiv:1011.2268](#)].  
1686 40. A. J. Larkoski, D. Neill, and J. Thaler, *Jet Shapes with*  
1687 *the Broadening Axis*, *JHEP* **1404** (2014) 017,  
1688 [[arXiv:1401.2158](#)].  
1689 41. A. J. Larkoski and J. Thaler, *Unsafe but Calculable:*  
1690 *Ratios of Angularities in Perturbative QCD*, *JHEP*  
1691 **1309** (2013) 137, [[arXiv:1307.1699](#)].  
1692 42. A. J. Larkoski, G. P. Salam, and J. Thaler, *Energy*  
1693 *Correlation Functions for Jet Substructure*, *JHEP* **1306**  
1694 (2013) 108, [[arXiv:1305.0007](#)].



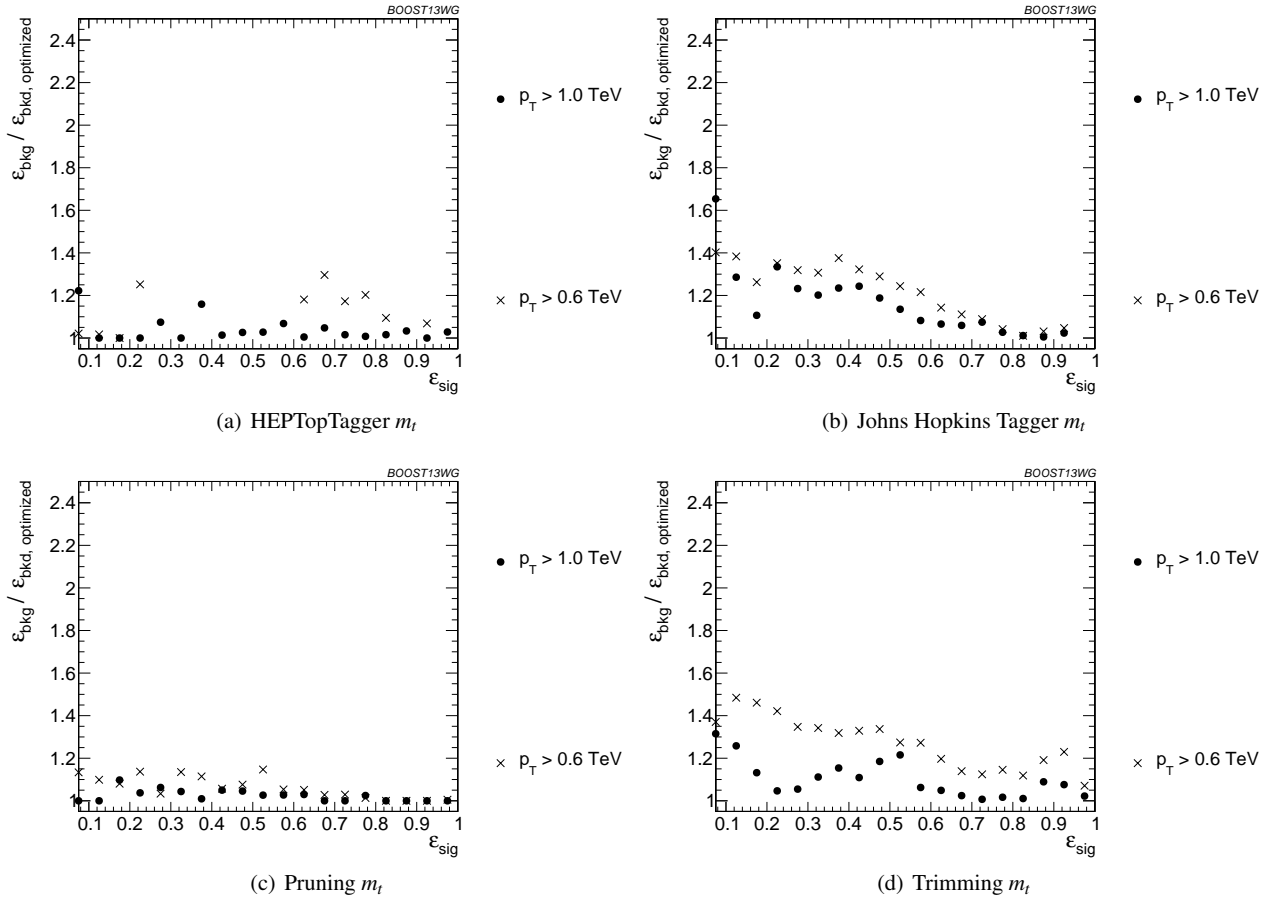


**Fig. 46** Comparison of top mass performance of different taggers at different  $p_T$  using the anti- $k_T$   $R=0.8$  algorithm; the tagger inputs are set to the optimum value for  $p_T = 1.5 - 1.6$  TeV.

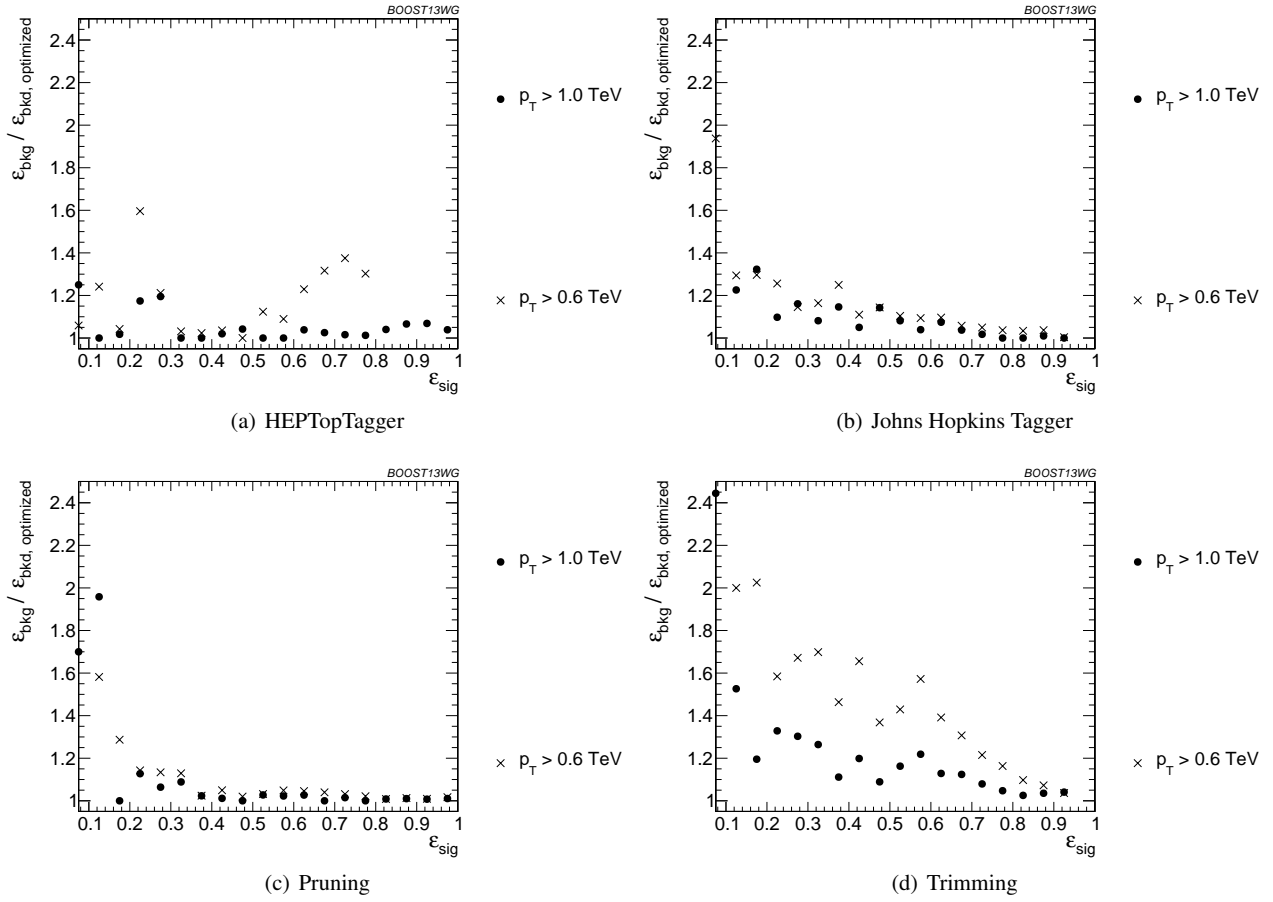


**Fig. 47** Comparison of BDT combination of tagger performance at different  $p_T$  using the anti- $k_T$   $R=0.8$  algorithm; the tagger inputs are set to the optimum value for  $p_T = 1.5 - 1.6$  TeV.

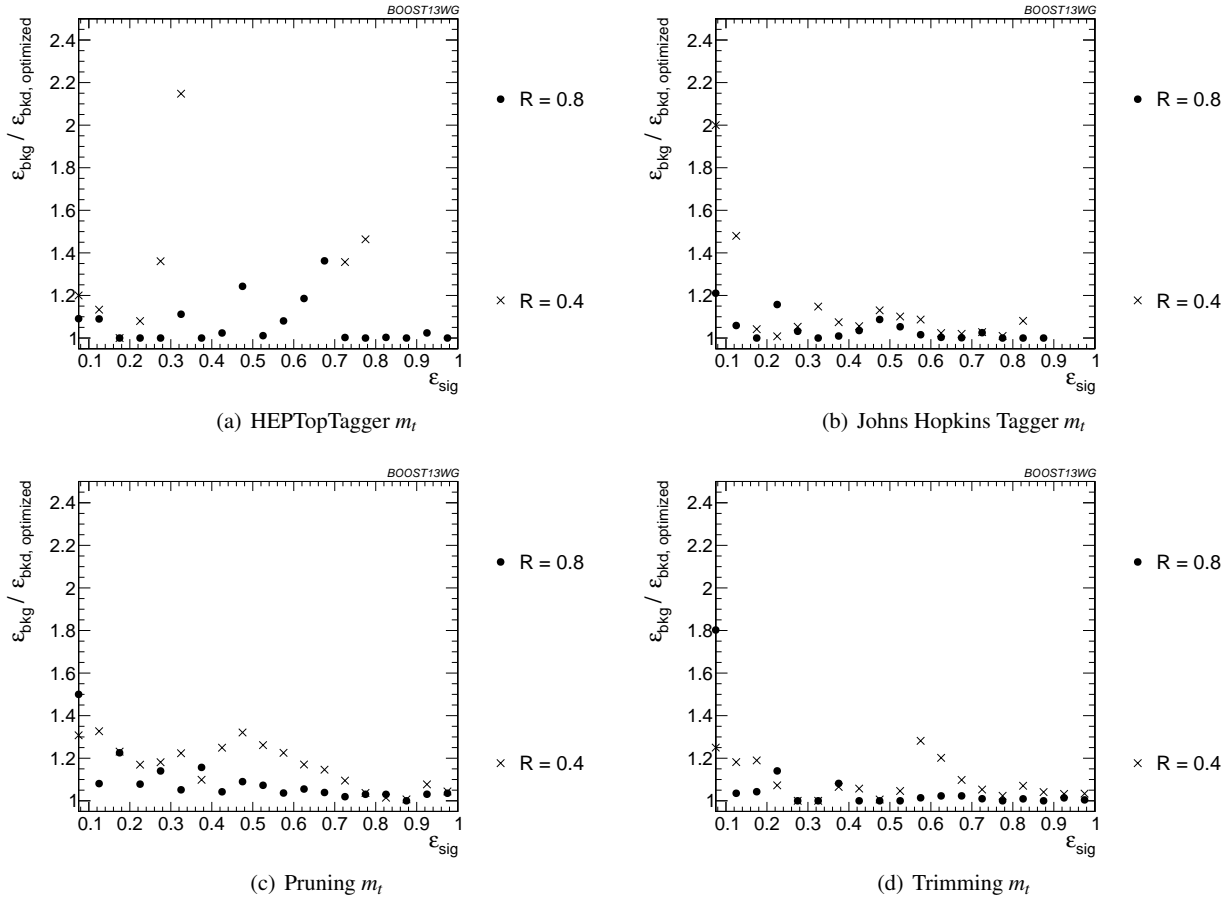


**Fig. 48** Comparison of top mass performance of different taggers at different  $R$  in the  $p_T = 1500 - 1600$  GeV bin; the tagger inputs are set to the optimum value for  $R = 1.2$ .

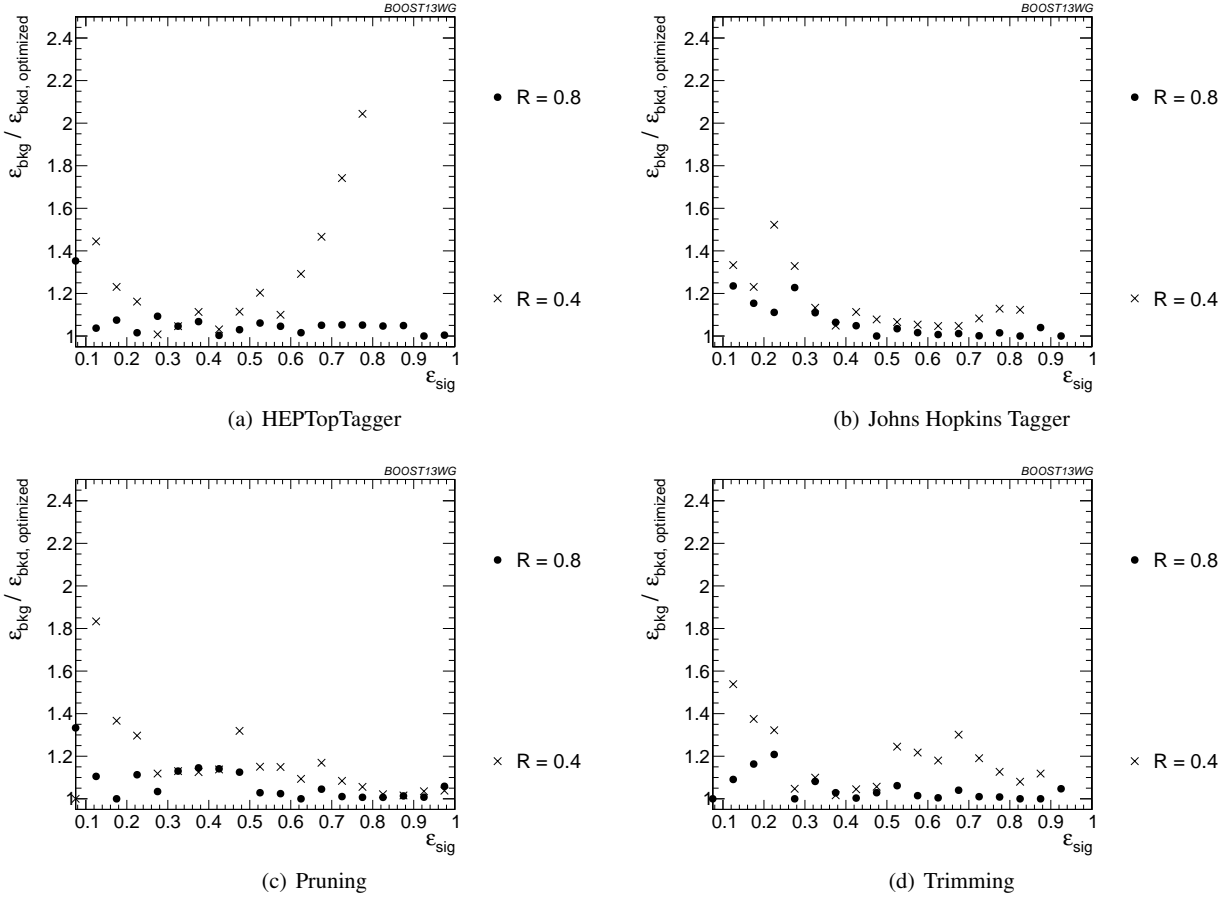


**Fig. 49** Comparison of BDT combination of tagger performance at different radius at  $p_T = 1.5-1.6$  TeV; the tagger inputs are set to the optimum value for  $R = 1.2$ .

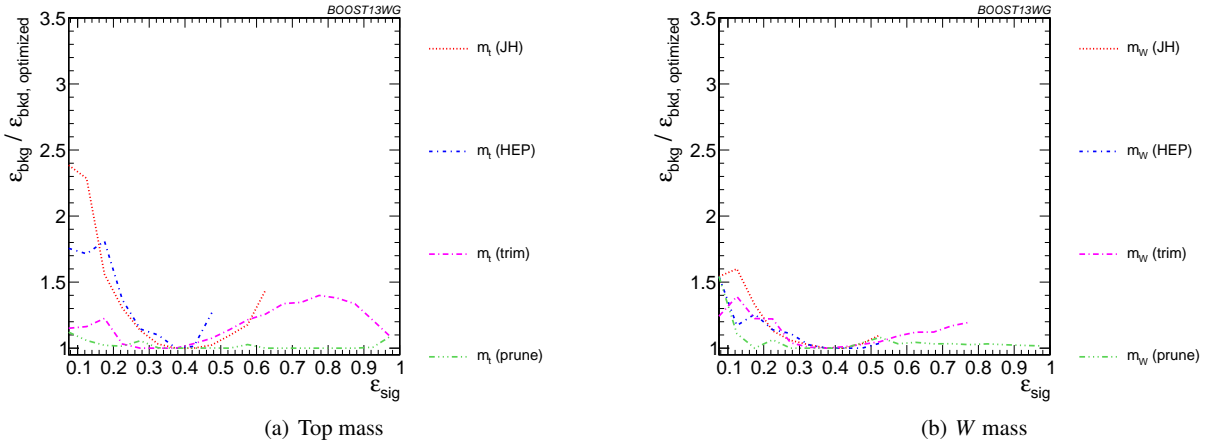


**Fig. 50** Comparison of single-variable top-tagging performance in the  $p_T = 1 - 1.1$  GeV bin using the anti- $k_T$ ,  $R=0.8$  algorithm; the inputs for each tagger are optimized for the  $\epsilon_{\text{sig}} = 0.3 - 0.35$  bin.

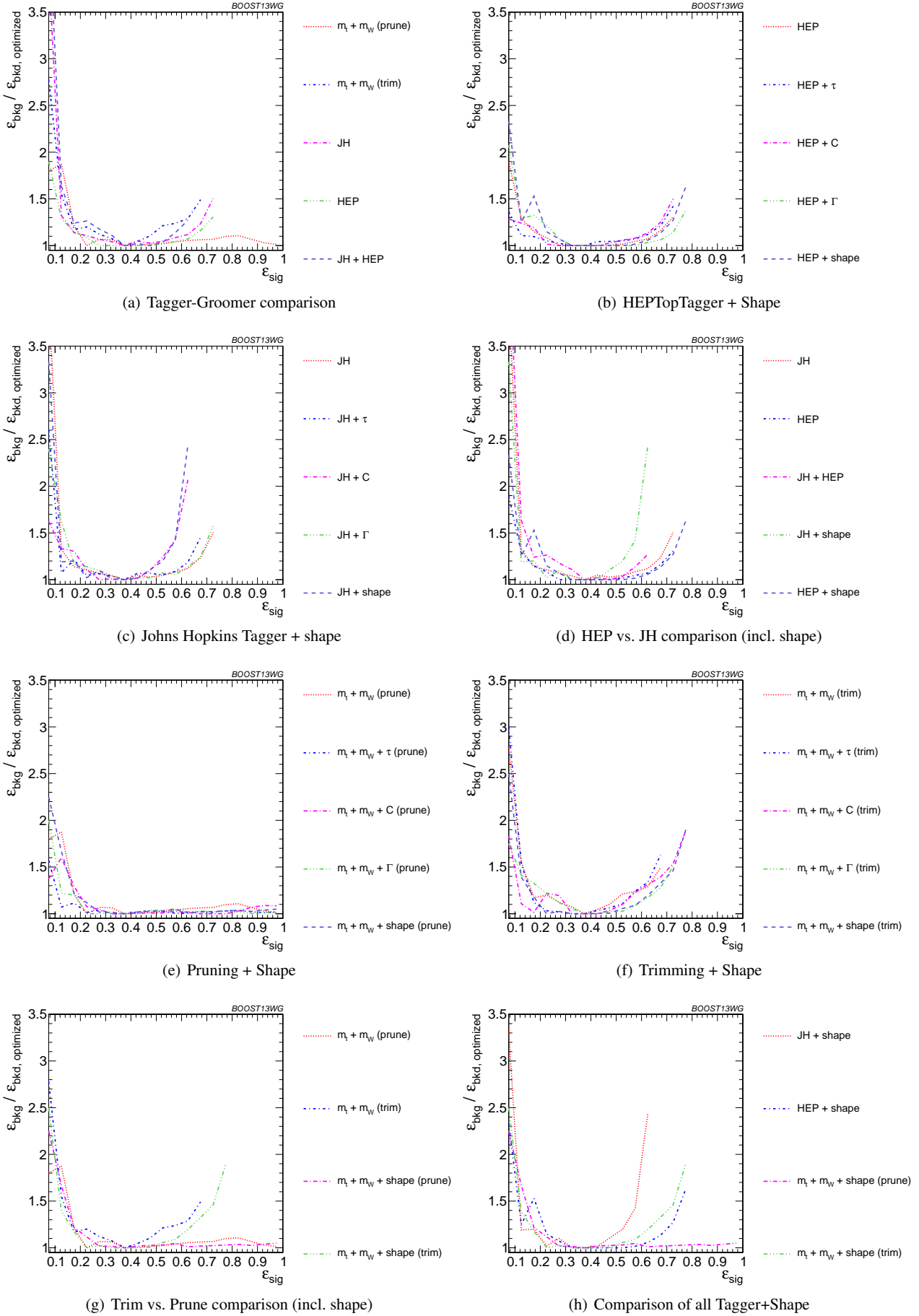


**Fig. 51** The BDT combinations in the  $p_T = 1 - 1.1$  TeV bin using the anti- $k_T$   $R=0.8$  algorithm. Taggers are combined with the following shape observables:  $\tau_{21}^{(\beta=1)} + \tau_{32}^{(\beta=1)}$ ,  $C_2^{(\beta=1)} + C_3^{(\beta=1)}$ ,  $\Gamma_{Qjet}$ , and all of the above (denoted “shape”). The inputs for each tagger are optimized for the  $\epsilon_{sig} = 0.3 - 0.35$  bin.